



ORGANIC BULK-HETEROJUNCTION PHOTOVOLTAIC DEVICES: MATERIALS, DEVICE ARCHITECTURES AND INTERFACIAL PROCESSES

Margherita Bolognesi

Dipòsit Legal: T.56-2014

ADVERTIMENT. L'accés als continguts d'aquesta tesi doctoral i la seva utilització ha de respectar els drets de la persona autora. Pot ser utilitzada per a consulta o estudi personal, així com en activitats o materials d'investigació i docència en els termes establerts a l'art. 32 del Text Refós de la Llei de Propietat Intel·lectual (RDL 1/1996). Per altres utilitzacions es requereix l'autorització prèvia i expressa de la persona autora. En qualsevol cas, en la utilització dels seus continguts caldrà indicar de forma clara el nom i cognoms de la persona autora i el títol de la tesi doctoral. No s'autoritza la seva reproducció o altres formes d'explotació efectuades amb finalitats de lucre ni la seva comunicació pública des d'un lloc aliè al servei TDX. Tampoc s'autoritza la presentació del seu contingut en una finestra o marc aliè a TDX (framing). Aquesta reserva de drets afecta tant als continguts de la tesi com als seus resums i índexs.

ADVERTENCIA. El acceso a los contenidos de esta tesis doctoral y su utilización debe respetar los derechos de la persona autora. Puede ser utilizada para consulta o estudio personal, así como en actividades o materiales de investigación y docencia en los términos establecidos en el art. 32 del Texto Refundido de la Ley de Propiedad Intelectual (RDL 1/1996). Para otros usos se requiere la autorización previa y expresa de la persona autora. En cualquier caso, en la utilización de sus contenidos se deberá indicar de forma clara el nombre y apellidos de la persona autora y el título de la tesis doctoral. No se autoriza su reproducción u otras formas de explotación efectuadas con fines lucrativos ni su comunicación pública desde un sitio ajeno al servicio TDR. Tampoco se autoriza la presentación de su contenido en una ventana o marco ajeno a TDR (framing). Esta reserva de derechos afecta tanto al contenido de la tesis como a sus resúmenes e índices.

WARNING. Access to the contents of this doctoral thesis and its use must respect the rights of the author. It can be used for reference or private study, as well as research and learning activities or materials in the terms established by the 32nd article of the Spanish Consolidated Copyright Act (RDL 1/1996). Express and previous authorization of the author is required for any other uses. In any case, when using its content, full name of the author and title of the thesis must be clearly indicated. Reproduction or other forms of for profit use or public communication from outside TDX service is not allowed. Presentation of its content in a window or frame external to TDX (framing) is not authorized either. These rights affect both the content of the thesis and its abstracts and indexes.

Margherita Bolognesi

Organic bulk-heterojunction
photovoltaic devices: materials, device
architectures and interfacial processes

Doctoral Thesis

Supervised by Dr. Emilio Palomares

Tutor at foreign institution Dr. Michele Muccini

Department of Analytical Chemistry and Organic
Chemistry



UNIVERSITAT ROVIRA I VIRGILI



STATEMENT OF SUPERVISION

Dr. Emilio Palomares

Department of Electronic Materials and Devices

Institute of Chemical Research of Catalonia (ICIQ)

Av. Països Catalans 16 – 43007 Tarragona (Spain)

Phone +34 977920200 (Ext. 211) – Fax +34 977920823

I STATE

that the present study, entitled “Organic bulk-heterojunction photovoltaic devices: materials, device architectures and interfacial processes”, presented by Margherita Bolognesi for the award of the degree of Doctor, has been carried out under my supervision at Department of Electronic Materials and Devices, at Institute of Chemical Research of Catalonia (ICIQ), and that it fulfils all the requirements to be eligible for the European Doctorate Award.

Tarragona, 03 Abril 2013

Doctoral Thesis Supervisor

Dr. Emilio Palomares

ACKNOWLEDGEMENTS

I am grateful for the financial support to this thesis of the Catalan Institute of Chemical Investigation (ICIQ) of Tarragona given through the pre-doctoral fellowship with reference 05/09 of Dr. Emilio Palomares, the financial support of the Project ERC StG with reference 239582 of Dr. Emilio Palomares and the financial support of the consortium Laboratory MIST E-R through the program P.O. FESR 2007-2013 of Regione Emilia Romagna, Activity I.1.1.

I am grateful to Dr. Emilio Palomares for supervising the thesis and to Dr. Michele Muccini for tutoring the work carried out at ISMN – CNR of Bologna, Italy. I wish to thank all the colleagues in Dr. Palomares group and the colleagues in Dr. Michele Muccini group, for their precious scientific support, their collaboration and their friendship.

I wish to thank Prof. Jordi Riu, Mrs. Eva Busto, Mrs. Giovanna Guidicelli and Mrs. Dúnia Munnié for allowing me to deposit and discuss this thesis, helping me with all the bureaucratic procedures.

I wish to thank my future husband Gianni, my father, my sisters and brothers and all my friends in Tarragona and in Bologna, for their love and support.

LIST OF PUBLICATIONS

Margherita Bolognesi, Antonio Sánchez-Díaz, Jon Ajuria, Roberto Pacios and Emilio Palomares, "The effect of selective contact electrodes on the interfacial charge recombination kinetics and device efficiency of organic polymer solar cells", *Phys. Chem. Chem. Phys.*, 2011, DOI: 10.1039/C0CP02879G

Margherita Bolognesi, Marta Tassarolo, Tamara Posati, Morena Nocchetti, Valentina Benfenati, Mirko Seri, Giampiero Ruani and Michele Muccini, "Efficiency enhancement of P3HT:PCBM solar cells containing scattering Zn-Al hydrotalcite nanoparticles in the PEDOT:PSS layer", accepted in *Organic Photonics and Photovoltaics*, 2013

Alessandro Abbotto, Mirko Seri, Milind S. Dangat, Filippo De Angelis, Norberto Manfredi, Edoardo Mosconi, Margherita Bolognesi, Riccardo Ruffo, Matteo M. Salamone, Michele Muccini, "A Vinylene-Linked Benzo[1,2-b:4,5-b']dithiophene-2,1,3-Benzothiadiazole Low-Bandgap Polymer", *JOURNAL OF POLYMER SCIENCE PART A: POLYMER CHEMISTRY*, 2012, DOI: 10.1002/pola.26046

Mirko Seri, Margherita Bolognesi, Zhihua Chen, Shaofeng Lu, Wouter Koopman, Antonio Facchetti, and Michele Muccini, "Fine Structural Tuning of New Cyanated Dithieno[3,2-b:2',3'-d]silole-Oligothiophene Copolymers: Synthesis, Characterization and Photovoltaic Response", submitted for publication

INDEX

CHAPTER I: Introduction to photovoltaics and aim of the work

1. History of photovoltaics	1
2. Organic photovoltaic (OPV)	2
2.1 Inorganic and organic semiconductors	3
2.2. Single layer OPV devices	4
2.3. Donor/acceptor bilayer heterojunction OPV devices	6
2.4. Donor/acceptor bulk heterojunction (BHJ) OPV devices	7
2.5. Polymer:fullerene BHJ OPV devices	8
3. Working principles in BHJ OPV devices	9
3.1. Light absorption and exciton formation	10
3.2. Exciton diffusion to the donor/acceptor interface	12
3.3. Charge separation at the donor/acceptor interface	14
3.4. Charge transport in the D and A phases	14
3.5. Charge collection at the electrodes	15
4. Fundamental photovoltaic parameters	16
4.1. Equivalent circuit of BHJ OPV devices	16
4.2. I-V curves: PCE, Isc, Voc, FF	19
4.3. Quantum efficiency	21
5. Limiting factors in BHJ OPV devices efficiency	22
6. The aim of this work: strategies to improve the BHJ OPV cells performance	24
7. Bibliography	25

CHAPTER II: Photoactive polymers, the donor materials

1. Polymeric semiconductors as donors in BHJ OPV devices	29
1.1. Advantages of using polymeric over small molecule donors	29
1.2. Traditional donor polymers and recent achievements	30
1.3. Requisites for polymeric semiconductors to work as donor in BHJ OPV devices	31
2. Polymeric donor design and processing strategies to improve BHJ OPVs devices performances	33
2.1. A new class of efficient Si-DT-based polymers	33
2.1.1. Experimental	35
2.1.1.1. Materials and Methods	35
2.1.1.2. OPV Devices Fabrication and Characterization	36
2.1.1.3. Hole-only Devices Fabrication and Characterization	37
2.1.1.4. Thin-film characterization	37
2.1.2. Results and discussion	38
2.1.2.1. Polymers synthesis and thermal properties	38
2.1.2.2. Polymers optical and electrochemical properties	39

2.1.2.3. Devices optimization and characterization	42
2.1.2.4. Morphological analysis.....	48
2.1.2.5. Photo-luminescence (PL) quenching studies.....	49
2.1.3. Conclusions.....	53
2.2. A new push-pull polymer with unsaturated spacer.....	54
2.2.1. Introduction.....	54
2.2.2. Experimental.....	56
2.2.2.1. Polymer characterization and computational investigations.....	56
2.2.2.2. Devices fabrication and characterization	57
2.2.3. Results and Discussion.....	58
2.2.3.1. Synthesis, chemical characterization, and optical properties.....	58
2.2.3.2. Electrochemical characterization.....	60
2.2.3.3. Structural theoretical calculations.....	62
2.2.3.4. Photovoltaic properties.....	63
2.2.4. Conclusions	68
3. Conclusions.....	69
4. Bibliography.....	71

CHAPTER III: Charge extracting (buffer) layers

1. Introduction on the role of buffer layers.....	77
2. TiO _x and ZnO based CBL: effects on the charge recombination and efficiency of inverted devices	79
2.1. Experimental.....	80
2.2. Results and discussion.....	82
2.2.1. Metal oxide thin film morphology.....	82
2.2.1. Devices photovoltaic characterization.....	83
2.2.2. Charge recombination dynamics.....	84
3. Conclusions	90
4. Bibliography.....	92

CHAPTER IV: Light managing techniques in OPVs

1. Different approaches for light managing in OPVs.....	95
2. Scattering particles in the PEODT:PSS layer of P3HT:PCBM-based solar cells.....	96
2.1. Experimental.....	98
2.1.1. Materials and methods.....	98
2.1.2. HTs/PEDOT:PSS thin-films preparation and characterization	98
2.1.3. Device fabrication and characterization.....	99
2.2. Results and discussion.....	100

2.2.1. HTs/PEDOT:PSS thin-film properties	100
2.2.2. Scattering of HTs:PEDOT:PSS films	104
2.2.3. Device performances	106
2.3. Conclusions.....	109
3. Bibliography.....	110

CHAPTER V: General conclusions and prospective

APPENDIX: List of symbols and abbreviations

CHAPTER I: INTRODUCTION TO PHOTOVOLTAICS AND AIM OF THE WORK

1. HISTORY OF PHOTOVOLTAICS

All living beings extract energy from the environment to convert it into other forms of energy used for their sustenance. Throughout history, man has developed and expanded his ability to use and harvest energy in all its forms, starting from the discovery of fire to the last generation of nuclear power plants. Since the industrial revolution to nowadays, the World Energy Consumption has increased exponentially in response to developed countries modern living standards, that are leading to a continuous expansion of the global energy demand and production (see **Figure 1**).

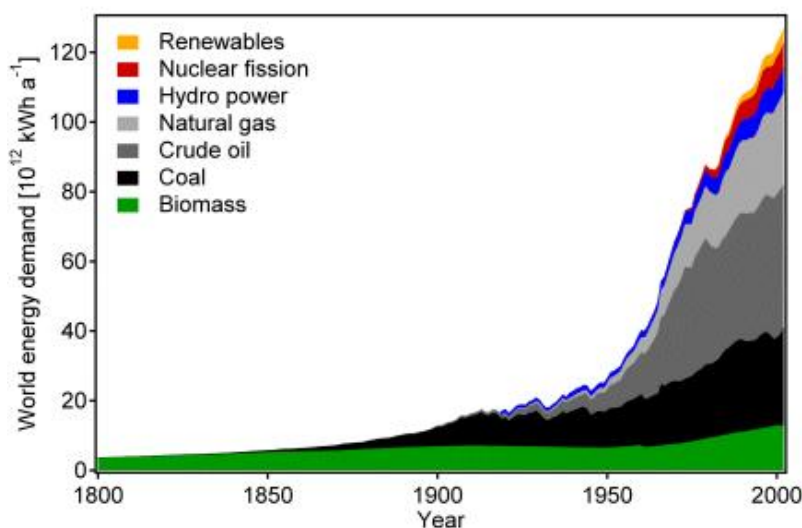


Figure 1 Representation of the World energy consumption over years since 1800.^[1]

However, the limited availability of primary exhaustible energy sources (i.e. fossil fuels and uranium) and the long-term adverse effects on the environment due to their exploitation, reflects the urgency to develop new strategies to effectively utilize other primary energy sources: the renewable ones.

The most clean, renewable and sustainable energy known to humankind is solar energy. In a way similar to the natural photosynthetic process, through which plants transform solar radiation energy into another form of energy such as the chemical potential, a photovoltaic device transform the photons energy into electrical energy. Electrical energy is one of the most important within secondary energetic sources, since it can be easily distributed, stored and used for many application.^[2]

The 'photovoltaic effect', the mechanism through which a solar cell converts the photon energy into mobile electrons, thus electricity, was first observed in 1839 by the French physicist Becquerel in an electrochemical experiment.^[3] Later, in 1876, William Adams and Richard Day observed photoconductivity in a solid state device

made of a thin layer of Selenium sandwiched between two heated platinum contacts.^[4] In the following years, while the first well performing Selenium/Gold based solid-state solar cell was built with an efficiency of 1%, photovoltaic effects were also observed in Copper/Copper Oxide thin films, in Lead Sulphide and Thallium Sulphide. The photovoltaic effect in these first photodiode-like structures was related to the existence of a barrier to the produced photocurrent flow at one of the two semiconductor/metal interfaces (i.e., rectifying action) by Goldman and Brodsky in 1914, while the relative theory was developed by Walter Schottky, Neville Mott and others in 1930.^[5]

However, it was not until the 1950s, with the development of good quality silicon wafers for applications in the emerging technology of solid state electronics, that potentially useful quantities of power were produced by photovoltaic devices (PVs). In fact, the discovery of a way to manufacture positively (p) and negatively (n) doped silicon led to the preparation of silicon p-n junction structures with much better rectifying action than Schottky barriers and a better photovoltaic behavior. The first silicon solar cell, reported by Chapin, Fuller and Pearson in 1954, showed in fact an efficiency of 6%.^[6]

In parallel, the discoveries leading to the birth of modern organic chemistry, in the end of the 19th and the beginning of 20th centuries, led to increased scientific and commercial interests in the research on organic materials. Anthracene was the first organic compound in which photoconductivity was observed by Pochettino in 1906^[7] and Volmer in 1913,^[8] while in the early 1960s it was discovered that many common dyes, such as methylene blue, had semiconducting properties.^[9] Later, these dyes were among the first organic materials to exhibit the photovoltaic effect, together with many other biological molecules such as carotenes, chlorophylls, porphyrins and phthalocyanines, while the first organic photovoltaic (OPV) device was described by Tang in 1986.^[10]

The progress in the PV technology had a strong impulse after the 1970s oil crisis, which pushed the scientific and industrial research to produce around 15% efficient Si-based inorganic PVs, also called first generation PVs, whose market expanded at a rate of 15% per annum in the late 1990s and even more in the last years (30% per annum).^[11] However, the inherent limitation to a real broad scale-up of first generation PV technologies is determined by the very laborious and energy consuming processing of Silicon wafers, representing more than 60% of the manufacturing costs of Si-based PVs. Therefore, the scientific and industrial research in the last decades were mainly directed to the increase of the device efficiency and to the reduction of materials and production costs, these efforts leading to the current emerging PV technologies such as organic photovoltaics.

2. ORGANIC PHOTOVOLTAIC (OPV)

The organic photovoltaic (OPV) technology is thought to provide an excellent alternative to Si-based PVs in those applications where the importance of price and mechanical properties dominate over high performances or lifetime.

Before going into a deeper analysis on OPV devices, a comparison between the properties of semiconducting inorganic and organic materials could be useful to understand the main advantages and drawbacks for their application in the photovoltaic technology.

2.1. Inorganic and organic semiconductors

The key differences between inorganic and organic semiconductors lie in their electronic structures. Traditional inorganic semiconductors are crystalline ordered solids where atoms are covalently bounded and electrons (and their wave's functions) are spatially delocalized over the crystalline lattice. The energy states allowed for these electrons form the semiconductor valence and conduction bands, which are dense (continuous) energy bands separated by an energy gap (the band gap, E_g). In inorganic PV cells, an electron can be promoted from the valence to the conduction band upon light absorption (or other excitation mechanisms), generating free delocalized charges which can be driven to the electrodes through the application of an external electrical potential.

On the opposite, traditional organic semiconductors are conjugated molecular or polymeric compounds with a structure characterized by a sequence of sp^2 hybridized carbon atoms with un-hybridized p_z atomic orbitals. These atomic orbitals give rise to molecular σ and π electronic orbitals respectively. The bonding (π) and antibonding (π^*) orbitals of molecules compose the valence and conduction bands of the organic semiconducting material, identified as the highest occupied and lowest unoccupied molecular orbitals respectively (HOMO and LUMO). Since polymeric semiconductors are usually disordered (amorphous) materials, with weakly interacting Van-der-Waals bonded macromolecules, a narrower band width distribution and a much weaker delocalization of electronic wavefunctions among neighbouring molecules occur, causing the HOMO and LUMO bands to be discrete and not continuous. Therefore in OPV devices, the usual product of light absorption is a tightly bounded electron-hole pair, also called Frenkel exciton or mobile excited state,^[12] which is an electrically neutral species which, to first order, is unaffected by electric fields.

The intrinsic electronic diversity between inorganic and organic materials causes firstly a significant difference in the relative importance of interfacial processes in inorganic PV and OPV devices, which is closely related to the described charge generation mechanisms. While in inorganic PV cells free charges are directly generated upon light absorption under normal conditions, light absorption in organic materials results in the production of a mobile excited state which can dissociate into free charges only at an heterointerface where the exciton dissociation driving force overcomes the coulombing interaction which tightly bounds the electron-hole pair.^[13] This notably influences the photoactive material structure, at the micro- and nanoscopic

level, necessary for the inorganic and organic PV devices to function most efficiently.

Another consequence of the intrinsically different electronic structure of organic and inorganic semiconducting materials is their charge transport mechanism. Band transport is the mechanism typically observed in inorganic semiconductors, where delocalized charges are efficiently screened by the surrounding lattice, due to the high dielectric constant of inorganic materials, and are transported through the material bulk in the continuous conduction band of the semiconductor without important energy losses. Differently, in amorphous organic semiconductors the conductive electronic states are more localized. Charges, poorly screened by the neighbour molecules due to the low dielectric constant of organic materials,^[14] polarize and distort the surrounding lattice forming the polarons, which diffuse between adjacent molecules through a thermally activated and less efficient hopping mechanism, comparing to band transport.^[15] This explains the much lower charge mobility of amorphous organic solids (usually lower than 10^{-2} cm²/V·s)^[16] comparing to that of crystalline inorganic semiconductors.

The very different cohesion forces in crystalline inorganic solids and polymeric organic solids easily explain also the different physical and mechanical properties of the two materials. While inorganic crystalline semiconductors are rigid and brittle, have high processing (fusion) temperatures and are reasonably stable to degradation processes with water and oxygen, organic amorphous or semicrystalline polymeric materials are flexible and lightweight, can be dissolved at low temperatures (this rendering their processing cheaper, easier and transferrable to industrial processes in continuum), but often suffer of easy degradation in ambient conditions.

The electronic structures of inorganic and organic semiconductors also determine a difference in their light absorption properties, leading organic materials to have higher absorption coefficients in the visible light range ($\sim 10^5$ cm⁻¹) compared to inorganic semiconductors ($\sim 10^3 - 10^4$ cm⁻¹). On the other hand, lower E_g values can be obtained for p- and n-doped inorganic semiconductors, allowing an efficient absorption of solar light in its most extended spectral region (the infrared), while only band gaps limited to values higher than 1.4-1.5 eV are obtainable for organic semiconductors, confining the solar light absorption to the visible spectral region.

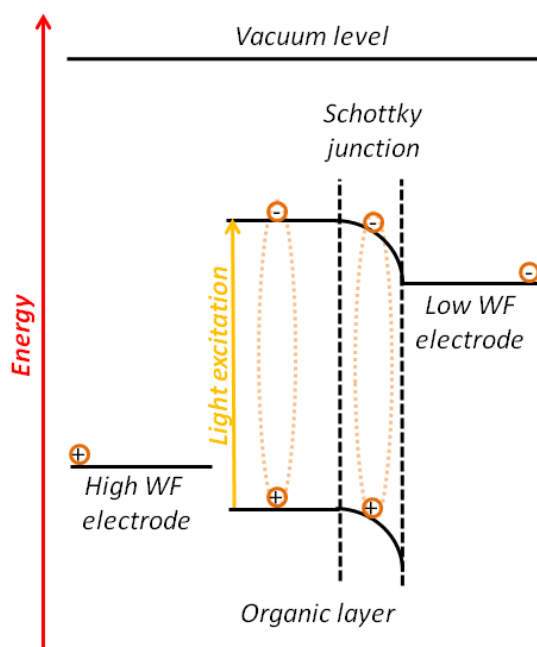
Finally, it should be reminded that the number of the synthetically available inorganic semiconducting compounds is extremely lower than their organic counterparts. Therefore an easier tuning of the chemical and physical properties by accurate molecular design and engineering, increasing the control on the performances optimization, is achievable for organic semiconductors comparing to inorganic ones.

In the history of OPV devices, research efforts aimed to the exploitation of the described advantageous characteristics of organic materials, while trying to

overcome the problems intrinsically linked to their use, such as a low electrical conductivity, the presence of impurities and a low stability in ambient conditions.

2.2. Single layer OPV devices

The first OPV devices had a very simple structure made of a single layer of photoactive organic material comprised between a semi-transparent electrode and a non-transparent one.^[17] However, the reported quantum efficiencies were very low because of the discussed poor charge mobility of the semiconducting organic layer, in the order of 10^{-3} $\text{cm}^2/\text{V}\cdot\text{s}$, very low comparing to that of single crystalline silicon (about 10^3 $\text{cm}^2/\text{V}\cdot\text{s}$). This low charge mobility, combined with a low interfacial area between the organic layer and the charges-extracting electrodes, bounded the efficiency of single layer OPV devices to very low values (around 0.1%).



Scheme 1 Processes and energetics occurring in a single layer D/A organic solar cell.

From a physical point of view, in single-layer OPV devices a thin layer of Schottky barrier is formed between the lower workfunction (WF) electrode and the organic layer, which is typically p-type, or hole conducting (**Scheme 1**). The diffusion of electrons from the low WF electrode into the organic material generates a depletion region (electrons enriched, or poor in holes). The resulting electric field causes the HOMO and LUMO bands-bending towards the Schottky contact, inside the depletion region. This field therefore facilitates the dissociation of excitons generated in or diffused into the depletion region, so the generated electrons can be collected by the low WF electrode while the holes can be transported across the film to the higher WF electrode. Because of the short diffusion length, most excitons generated outside the depletion region recombine

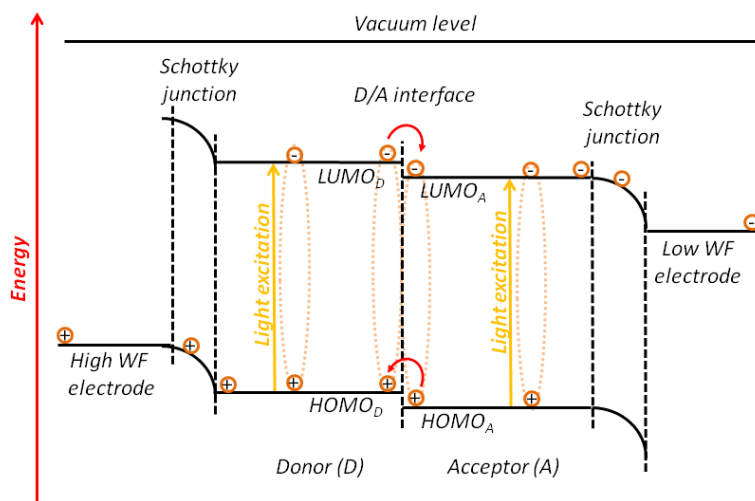
to the ground state and do not contribute to the photocurrent. Moreover, since free charges travel in the same phase, important charge losses due to recombination are also present. These factors explain the very low PV performances of single-layer OPVs.

2.3. Donor/acceptor bilayer heterojunction OPV devices

The second generation of OPV devices was first demonstrated by C. Tang in 1986,^[18] with a surprisingly high efficiency of 1%. The success of this kind of device consisted in the introduction of the donor-acceptor heterojunction concept. The device consisted in fact of a bilayer of p- and n- type organic semiconductors, also called as donor (D) and acceptor (A). In this kind of devices, once a photo-generated exciton, formed either in the D or A layer, reaches the D/A interfacial heterojunction by diffusion, the electrons would transfer to (or remain in) the acceptor LUMO ($LUMO_A$) and the holes would transfer to (or remain in) the donor HOMO ($HOMO_D$). The frontier orbital energy offsets between the donor and the acceptor ($LUMO_D-LUMO_A$ and $HOMO_D-HOMO_A$) are the key driving forces for the exciton dissociation (or charge separation). Due to both the internal field across the electrodes and the chemical potential driving forces, the electrons and holes can diffuse to the electrodes, in D/A bilayer heterojunction OPV devices, much easier than in single layer ones. The probability of charge recombination in bilayer devices is then reduced thanks to the dissociation of the Frenkel exciton electron-hole pair, which allows the electrons and holes to diffuse in two separated phases/layers.

However, the efficiency of bilayer devices is still limited by a low charges generation, mainly due to: i) the low exciton diffusion length in the D and A phases, typically some tens of nanometers, and ii) the low D/A heterojunction interfacial area available for excitons dissociation into separated charges, leading most excitons generated far from the D/A interface to recombine to the ground state.

In **Scheme 2** are represented the described processes and energetics.



Scheme 2 Processes and energetics occurring in a bilayer D/A organic solar cell.

2.4. Donor/acceptor bulk heterojunction (BHJ) OPV devices

A logical way to enhance the D/A binary heterojunction OPV devices efficiency is to maximize the D/A interfacial area while decreasing the exciton diffusion pathway to the D/A interface. This can be done by intimately blending the donor and acceptor materials, to form a bulk heterojunction (BHJ) active layer (**Figure 2**).

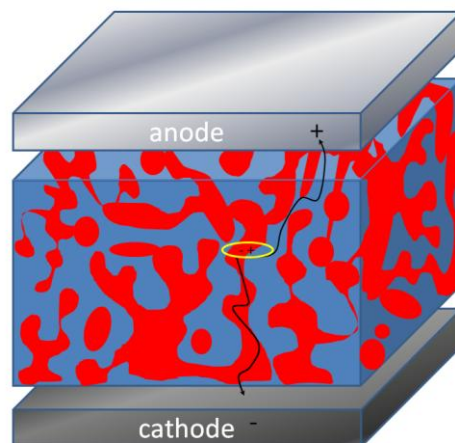


Figure 2 Schematic representation of a bulk heterojunction solar cell, composed of two finely intermixed phases of a donor (in BLUE) and an acceptor (in RED).

Efficiency indeed has been greatly improved in the first BHJ OPV devices, comparing to bilayer D/A heterojunction OPV ones: numerous cells employing poly(*p*-phenylene-vinylene) (PPV) or polythiophene derivatives (e.g. MEH-PPV, MDMO-PPV, P3HT or P3OT) as donors^[19] and CN-PPV^[20] or fullerene derivatives^[21] as acceptor have been intensely studied and reached near unity photoinduced charge separation efficiency.

The higher efficiency of D/A BHJ cells comparing to D/A bilayer cells can be attributed mainly to the reduction of exciton losses due to: i) a larger D/A interfacial area and ii) to the reduced dimensions of D and A domains in which excitons are formed and have to diffuse to reach the D/A interface. If the length scale of the D/A blend domains is similar to the D and A exciton diffusion lengths, most of the excitons generated in either material may reach the heterojunction interface. This allows to increase the BHJ photoactive film thickness, comparing to single or bilayer devices, up to more than 100 nm (one order of magnitude higher than the typical exciton diffusion length of amorphous organic semiconductors)^[22] in order to maximize the photons harvesting.

On the other hand, the typical low charge carrier mobility of organic semiconductors and the possible discontinuities in the electrons and holes conduction pathways through the A and D phases could limit the overall photoinduced charges collection at the electrodes. Indeed, one of the possible

limiting factors to the BHJ OPV devices efficiency are non-geminate (between electrons and holes dissociated from different excitons) recombination processes.

These considerations evidence how the BHJ film morphology plays a fundamental role on the device efficiency. The optimal morphology should result indeed in a fine intermix of D and A domains, with sizes that meet the compromise between the D and A exciton diffusion lengths and a high D/A interfacial area, together with the need of bicontinuous percolation pathways for charges transport at the electrodes. Therefore, the D/A BHJ film preparation method plays a key role in determining the final BHJ film morphology. High-vacuum thermal co-evaporation is a possible technique which is often used for molecular organic semiconducting materials, while the deposition of a D/A blend solution with techniques such as spin coating, blading or printing are usually employed for polymeric OPVs. In solution based processes, the accurate choice of solvent, solvent mixtures and/or additives, of the film drying time and temperature and of the film post-processing treatments allows a fine control of the final BHJ film morphology.

Despite the difficulty to favorably match the numerous factors determining the overall BHJ OPV devices efficiency, in recent years extraordinary improvements have been achieved for the BHJ OPV cells efficiency, now overcoming the $\sim 10\%$ and still rapidly increasing.^[23]

2.5. Polymer:fullerene BHJ OPV devices

Several approaches to organic photovoltaic active BHJ composites have been investigated to date. These include strategies based on photoinduced charge transfer within blends of low molecular weight molecules, blends of conjugated polymers, molecular dyads, or conjugated polymer:small molecule blends. Since ultrafast photoinduced electron transfer from a conjugated polymer as donor to buckminsterfullerene (C_{60}) or its derivatives as acceptor was first observed in 1992 by Sariciftci et al.,^[24] this material combination has been extensively studied in BHJ OPV cells. In 1995 it was fabricated the first fully organic BHJ solar cell based on a mixture of a soluble PPV derivative with a fullerene acceptor (the C_{60} derivative phenyl-C61-butyric acid methyl ester, or PC₆₁BM,^[25] **Figure 3**), while in 2001 it was obtained the first truly promising result for polymer:PC₆₁BM BHJ solar cells, through a BHJ film nanoscale morphology accurate optimization, yielding to a power conversion efficiency of 2.5%.^[26]

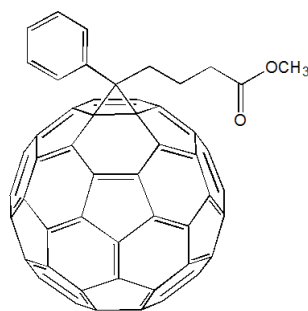


Figure 3 Chemical structure of phenyl-C₆₁-butyric acid methyl ester, PC₆₁BM.

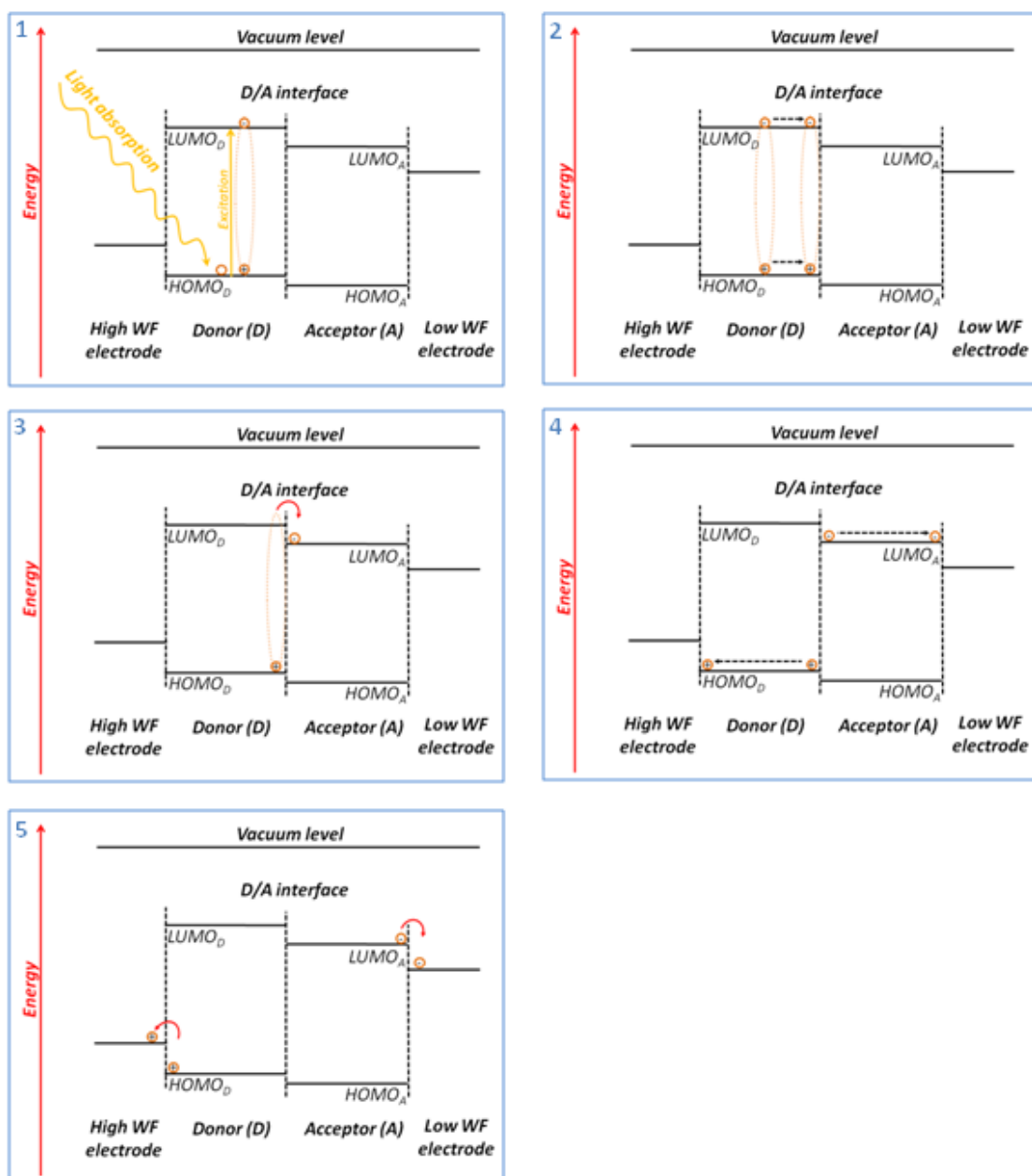
For this reason, in this thesis, the type of organic photovoltaic active BHJ composite studied is the polymer:fullerene blend. The typical fullerene derivatives soluble derivatives PC₆₁BM and PC₇₁BM (analogous of the former, with a C₇₀ core instead of C₆₀ one) will be the only molecular acceptor species analyzed in this work, while many different conjugated polymers will be studied and applied (see Chapter II).

3. WORKING PRINCIPLES IN BHJ OPV DEVICES

For a deeper analysis on the strength and weak point of the OPV technology and of the possible solutions that research could offer for this technology improvements, a better understanding on the basic working principles in BHJ OPV devices is given in this Section.

As represented in **Scheme 3**, the functioning of BHJ OPV devices under illumination can be divided into 5 steps: light absorption with exciton formation, exciton diffusion to the donor/acceptor interface, exciton dissociation into free-charges, free-charges transport through the donor or acceptor phases to the interface with the electrodes, free-charges collection at the electrodes.^[27] It has to be noted that light absorption, in this schematization, only involves the donor material. Indeed in BHJ OPV devices, the main light absorber is in most cases the organic electron donor material, since the absorption coefficient and spectral coverage in the visible range of traditional electron accepting organic materials is usually much lower than those of their electron donor counterpart.

In the following sections we try to analyze more in detail each step of the functioning of BHJ OPV devices under illumination.



Scheme 3 Schematic representation of the steps occurring in BHJ OPV devices.

3.1. Light absorption and exciton formation

Light absorption mainly involves the D/A blend layer and within D and A the strongest absorbing material is often the former one. The incident photons penetrate into the device and reach the photoactive layer, which absorbs light with a certain efficiency.

The efficiency of light absorption depends first on the optical absorption coefficient of D and A in the film, which is strictly correlated to their molar absorptivity or molar extinction coefficient (the intrinsic capacity of light absorption by a single molecule), their density (the number of molecules for volume unit) and their absorption cross section (the orientation of the absorbing molecules comparing that of the incident light electromagnetic field). The

absorption coefficient varies with wavelength depending on the distribution and density of the electronic and vibrational energetic states of the organic material, and on the transitions moments associated with them. Moreover, it is limited by the semiconductor bandgap, defined by the difference between its LUMO and HOMO levels (the smallest difference between the ground and excited electronic states bands)^[28] in such a way that only photons with energy $> E_g$ can be absorbed.

Therefore, the strategies for the enhancement of the absorption coefficient of organic materials involve an accurate tuning of its molecular electronic structure and its intermolecular packaging and ordering in the photoactive film. Some of these strategies will be discussed in more detail in Chapter II. However, in general, the absorption coefficient is much higher for organic materials than for Si, so that usually about 100 nm thin active films are sufficient to absorb between 60% and 90% of the incident light, if a reflective back contact is used.

The second factor influencing the device absorption efficiency is the light pathway length inside the photoactive film. This mainly depends on the film thickness which, as discussed before, is limited by the typical low charge carrier and exciton mobilities of organic materials. Other factors influencing the light penetration and pathway inside the active layer are reflection, refraction and scattering at the interfaces within the device layers and at the device/air interface. In particular, reflection could causes optical losses, while an accurate managing of scattering and refraction phenomena inside the device could lead to enhanced photoactive layer light absorption. Some strategies for light managing in BHJ OPV devices will be discussed in Chapter V.

The third factor determining the light absorption efficiency of the photoactive layer of a solar cell is the overlap between its absorption spectrum and the solar radiation one. The extraterrestrial solar radiation (Air Mass 0, or AM0)^[29] consists in a flux of photons emitted with a distribution of energies similar to the emission of a black body at 5960 K, while at the Earth level, being filtrated by the atmosphere, it still has similar spectral features, with some wavelength regions being attenuated (Air Mass 1.5, or AM1.5)^[30] (see **Figure 4**).

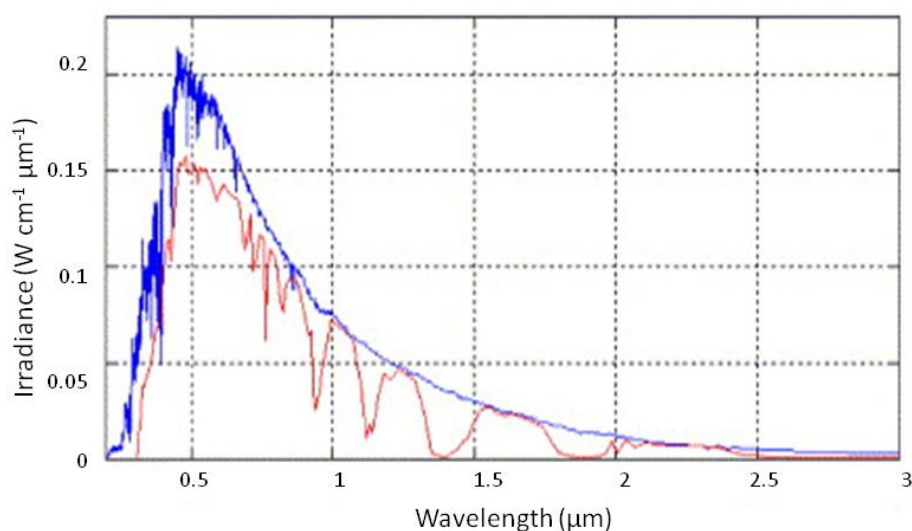


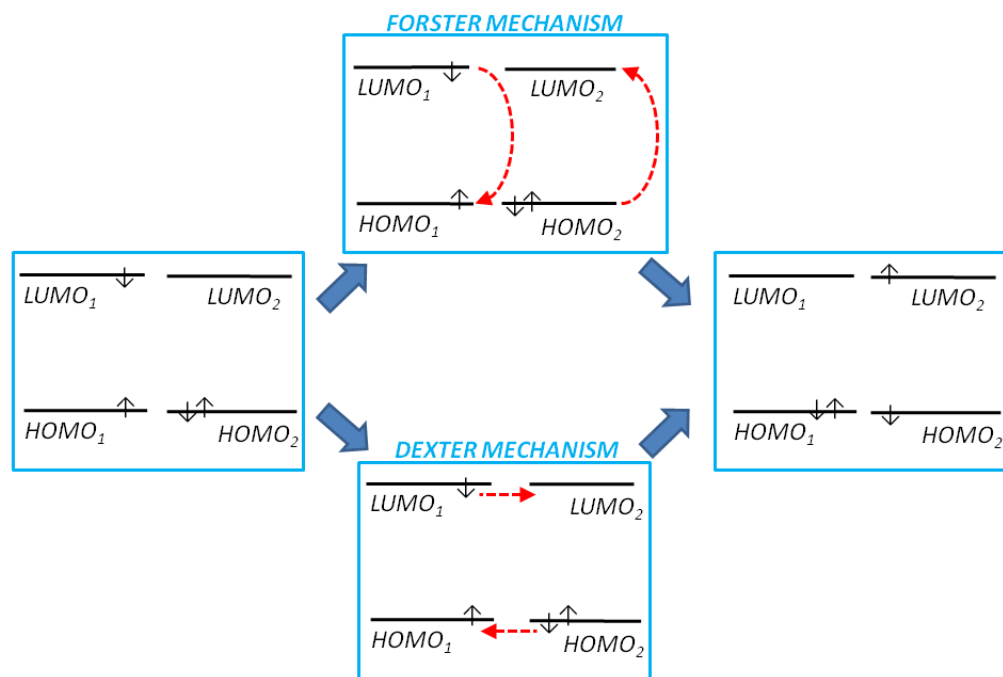
Figure 4 Extra-terrestrial solar spectrum (Air Mass 0, or AM0, blue line) and terrestrial solar spectrum (Air Mass 1.5, or AM1.5, red line).

As it can be seen, around a half of the total light power lies in the infrared region, in the range of low energy radiations. Since the solar radiation absorption by the active layer is determined by the overlap between the solar photons flux and the absorption coefficient integrated over energies $> E_g$, another strategy for the absorption enhancement is the lowering of the semiconductors band gaps. Some of these strategies will be discussed in more detail in Chapter II and in Chapter IV.

Light absorption promotes the electrons lying in the ground state to one of the excited states of the organic semiconductor, with the formation of the Frenkel exciton. The separation of the exciton into free charges can occur only if a driving force sufficient to overcome the coulombic attractive energy (E_B) between the exciton electron-hole pair is present.

3.2. Exciton diffusion to the donor/acceptor interface

The condition for exciton separation into free charges can occur only if the exciton is allowed to *diffuse* to the D/A interface dissociation sites. The exciton, mainly formed in the D phase, diffuses as long as geminate recombination processes (between the electron and hole which make up the exciton) do not take place. Dexter (between adjacent molecules) or Forster (long range) energy transfers can take place between an excited donor molecule, considered as an energy donor, and another molecule that receives the excitation energy, considered as an energy acceptor, as illustrated in **Scheme 4**.^[15]



Scheme 4 Schematic representation of the Forster and Dexter energy exchange mechanisms within two molecules (1 and 2) with HOMO₁, LUMO₁ and HOMO₂, LUMO₂ energy levels respectively.

The Dexter energy transfer occurs through the overlapping of the electron clouds of the frontier orbitals of two neighboring molecules (represented as LUMO₁, LUMO₂, HOMO₁ and HOMO₂ in the scheme). This mechanism does not rest upon allowed electronic transition probabilities, but the total spin of the system must be conserved during the energy transfer. The energy transfer (or exciton diffusion) through Dexter mechanism has an efficiency that decays exponentially with distance, thus it can occur only within very short distances (in the order of 0.3–2 nm).

On the other hand, the Forster energy transfer occurs through non-radiative dipole-dipole coupling between an excited donor molecule and an energy-accepting donor molecule. Spins of both molecules involved are conserved during Forster energy transfers, under a condition imposed by allowed dipolar electronic transitions. The efficiency of the Forster energy transfer is inversely proportional to the sixth power of the distance, thus it is a longer-range process comparing to the Dexter one, and occurs within distances in the order of 3–10 nm.

The D domain size in BHJ devices, then, should be kept approximately in the same range of the efficient excitons diffusion length determined by the described energy transfer processes, in order to effectively compete with the various exciton recombination mechanisms that will be discussed in the following sections. Exciton diffusion lengths in typical organic polymeric or molecular donor phases in BHJ OPVs ranges from around 5 nm^[31] to more than 100 nm (only in a few cases, i.e. some perylene derivatives).^[32]

3.3. Charge separation at the donor/acceptor interface

Excitons surviving to recombination processes are allowed to diffuse into the D or A phases and reach the D/A interface. If the energy difference between the ionization potential IP_D of the electron donating material and the electron affinity EA_A of the electron acceptor material is larger than the exciton binding energy E_B , that is usually 0.1-0.2 eV, exciton dissociation is energetically favorable. This can be resumed in **Equation 1** as:

$$IP_D - EA_A - E_B < 0 \quad \text{Eq. 1}$$

The charge transfer at the D/A interface is typically very fast and very efficient,^[33] occurring usually within a time range < 100 fs. After exciton dissociation, the hole stays on the donor molecule while the electron is transferred on the acceptor molecule. Thus, charge carriers are spatially separated, residing on two separate molecules, this leading to lowered recombination rates (occurring within micro- to milliseconds time ranges) as compared to the recombination of Frenkel excitons (occurring within time ranges of nanoseconds). Nonetheless, the positive and negative charges are still bound by Coulombic attractive forces. Therefore, a further step is necessary for the final charge pair dissociation.

To overcome the coulombic attraction between the electron-hole pair, spatially separated but still bound at the D/A interface, an electric built-in field is needed. This internal field is mainly determined by the different work-functions of the electrodes at the two sides of the device. If this difference is too low, geminate recombination of the charges pair is very probable.^[34] On the other hand, if the field supported charge carrier separation is successful, electrons and holes can diffuse and be transported towards their respective contacts, in order to generate a photocurrent.

3.4. Charge transport in the D and A phases

The charge transport mechanism in organic semiconductors depends on the degree of order of the molecular species in the BHJ film. Charge transport mechanisms can be divided into two general classes: band or hopping transport.

As discussed before, band transport is the mechanism typically observed in inorganic semiconductors, where charges are delocalized over the electronic states constituting the conduction band of the semiconductor. With this mechanism, charge transport occurs without important energy losses. A similarly efficient band transport mechanism takes place in highly purified molecular crystals (even though the presence of traps significantly deviates from such a behavior), for which, at room temperature, conductivity values in the range 1 to 10 $\text{cm}^2/\text{V}\cdot\text{s}$ can be achieved.^[35]

In the opposite case, such as in amorphous organic semiconductors, the conductive electronic states are more localized rather than consisting in electronic

bands. Thus charges, mainly localized on a single molecule rather than delocalized over a crystalline lattice, polarize and distort the surrounding lattice forming the polarons. The mechanism by which charge carrier transport (or polaron diffusion) occurs between adjacent molecules is the thermally activated hopping transport.^[15b] Comparing to band transport, this mechanism is generally less efficient and is responsible of the much lower charge mobility of amorphous organic solids (usually lower than 10^{-2} cm²/V·s)^[16] comparing to that of crystalline organic and inorganic semiconductors.

Since semiconducting organic films used in BHJ OPV devices are generally amorphous or semi-crystalline, the hopping charge transport mechanism usually prevails.

Another important limiting factor, in BHJ OPV devices, for the charge transport of free charges from the exciton dissociation sites to the electrodes, resides in the intrinsic morphological features of the D and A phases, characterized by finely intermixed and contorted domains of the two materials. The necessity to have a photoactive film thickness in the order of hundreds of nm to guarantee a high incident light absorption, and the requisite of a fine D and A phases intermixing to guarantee a high D/A interfacial area for high charge separation yields, is difficult to combine with the need to have bi-continuous D and A phases in order to ensure an efficient free charges transport from the D/A interface to the contact electrode. To fulfill all these requirements, the accurate control of the BHJ morphology is one of the most challenging key issues in the preparation of efficient devices.

3.5. Charge collection at the electrodes

For the collection of free charges at the respective positive and negative electrodes to occur, the work-function of the cathode should have a lower energy than the LUMO_A level and the work-function of the anode should have a higher energy than the HOMO_D level. The differences between the WF of the electrode and the LUMO_A or HOMO_D energies determine whether there are ohmic or blocking contacts for the injection of charges at the corresponding electrodes. When the electrode/organic contact is non-ohmic, the interfacial energy level alignment between the organic frontier orbitals and the WF of the contacts could cause electrical losses for the device, while for ohmic contacts a charge collection at the electrodes with higher efficiency could be expected.^[22]

Common electrode materials used as electron collecting contacts (low WF required) in BHJ OPV devices are Al, Ca, and Ag, and their charge extraction ability is more or less efficient depending on the kind of organic electron transporting material. For example, an ohmic contact is known to form between the WF of Ca and the LUMO_A of PCBM, the most common electron acceptor used in BHJ OPVs. On the other hand, high WF materials like Au are preferred as hole collecting contacts.

Since one contact has to be at least partly transparent for light penetration into the device, very thin metal layers could be used (e.g. about 15-20 nm of Au). Alternatively, Indium Tin Oxide (ITO), a semiconductor made of In₂O₃ (90%) and

SnO₂ (10%), transparent to visible light due to its high bandgap (around 3.7 eV) and highly conductive due to its oxygen vacancies, is commonly used as transparent electrode.^[36]

Many different interactions at the organic/electrode interface could occur, depending not only on the respective organic and electrode energy levels alignment, but also on their physical and chemical characteristics. Such interactions involve dipole formation, wavefunction hybridization, charge transfer, chemical reactions, physical intermixing, etc.^[37] All these factors affect the mechanisms and efficiency of the charge extraction process at the electrodes. For example, a thin oxide layer formed at the metal interface due to impurities or adsorbed species on the organic material constitutes a potential barrier for charges extraction. In addition, the high thermal energy of the metal, which is often deposited onto the organic layer by evaporation, could cause some “hot” metal atoms and clusters to diffuse into the organic layer and create non-geminate charge recombination sites, or could result into possible damage of the organic material due to high metal condensation energies. Moreover, also the selectivity of the electrodes towards only positive or negative charges should be guaranteed in order to minimize the non-geminate recombination of charges due to non-selective charges extraction at the BHJ film/electrode interface. For all these reasons, a thin intermediate layer, also called as buffer layer, is often interposed between the organic BHJ film and the metal electrode.^[38] Buffer layers typically consists of semiconductor films forming selective ohmic contact with the LUMO_A (cathode) or with the HOMO_D (anode). In addition, buffer layers often work also as protective barrier, as energy level pinner, as surface flattener and also as optical spacer. Some typical anode buffer layers are the polymeric PEDOT:PSS and some metal oxides such as MoO₃ and V₂O₅, while typical cathode buffer layers are LiF, TiO₂ and ZnO. A deeper study on different kind of buffer layers will be given in Chapter III.

4. FUNDAMENTAL PHOTOVOLTAIC PARAMETERS

4.1. Equivalent circuit of BHJ OPV devices

To better understand the functioning of a solar cell, it is useful to represent it with an equivalent circuit. Indeed, the solar cell can take the place of a current generator in a simple electric circuit, as represented in **Figure 5**.^[39]

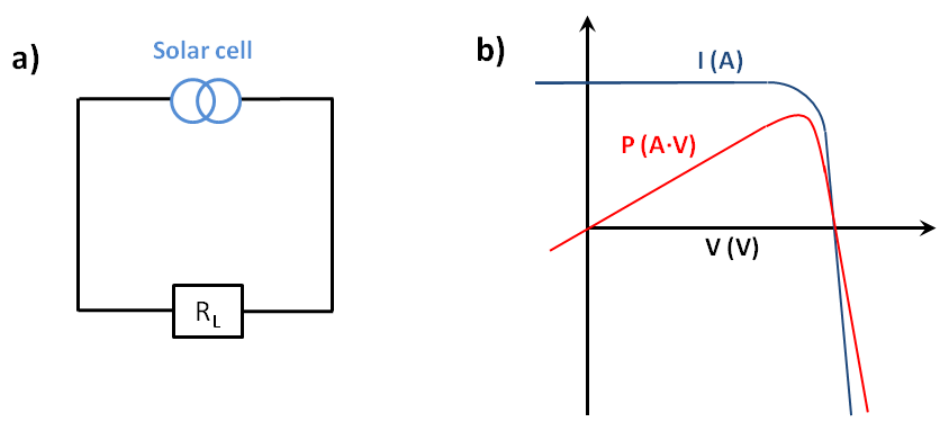


Figure 5 a) Schematic representation of the equivalent circuit of a solar cell; **b)** I-V and P-V curves of a typical solar cell.

When light illuminates the cell, it develops a potential difference which: when the terminals are isolated (infinite load resistance, or R_L) is open circuit voltage, or V_{oc} ; when the terminals are connected and the circuit is closed, the current drawn is called as the short circuit current, or I_{sc} . For any intermediate R_L , the cell develops a voltage V comprised between 0 and V_{oc} and delivers a current I such that $V = I \cdot R_L$. The $I(V)$ behavior is determined by the current-voltage characteristic of the cell under illumination (blue curve in **Figure 5b**), which varies with the incident light intensity and also with R_L . Since the current is roughly proportional to the illuminated area, the current density J is often used instead of I (and correspondingly J_{sc} instead of I_{sc}). This is the simplest, ideal diode model of a solar cell.

The operating regime of the solar cell is the range of bias, from 0 to V_{oc} , in which the cell produces power (red curve in **Figure 5b**), with a power density given by **Equation 2**:

$$P = I \cdot V \tag{Eq. 2}$$

At $V < 0$ and $V > V_{oc}$ the illuminated device consumes power to generate current. The R_L load of the circuit to which the cell is connected develops a potential difference between the device terminals even when the cell is not illuminated. This potential difference generates a current which acts in the opposite direction to the photocurrent produced under illumination, and the net current flowing in the circuit is then reduced from its short circuit value. This reverse current is usually called the dark current, or $I_{dark}(V)$ ($J_{dark}(V)$ if considering the current density). Since most solar cells behave like a diode in the dark, showing a rectifying behavior due to their asymmetric junction, their dark current density $J_{dark}(V)$ varies like the one of an ideal diode, as in **Equation 3**:^[40]

$$J = J_0 \left(e^{\frac{qV}{k_B T}} - 1 \right) \tag{Eq. 3}$$

where J_0 is the reverse current, k_B is Boltzmann's constant, q is the electron elementary charge and T is temperature in Kelvin degrees.

The overall $I(V)$ response of the cell, its current-voltage characteristic, can be approximated as the sum of the short circuit photocurrent and the dark current. This step is known as the superposition approximation. Although the reverse current which flows in an illuminated cell is not formally equal to the current which flows in the dark, the approximation is reasonable for many photovoltaic materials.

The net current density in the cell is then described by **Equation 4**:

$$J(V) = J_{sc} - J_{dark}(V) \tag{Eq. 4}$$

which becomes **Equation 5** for an ideal diode:^[41]

$$J = J_{sc} - J_0 \left(e^{\frac{qV}{k_B T}} - 1 \right) \tag{Eq. 5}$$

Since empirically the real diode behavior deviates from the ideal diode relation, an ideality factor has to be introduced, leading to **Equation 6**:^[42]

$$J = J_{sc} - J_0 \left(e^{\frac{qV}{\xi k_B T}} - 1 \right) \tag{Eq. 6}$$

where ξ is the ideality factor, which i.e. for silicon based diodes is usually $1 < \xi < 2$.

Also BHJ OPVs deviate from ideality and by analyzing their deviations we can upgrade the equivalent circuit of the cell to a more representative one and define other significant parameters better describing the solar cell behavior.

The simplest extension of **Equation 6** to better describe the real BHJ OPV device functioning consists in introducing losses through a series resistance R_s and a parallel resistance R_p .^[40] R_s represents contact resistances such as ohmic losses in the front and rear contact. R_p includes any current bypassing the D/A interface as well as shunt currents through shorts. Based on **Equation 6** this leads to **Equation 7**:

$$J = J_{sc} - J_0 \left(e^{\frac{q(V-IR_s)}{\xi k_B T}} - 1 \right) + \frac{V-IR_s}{R_p} \tag{Eq. 7}$$

The equivalent circuit of a real BHJ OPV device can be upgraded by adding R_s and R_p and represented as in **Figure 6**.

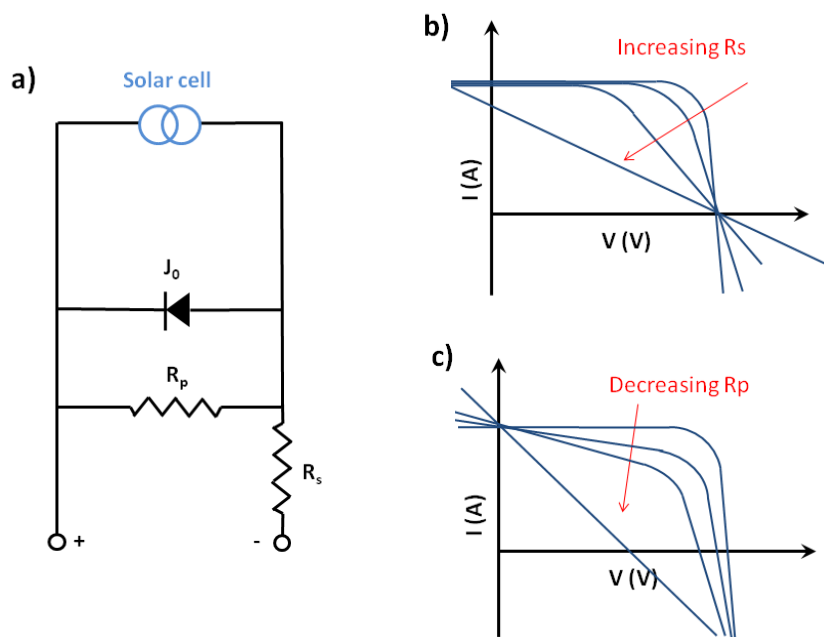


Figure 6 a) Schematic representation of the equivalent circuit of a real BHJ OPV device; **b)** evolution of the I-V curves of a solar cell with increasingly high R_s ; **c)** evolution of the I-V curves of a solar cell with gradually lower R_p .

The real $I(V)$ behavior of a BHJ OPV is substantially modified by the two resistors R_s and R_p in such a way that the voltage V drops over the serial resistance R_s , whereas the shunt R_p resistance adds the current $I_p = (V - IR_s)/R_p$ to the cell output current. The overall effect on the increase of R_s or the decrease of R_p on the $I(V)$ characteristics of the cell is resumed in **Figures 6b** and **6c** respectively.

4.2. I-V curves: PCE, I_{sc} , V_{oc} , FF

The most important parameters of a photovoltaic cell, directly derivable from the cell $I(V)$ curve, are: the short-circuit current I_{sc} , the open circuit voltage V_{oc} , the fill factor FF and the power conversion efficiency (PCE).

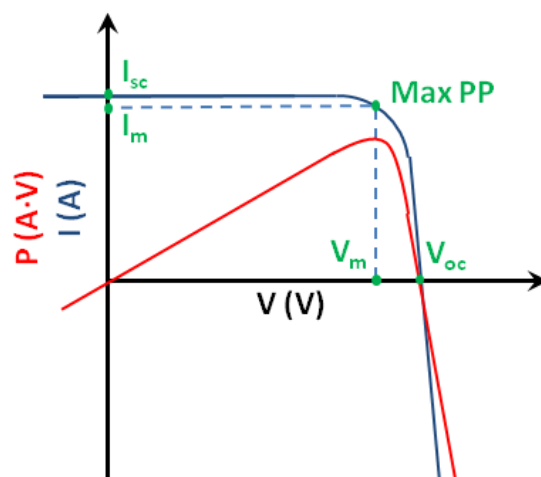


Figure 7 Schematic representation of the most important parameters derivable from the $I(V)$ and $P(V)$ curves of a solar cell under illumination.

In **Figure 7** the typical $I(V)$ and $P(V)$ curves of a solar cell are represented, together with the described parameters.

As discussed before, V_{oc} is the voltage at which no current flows through the solar cell. For traditional single junction inorganic solar cells, V_{oc} is mainly determined by the band gap of the absorbing semiconductor, although being limited by the recombination of charges through radiative processes, as firstly hypothesized by Shockley and Queisser in 1961.^[43] On the opposite, in BHJ OPVs charge separation at the D/A interface occurs very efficiently. Due to this, as demonstrated by several studies,^[44] in BHJ OPV devices the V_{oc} strongly depends on the energy difference between the HOMO_D-LUMO_A offset at the D/A interface of the cell, rather than on the D band gap. In addition, the experimental values for V_{oc} can differ from those inferred from that difference, depending on the D/A blend morphology and on the electrodes morphology and nature.^[45] In fact, differently from the Shockley and Queisser theory, since severe quenching of the excited states occur at the D/A interface by effective charge separation processes, charge losses mainly occur by non-radiative recombination pathways instead of radiative ones.^[46]

As discussed before, J_{sc} is the current flowing through the solar cell when $V = 0$. At a certain photon flux, J_{sc} primarily depends on the property of the D material to absorb light and create excitons, this being in turn determined by the material absorption coefficient and band gap, and on the exciton diffusion at the donor/acceptor interface which varies with the materials exciton diffusion lengths. Secondly, J_{sc} also depends on the carrier mobility in the D and A phases, thus on their electrical conductivity and morphology in the BHJ film.

The maximum electric power produced by the OPV cell under illumination is the maximum of the power curve (P_{max}) and corresponds to the maximum power point (MPP) in the $I(V)$ curve. At the MPP, the cell produces a certain I_m under an applied voltage of V_m . The ratio between the maximum power obtained by the cell ($I_m \cdot V_m$,

or P_{\max}) and the theoretical maximum power that could be obtained from the cell ($I_{sc} \cdot V_{oc}$) is called the fill factor FF, calculated as in **Equation 8**:

$$FF = \frac{P_{\max}}{I_{sc} \cdot V_{oc}} \quad \text{Eq. 8}$$

The FF is therefore an indicator of the quality of a photovoltaic cell. In fact it represents the deviation of the $I(V)$ behavior of the cell from ideality. These deviations are significantly affected both by the ideality factor (ξ) of the cell and also by its electrical resistances (R_s and R_p). Indeed, increasingly higher R_s and lower R_p lead to lower FF and consequently lower cell efficiencies. Strategies to decrease the contact resistances (thus lowering R_s) include the accurate choice and processing of the buffer layers and electrodes, while the strategies to decrease the shunt currents bypassing the D/A interface (thus increasing R_p) involve the improvement of the BHJ morphology as well as the control and tuning of the energetic and kinetics involved in the charge separation process. Both these strategies are usually employed in the optimization of FF and efficiency of BHJ OPV cells.

The solar cell power conversion efficiency is the ratio of the electrical output of a solar cell to the incident light power to which the cell is exposed. This is calculated by dividing output power density at its maximum power point (P_m , in W/m^2) by the incident light irradiance (P_L , in W/m^2), as in **Equation 9**:

$$PCE = \frac{P_m}{P_L} = \frac{I_{sc} \cdot V_{oc} \cdot FF}{P_L} \quad \text{Eq. 9}$$

The PCE measured in standard temperature (25°C) and illumination conditions (incident radiation $P_L = 100 \text{ mW/cm}^2$ and AM1.5 spectral shape) is the conventional efficiency (η) value given for any solar cell.

4.3. Quantum efficiency

Another important photovoltaic parameter characterizing solar cells is the External Quantum Efficiency (EQE), also called incident-photon-to-current efficiency. EQE is defined as the ratio between the number of photoinduced charges extracted out of the solar cell (N_e) and the number of incident photons (N_{ph}), as in **Equation 10**:

$$EQE = \frac{N_e}{N_{ph}} \quad \text{Eq. 10}$$

Since the number of photons coming from any source (included the sun) is dependent on the photons energy, therefore on the radiation wavelength, usually the EQE values for a determined solar cell are given as a function of wavelength λ , and $EQE(\lambda)$ is also called the spectral response.

The EQE(λ) can be directly determined from the short-circuit current $I_{sc}(\lambda)$ of the cell illuminated at each wavelength λ and the incident light intensity $J_i(\lambda)$ at the same wavelengths, by **Equation 11**:

$$EQE(\lambda) = \frac{N_e}{N_{ph}} = \frac{I_{sc}(\lambda)}{J_i(\lambda)} \cdot \frac{hc}{\lambda q} \quad \text{Eq. 11}$$

where c is the speed of light and h is the Planck constant. Therefore, the convolution of EQE(λ) over the entire λ range of the incident radiation spectrum, gives the total photocurrent of the cell (I_{sc}).

The EQE is smaller than the internal quantum efficiency (IQE), which represents the conversion of absorbed photons into charges within the cell, because in EQE the light absorption capability of the active layer and the possible losses due to reflection and scattering are also taken into account. For this reasons EQE is usually far from unity for most BHJ OPV cells.

5. LIMITING FACTORS IN BHJ OPV DEVICES EFFICIENCY

Before presenting the aim of this work, a brief resume of the main loss factors and mechanisms during BHJ OPV devices functioning should be given. The losses within any D/A heterojunction solar cell may be grouped into three categories: i) relaxation of excitons which fail to diffuse to, and separate at, the D/A interface; ii) recombination of geminate electron-hole pairs formed at that interface which fail to fully dissociate into free charge carriers (called geminate recombination); iii) recombination between dissociated carriers generated by different absorption events (called non-geminate recombination). The latter loss mechanism encompasses all those recombination processes involving carriers facing the “wrong” electrode (surface recombination, or leakage) and processes involving the recombination of oppositely charged carriers diffusing through the bulk, often referred to as bimolecular recombination.^[47]

In BHJ OPV cells with coarse, sub-optimal D/A blend morphology, exciton recombination in the D or A phase far from the D/A interface could be an important efficiency limiting factor, this usually leading to low photocurrents.

On the other hand, in most nanomorphology-optimized bulk heterojunction solar cells, the efficiency of the D exciton quenching by A species at the D/A interface is close to unity. This implies that after a fine tuning of the BHJ active layer processing conditions, exciton diffusion is not usually a strongly limiting process.^[48] Under short-circuit conditions, non-geminate losses are generally observed to be very low,^[49] therefore in this condition the main loss mechanism leading to sub-optimal external quantum efficiency is primarily the geminate recombination one.^[50] On the other hand, away from short-circuit conditions and particularly close to V_{oc} , a combination of geminate and non-geminate recombination losses mechanisms are expected to shape the solar cell J-V behaviour. In detail, as the operating condition is moved from short-circuit to

open-circuit, the macroscopic electric fields present in the device due to electrode charge tend to zero ('flat band' conditions). This reduction in internal electric field results in a retardation of the charge carrier extraction time at the electrodes, which leads to an increase in the steady state charge carrier density in the photoactive layer towards open-circuit. This increase in charge carrier density can result in an important increase in non-geminate recombination losses as the cell voltage is increased. It has been shown that these non-geminate losses may be quantified as a function of bias and light intensity and used to understand the light-intensity dependence of FF and V_{oc} in many BHJ OPV cells.^[51] It should also be considered that the reduction of the internal electric field close to open-circuit conditions influences also the dissociation efficiency of photogenerated charge carrier pairs; therefore the magnitude of geminate recombination may be directly dependent upon this field, and therefore upon cell voltage.

Many investigation techniques aiming to quantify voltage-dependent geminate recombination and charge density dependent non-geminate recombinations, limiting the J_{sc} , V_{oc} and FF of BHJ solar cells have been developed and successfully applied to many small molecule- or polymer-based BHJ OPVs, those techniques including transient photovoltage measurements, charge extraction measurements, transient absorption spectroscopy and impedance spectroscopy.^[47,52] These analysis allow to correlate the V_{oc} with the materials energetics (ionization potential of the donor and electronic affinity of the acceptor), the charge photogeneration efficiency and the recombination kinetics. As such, the deep study on the described loss mechanisms are an effective tool for achieving the systematic optimization of the performances of OPV devices.

6. THE AIM OF THIS WORK: STRATEGIES TO IMPROVE THE BHJ OPV CELLS PERFORMANCES

This work is focused on the characterization and optimization of BHJ OPV devices, in particular those where the active layer is made of polymeric donor materials and standard fullerene-based acceptor materials. The thesis is divided into chapters, each one treating different aspects that are critical in determining the performances of BHJ OPV, such as the device materials, architecture or implementation of additional functional components.

Chapter II is focused on the optimization of the performances of BHJ OPV devices by the accurate study and tuning of the properties of the polymeric donor material employed. In particular, the strategy of using co-polymers with electron withdrawing and electron donating alternate units is explored. A study on two different families of co-polymers is presented. The tuning of the chemical structure of the monomeric units, inter-moieties spacers and solubilizing side-groups is shown to effectively modulate the polymer optical, electrical, morphological, and photophysical properties. These properties are then correlated with the performances of the corresponding BHJ OPV devices, which are fully optimized and characterized.

In Chapter III the work is focused on the optimization of the BHJ OPV cells performances by a deeper study on the role of buffer layers employed in the devices. To this aim, active layers made of poly(3-hexylthiophene) (P3HT) and PC₆₁BM as standard and deeply studied in literature donor:acceptor couple are employed. The study focuses on two different semiconducting metal-oxides, such as TiO_x and ZnO, employed as cathode buffer materials, while PEDOT:PSS is used in any case as anode buffer layer. The optical, morphological and electrical properties of these materials have been investigated and their functioning as thin film buffer layers in inverted structure BHJ OPVs devices is analyzed and compared with the reference P3HT:PCBM-based devices made by employing LiF/Al cathode and ITO/PEDOT:PSS anode.

In Chapter IV an overview of the light managing techniques that possibly improve the solar cell light absorption is given. A deeper study on the technique of light trapping inside the device, obtained by using a scattering material in the device architecture, is applied in standard P3HT:PCBM based devices.

The methods and techniques for the preparation and characterization of materials and devices, the discussion of results, the bibliographic references and some conclusions are specified in each chapter, while general conclusions of the thesis work and future perspectives are given in Chapter V.

7. BIBLIOGRAPHY

- [1] (a) V. Smil, *Energy Transitions: History, Requirements and Prospects*, Ed. ABC-CLIO, 2010; b) BP Statistical Data , www.bp.com.
- [2] (a) N. Armaroli e V. Balzani, *Energia oggi e domani: prospettive, sfide, speranze*, Bononia University Press, 2004; (b) N. Armaroli e V. Balzani, *Energia per l'astronave Terra*, Ed. Zanichelli, 2011.
- [3] R. Williams, *The Journal of Chemical Physics*, 32 (5), 1960, 1505.
- [4] (a) W.G. Adams, R.E. Day, *Proc. R. Soc. London*, 25, 1876, 113. (b) Z. A. Smith, K. D. Taylor, *Renewable and Alternative Energy Resources: A Reference Handbook* , ABC CLIO, 2008.
- [5] W. Schottky, *Phys. Z.*, 41, 1940, 570.
- [6] D. M. Chapin, C. S. Fuller, G. L. Pearson, *J. Appl. Phys.*, 25, 1954, 676.
- [7] A.Pochettino, *Acad. Lincei Rend.*, 15, 1906, 355.
- [8] M.Volmer, *Ann. Physik*, 40, 1913, 775.
- [9] R.H. Bube, *Photoconductivity of Solids* , Ed. John Wiley & Sons Ltd, 1960.
- [10] (a) S. Anthoe, *Rom. Rep. Phys.*, 53, 2002, 427; (b) A. Chamberlain, *Sol. Cells*, 8, 1983, 47.
- [11] S. S. Hegedus, A. Luque, *Handbook of Photovoltaic Science and Engineering*, Ed. John Wiley & Sons Ltd, 2003.
- [12] (a) J. Frenkel, *Phys. Rev.*, 54, 1938, 647; (b) M. Fox, *Optical properties of solids*, Oxford University Press, 2001.
- [13] I. G. Hill, A. Kahn, G. Soos, R. A. Pascal. *Chem. Phys. Lett.*, 327, 2000, 181.
- [14] X.-Y. Zhao, H.-J. Liu, *Polym. Int.*, 59, 2010, 597.
- [15] (a) I. Bruder, *Organic solar cells: Correlation between molecular structure, morphology and device performance*, PhD thesis, Max-Planck-Institut für Festkörperforschung 2010; (b) E.A. Silinsh, V. Capek, *Organic molecular crystals - interaction, localization and transport phenomena* , American Institute of Physics, 1994.
- [16] C. Guo, W. Hong, H. Aziz, Y. Li, *Reviews in Advanced Sciences and Engineering*, 1, 3, 2012, 200.
- [17] (a) A.K. Ghosh et al., *J. Appl. Phys.*, 45, 1974, 230; (b) B.R. Weinberger et al., *Synth. Metals*, 4, 1982, 187; (c) S. Glenis et al., *Thin Solid Films*, 139, 1986, 221; (d) S. Karg et al., *Synth. Metals*, 54, 1993, 427.
- [18] C. W. Tang, *Appl. Phys. Lett.*, 48, 1986, 183.
- [19] (a) G. Yu, J. Gao, J. C. Hummelen, F. Wudl, A. J. Heeger, *Science*, 270, 1995, 1789; (b) H. Spanggaard, F. C. Krebs, *Sol. Energy Mater. Sol. Cells*, 83, 2004, 125; (c) G. Yu, K. Pakbaz, A.J. Heeger, *Appl. Phys. Lett.* , 64, 1994, 3422; (d) D. Gebeheyu, F. Padinger, T. Fromherz, J.C. Hummelen, N.S. Sariciftci, *Int. J. Photoenergy*, 1, 1999, 95; (e) N. Camaioni, G. Ridolfi, G. Casalbore-Miceli, G. Possamai, L. Garlaschelli, M. Maggini, *Sol. Energy Mater. Sol. Cells*, 76, 2003, 107; (f) P. Schilinsky, C. Waldauf, C.J. Brabec, *Appl. Phys. Lett.*, 81, 2002, 3885.

[20] (a) G. Yu, A. J. Heeger, *J. Appl. Phys.*, 78, 1995, 4510; (b) J. J. M. Halls, C.A. Walsh, N.C. Greenham, E.A. Marseglia, R.H. Friend, S.C. Moratti, A.B. Holmes, *Nature*, 376, 1995, 498.

[21] (a) J. C. Hummelen, B. W. Knight, F. LePeq, F. Wudl, J. Yao, C. L. Wilkins, *J. Org. Chem.*, 60, 1995, 532; (b) M. T. Rispens, A. Meetsma, R. Rittberger, C. J. Brabec, N.S. Sariciftci, J. C. Hummelen, *Chem. Commun.*, 17, 2003, 2116.

[22] S.-S. Sun, L. R. Dalton, Introduction to Organic Electronic and Optoelectronic Materials and Devices, CRC Press, Taylor and Francis Group, 2008.

[23] (a) R. F. Service, *Science*, 332, 2011, 293 ; (b) L. Dou, W.-H. Chang, J. Gao, C.-C. Chen, J. You, Y. Yang, *Adv. Mater.*, 25, 2013, 825; (c) H. Zhou, L. Yang, A. C. Stuart, S. C. Price, S. Liu, W. You, *Angew. Chem., Int. Ed.* 50, 2011, 2995; (d) Y. Liang, Z. Xu, J. Xia, S.-T. Tsai, Y. Wu, G. Li, C. Ray, L. Yu, *Adv. Mater.*, 22, 2010, E135; (e) H.-Y. Chen, J. Hou, S. Zhang, Y. Liang, G. Yang, Y. Yang, L. Yu, Y. Wu, G. Li, *Nature Photon.*, 3, 2009, 649; (f) L. Dou, J. You, J. Yang, C.-C. Chen, Y. He, S. Murase, T. Moriarty, K. Emery, G. Li, Y. Yang, *Nat. Photonics*, 6, 2012, 180; (g) H. J. Son, L. Lu, W. Chen, T. Xu, T. Zheng, B. Carsten, J. Strzalka, S. B. Darling, L. X. Chen, L. Yu, *Adv. Mater.* 25, 2013, 838; (h) W.Tracy, available from:

www.konarka.com/index.php/site/pressreleasedetail/konarkas_power_plastic_achieves_world_record_83_efficiency_certification_fr; (i) R. Nigel, available from: www.heliatek.com/wp-content/uploads/2011/12/111205_PI_Heliatek-with-efficiency-record-for-organic-solar-cell_EN.pdf; (l) T. Pearl, available from: www.polyera.com/newsflash/polyera-achieves-world-record-organic-solar-cell-performance; (m) M. A. Green, K. Emery, Y. Hishikawa, W. Warta, E. D. Dunlop, *Prog. Photovolt. Res. Appl.*, 20, 2012, 12.

[24] N. S. Sariciftci, L. Smilowitz, A. J. Heeger, F.Wudl, *Science*, 258,1992, 1474.

[25] J. C. Hummelen, B. W. Knight, F. Lepeq, F. Wudl, J. Yao, C. L. Wilkins, *J. Org. Chem.*, 60, 1995, 532.

[26] S. E. Shaheen, C. J. Brabec, N. S. Sariciftci, F. Padinger, T. Fromherz, J. C. Hummelen,

Appl. Phys. Lett., 78, 2001, 841.

[27] D. Bagnis, Engineering materials and devices for organic solar cells, PhD thesis, University of Perugia, 2009.

[28] (a) M. C. Scharber et al., *Adv. Mater.*, 18, 2006, 789; (b) A. Gadisa, M. Svensson, M. R. Andersson, O. Inganäs, *Appl. Phys. Lett.*, 84, 2004, 1609.

[29] C. Julian Chen, *Physics of Solar Energy*, Appendix E, Ed. John Wiley & Sons, 2011.

[30] ASTM E927 – 10, <http://www.astm.org/Standards/E927.htm>, Standard Specification for Solar Simulation for Terrestrial Photovoltaic Testing.

[31] (a) P. Peumans, A. Yakimov, and S.R. Forrest. *J. Appl Phys.* , 93(7), 2003, 3693; (b) Y. Terao, H. Sasabe, C. Adachi., *Appl. Phys. Lett.*, 90, 2007, 103515; (c) T. Stübinger and W. Brütting. *J. Appl. Phys.*, 90, 2001, 3632; (d) H. R. Kerp, E. E. van Faassen, *Nord. Hydrol.*, 1, 1999, 1761.

[32] (a) R. R. Lunt, N. C. Giebink, A. A. Belak, J. B. Benziger, S. R. Forrest, *J. Appl. Phys.*, 105, 2009, 053711; (b) H. Marciniak, X.-Q. Li, F. Würthner, S. Lochbrunner, *The Journal of Physical Chemistry A*, 115, 2011, 648.

[33] N.S. Sariciftci, L. Smilowitz, A.J. Heeger, and F. Wudl., *Science*, 258, 1992, 474.

[34] P. Peumans, S.R. Forrest, *Chem. Phys. Lett.*, 398, 2004, 27.

[35] (a) W. Brutting, H. Riel, T. Beierlein, W. Riess, *J. Appl. Phys.*, 89, 2001, 1704 ; (b) W. Brutting, S. Berleb, A. G. Mockl, *Org. Electron. 2*, 2001, 1; (c) H. Riel, T. A. Beierlein, S. Karg, W. Riess, *Organic Light-Emitting Materials and Devices VI*, Ed. Z.H. Kafafi and H. Antoniadis, Proc. SPIE, 4800, 2003, 148; (d) H. Becker, S. E. Burns, R. H. Friend, *Phys. Rev. B*, 56, 1997, 1893; (e) A. L. Burin, M. A. Ratner, *J. Phys. Chem. A*, 104, 2000, 4704; (f) Z. D. Popovic et al., *J. Appl. Phys.*, 89, 2001, 4673.

[36] A. Andersson, N. Johansson, P. Bröms, N. Yu, D. Lupo, W. R. Salaneck, *Adv. Mater.* 10, 11, 1998, 859.

[37] H. Ishii, K. Sugiyama, E. Ito, K. Seki, *Adv. Mater.*, 11, 8, 1999, 605.

[38] (a) R. Steim, F. R. Kogler, C. J. Brabec, *J. Mater. Chem.*, 20, 2010, 2499; (b) R. Po, C. Carbonera, A. Bernardia, N. Camaioni, *En. Environ. Sci.*, 2011, 4, 285.

[39] T. Markvart, L. Castaner, *Solar cells: materials, manufacture and operation*, Elsevier Ltd, First ed., 2005.

[40] J. Nelson, *The Physics of Solar Cells*, Imperial College Press, First Ed., 2003.

[41] (a) W. Shockley, *Bell Syst. Tech. J.*, 28, 1949, 7; (b) C. T. Sah, R. N. Noyce, W. Shockley, *Proc. IRE*, 45, 1957, 1228.

[42] (a) W. Shockley, W. T. Read, *Phys. Rev.*, 87, 1952, 835; (b) R. N. Hall, *Phys. Rev.*, 83, 1951, 228.

[43] W. Shockley, H. Queisser, *J. Appl. Phys.*, 32, 1961, 510.

[44] S. Yamamoto, A. Orimo, H. Ohkita, H. Benten, S. It, *Adv. Energy Mater.*, 2, 2012, 229.

[45] J. C. Blakesley, D. Neher, *Phys. Rev. B*, 84, 2011, 075210.

[46] (a) K. Vandewal, K. Tvingstedt, A. Gadisa, O. Inganäs, J. V. Manca, *Nat. Mater.*, 8, 2009, 904. (b) L. J. A. Koster, M. Kemerink, M. M. Wienk, K. Maturová, R. A. J. Janssen, *Adv. Mater.*, 23, 2011, 1670; (c) K. Vandewal, K. Tvingstedt, A. Gadisa, O. Inganäs, J. V. Manca, *Phys. Rev. B*, 81, 2010, 125204; d) A. F. Nogueira, I. Montanari, J. Nelson, J. R. Durrant, C. Winder, N. S. Sariciftci, C. Brabec, *J. Phys. Chem. B*, 107, 2003, 1567.

[47] D. Credgington, F. C. Jamieson, B. Walker, T.-Q. Nguyen, J. R. Durrant, *Adv. Mater.*, 2012, 24, 2135.

[48] (a) M. Morana et al., *Adv. Funct. Mater.*, 2010, 20, 1180; (b) F. C. Jamieson, E. B. Domingo, T. McCarthy-Ward, M. Heeney, N. Stingelin, J. R. Durrant, *Chem. Sci.*, 2012, 3, 485.

[49] S. R. Cowan, A. Roy, A. J. Heeger, *Phys. Rev. B*, 2010, 82, 10.

[50] T. M. Clarke, A. Ballantyne, S. Shoaee, Y. W. Soon, W. Duffy, M. Heeney, I. McCulloch, J. Nelson, J. R. Durrant, *Adv. Mater.*, 2010, 22, 5287.

[51] D. Credgington, Y. Kim, J. Labram, T. D. Anthopoulos, J. R. Durrant, *J. Phys. Chem. Lett.*, 2011, 2759.

[52] (a) A. Maurano , R. Hamilton , C. G. Shuttle , A. M. Ballantyne , J. Nelson , B. O'Regan , W. Zhang , I. McCulloch , H. Azimi , M. Morana , C. J. Brabec , J. R. Durrant, *Adv. Mater.*, 2010, 22, 4987; (b) D. Credgington, R. Hamilton, P. Atienzar, J. Nelson, J. R. Durrant, *Adv. Funct. Mater.*, 2011, 21, 2744; (c) G. Garcia-Belmonte, J. Bisquert , *Appl. Phys. Lett.*, 2010, 96, 113301.

CHAPTER II: PHOTOACTIVE POLYMERS, THE DONOR MATERIALS

1. POLYMERIC SEMICONDUCTORS AS DONORS IN BHJ OPVS

As a component in the active layer, the donor material serves as the main absorber to solar photon flux, as well as the hole transporting phase. Research on BHJ OPVs has developed into two the two main branches of “polymeric” or “small molecule” solar cells, depending on the macromolecular or molecular nature of the organic semiconductor used as donor (being the acceptor organic material in most cases the small molecule PC₆₁BM or PC₇₁BM).

1.1. Advantages of using polymeric donors over small molecule ones

There are several advantages in using polymeric versus molecular π -conjugated semiconductors. First of all, the processing from solution of polymeric comparing to molecular materials into thin films usually generates smoother and more uniform layers, due to the inferior tendency to aggregation and crystallization of the long macromolecular chains of polymers comparing to small molecules. This enables a great control of the organic film structural and morphological characteristics even at large scale levels, through easy and cheap solvent-based processes. The first techniques employed for the deposition of small molecules-based organic thin films with controlled structural and morphological characteristics, due to their higher tendency to crystallization, were high vacuum and/or high temperature evaporation processes, which are quite expensive techniques difficult to extend to the industrial scale. However, very recently the preparation of efficient small molecules-based BHJ OPV devices by solution-based deposition techniques, thanks to the accurate fine tuning of the materials physical properties through their chemical structure engineering, has been demonstrated and reported in literature.^[1]

An advantage of the use of polymers over small molecules is that solution based printing techniques necessitate a great control of the solution rheological properties, which can be tuned more efficiently for polymer-based solutions rather than for molecular ones, due to the possibility to control polymers molecular weights. Moreover, polymeric crystalline domains are typically much smaller than the length scale of several opto-electronic devices, resulting in isotropic transport characteristics. This results in low device-to-device performance variability, which is particularly important for solar cells reproducibility and integration into solar panels.

Other advantages regard the easiness of fabrication, from solution deposition processes, of the multilayers that usually compose the BHJ OPV stack. This often requires that each stacked layer is inert to the solvents and processing temperatures at which it is subsequently exposed during device manufacture. The

reduced solubility parameter window of polymers and their larger bulk viscosity comparing to molecular solutions, typically increases the probability to find orthogonal solvents for subsequent solution depositions, thus expanding the choice of polymeric materials that can be used in devices.

In addition, since polymers do not vaporize before decomposition and thus have negligible vapor pressure, they are not susceptible to interlayer diffusion during the device fabrication processing or with device aging.

Finally, polymers exhibit the visco-elastic behavior typical of plastic materials. Therefore, the mechanical properties of nanometer-thick polymeric semiconductor films render them potentially compatible with BHJ OPV devices fabrication onto flexible substrates.

1.2. Traditional donor polymers and recent achievements

The first semiconducting polymers used as donors in OPV cells are shown in **Figure 8**.

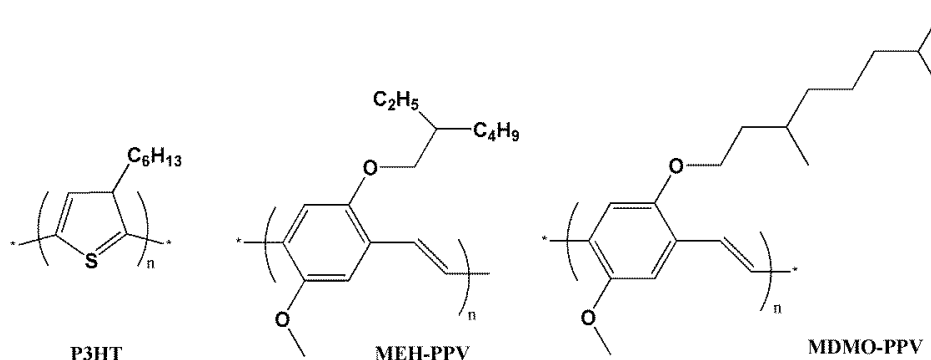


Figure 8 Structures of P3HT, MEH-PPV and MDMO-PPV.

Dialkoxy substituted poly(para-phenylene vinylene)s such as MEH-PPV and MDMO-PPV have been the first class of polymers employed in the OPV technology. While with polymer-only photovoltaic devices efficiencies as low as $10^{-2} - 10^{-3} \%$ were achieved,^[2] the combination of MEH-PPV with an electron acceptor (usually PC₆₁BM) led to a OPV polymer-based device with an impressive enhanced efficiency of 2.9%.^[3] Regioregular P3HT is also a widely studied polymer for its use in BHJ OPV cells. While an initial promising efficiency of $\sim 3\% - 4\%$ was achieved for P3HT:PCBM based cells,^[4] record PCEs $> 6\%$ were reached thanks to the use of different acceptors.^[5] The studies on P3HT, MEH-PPV, and MDMOPPVB based OPV cells paved the way to understanding how bulk-heterojunction OPV cell function and what are the critical parameters affecting efficiency and stability. In particular, many useful models of the OPV devices energetics and kinetics were proposed basing their fundamentals on these studies.

In parallel, a wide number of strategies aimed to the optimization of the active layer morphology in order to improve the device performances have been investigated: the use of solvent mixtures or additives, different photoactive layer

thermal or solvent annealing, controlled film forming conditions and many others.^[6]

Most importantly, the gradual understanding of the functioning of OPV devices and the results coming from the materials optimization flowed into the design of new π -conjugated, promising, donor polymers, resulting in present day efficiency records over 9% (certified).^[7] In the next sections, some of the strategies that have been pursued in order to improve the BHJ OPV device performances by accurately designing and processing new donor polymers are illustrated.

1.3. Requisites for polymeric semiconductors to work as donor in BHJ OPV devices

Polymeric semiconductors for OPV applications must present some essential features. The first one is a highly π -conjugated backbone: the extension of the π -conjugation along the polymer backbone and the enhancement of the intermolecular π - π stack are both known to enable some solution and solid state key properties such as high absorption coefficient and high electrical conductivity.^[8] Moreover, π -conjugation strongly influences other polymer properties such as red-ox potentials and frontier molecular orbital energy levels.^[9]

One of the possible strategies for the extension of the π -conjugation length of the conjugated segments along a polymeric chain is the use of heterocyclic rings, benzofused systems or bridging atom,^[10] helping the polymer backbone planarization through reduced steric effects or increased rigidity. Another strategy is the combination of alternated electron rich and electron poor units in so called “push-pull” or “donor-acceptor” structures, which extending the π -conjugation along the polymer backbone enhances the polymer electrical properties.^[11]

Another essential characteristic of polymeric semiconductors for OPV applications is indeed a suitably low band gap. E_g depends on several parameters encompassing both intra- and intermolecular considerations.^[10] Upon intramolecular parameters, the energy related to the bond length alternation determines a lower E_g for quinoid electronic ground states comparing to aromatic electronic ground states. Moreover, structural deviations from coplanarity of conjugated aromatic rings in the same polymer backbone also determine an increase in the E_g by decreasing the π delocalization. Therefore, polymers with a more rigid backbone with increased monomers coplanarity should have a lower E_g . In addition, in the case of poly(aromatic)s, the delocalization of π electrons along the chain is in competition with their confinement within the aromatic ring. Thus polymers with a lower resonance stabilization energy of aromatic monomers should have an increased delocalization of π electrons along the chain, resulting in a lower E_g . The inductive and mesomeric effects of substituents on the monomeric units also plays an important role in the E_g tuning, other than increasing the polymer conductivity. In particular, electron withdrawing substituents reduce E_g by decreasing the polymer LUMO energy while electron donating substituents reduce the E_g by increasing the HOMO energy. Thus the use of “push-pull”

structures is a very popular method among chemists to obtain low band gap polymers and will be applied also in this work, as illustrated in the following sections.^[11] Finally, also the interchain interactions play an important role in tuning the E_g : intermolecular π and π^* orbitals with a high overlap determine an increase of the width of the polymer HOMO and LUMO bands and contribute to lower E_g .

From an energetic point of view, the pre-requisites of a polymeric semiconductor to be employed as donor in BHJ OPV devices is the suitable positioning of its frontier orbital energies with those of the electron acceptor material composing the BHJ active layer. For example, since the most common electron accepting material family is that of fullerene derivatives, having HOMO and LUMO levels lying around -6.0 and -4.0 eV respectively, a polymer suitably associable with those acceptors should have HOMO and a LUMO levels with energies at least 0.2 eV correspondingly higher.

Another important requirement for polymeric semiconductors to be efficiently applied as donors in BHJ OPV devices is the substitution of their backbone with lateral functional substituents. These substituents play a double role: firstly, they work as solubilizing chains, which are essential for the polymers processing from solutions; secondly, they can enhance the bulk intermolecular interactions in order to help exciton diffusion and electrical conductivity.^[12] The effects of the presence and position of lateral side groups on the backbone of a family of polymers will be analyzed more in detail in the following sections of this chapter.

Other important parameters characterizing and influencing the polymers properties are molecular weight and polydispersity. Polymers, in fact, consist in a distribution of macromolecules with different chain lengths and molecular weights. The polydispersity index (PDI) represents the distribution of the molecular masses of a given polymer sample, while the molecular weight is always given as a weight (Mw) or number (Mn) average within all the molecular weights of that sample. The PDI and Mw (or Mn) of polymers mainly influence solubility, filmability and morphology of both the pristine material and of the blend in BHJ OPVs. Usually, polymers with higher Mn (or Mw) are more difficult to dissolve in solution, but after slow film forming process, usually present higher mobilities. On the other hand, low PDI usually enables a higher reproducibility of the chemical and physical properties of a polymeric film with a certain Mw. In general, the optimal values of Mw or PDI strongly depend on the polymer structure; however, for most polymers a Mn between 20 and 60 kDa and a PDI of 1.2-1.8 are reasonable threshold values.^[13] An example of the effect of a polymer Mw on the corresponding BHJ OPV performance is given in the following sections.

Finally, together with the polymer structural design, the parallel control on the BHJ film morphology is necessary for optimal device performances. In fact, also the active layer film forming process (deposition technique, solvent or solvents mixtures nature, use of additives, thermal or solvent annealing) strongly influences the polymer properties and performance in BHJ OPVs.

In the following sections, some strategies aimed to the optimization of BHJ OPV devices performances by an accurate design and processing of the donor polymers are presented.

2. POLYMERIC DONOR DESIGN AND PROCESSING STRATEGIES TO IMPROVE BHJ OPV DEVICES PERFORMANCES

2.1. A new class of efficient Si-DT-based polymers

An efficient method to extend and enhance the π -delocalization and lower the band-gap of donor polymers is the above mentioned “push-pull” concept, where π -electron-rich (donor) and π -electron-deficient (acceptor) conjugated moieties are combined into the repeating units of the polymer backbone.

In donor-acceptor polymers, the energy and delocalization of the HOMO is mainly determined by the HOMO of the electron poor unit, while energy and delocalization of the LUMO by the electron rich unit. As a result, the photophysical, electrochemical and photovoltaic properties of the polymer can be widely tuned thanks to the large range of ‘push’ and ‘pull’ units that can be used, enabling a fine control of the HOMO and LUMO energies independently. For example, the push-pull polymer approach is used to design polymers with lowered HOMO energy in order to increase device V_{oc} . There is also some evidence that push-pull polymers may allow charge pair separation at a lower driving force comparing to other classes of polymers, maybe owing to the intramolecular charge transfer (CT) features,^[14] between the electron rich and electron poor polymer moieties, of their ground and/or excited electronic states.

Within push-pull polymers, one of the approaches aimed to push down the polymer HOMO include substitution of carbon atoms in the polymer structure by more electron-rich atoms such as sulfur, nitrogen, silicon. This strategy has intensively stimulated the development of the most efficient polymers for OPV devices, leading to devices with efficiencies over 7%.^[15] Among the huge variety of fused hetero-aromatic rings based monomers used in this class of push-pull copolymers, dithieno[3,2-*b*:2',3'-*d*]silole (SiDT, see **Figure 9**) based polymers have attracted much attention due to their intrinsic advantages and potentialities in optoelectronic devices such as organic light emitting diodes (OLEDs)^[16], organic light emitting transistors (OFETs)^[17] and OPV cells.^[18]



Figure 9 dithieno[3,2-*b*:2',3'-*d*]silole (SiDT) unit.

The SiDT electron rich unit is obtained by replacing the carbon bridging atom in fluorene with a silicon atom (Si). Silicon based monomers such as SiDT, analogously to their carbon-based counterparts with aromatic rings bridged together in a condensed configuration, stiffen the polymer backbone leading to a reduced conformational disorder and enhanced interchain π - π interactions. This possibly improves the polymer optical and charge transport properties in the solid state. Additionally, the presence of silicon atoms, that is less electronegative and has more polarizable p atomic orbitals comparing to the C atom, reduces the energy of the molecular π orbitals determining a reduction of the HOMO energy levels. Since, as discussed before, the V_{oc} of a BHJ OPV is proportional to the difference between the HOMO level of the donor material and the LUMO level of the acceptor material, this reduction in the polymer HOMO energy could effectively increase V_{oc} of the resulting BHJ solar cells. Moreover, a lower lying HOMO level could also enhance the chemical stability of the polymer towards moisture oxidizing species. Another effect that could be given by the presence of the Si atom in the SiDT unit is that effective orbital mixing between the silicon's σ^* -orbital and the π^* -orbital of the adjacent butadiene fragment could occur, this leading to a low-lying LUMO and correspondingly lower the band-gap of the SiDT based polymer comparing to a carbon bridged monomeric analogue.^[19] Finally, the tetravalence of the silicon atom in the SiDT unit offers two additional substitution sites for the incorporation of alkyl chains, in order to enhance not only the solubility of the polymer, but also the molecular packing and the interactions between the donor and acceptor materials.^[20]

Recently, several groups have proven the potential of this class of polymers as donor materials for high-efficient BHJ solar cells. For instance, Bazan *et al.*^[21] obtained PCEs of 5.9 %, with open-circuit voltage of 0.57 V, short-circuit current density of 17.3 mA/cm² and fill factor of 61%, using new donor-acceptor (D-A) silole-containing polymers blended with PC₇₁BM. A recent work of Tao^[22] *et al.*, describing a new alternating copolymer of dithienosilole and thienopyrrole-4,6-dione, afforded PCE of 7.3 %, with $V_{oc} = 0.88$ V, $J_{sc} = 12.2$ mA/cm² and FF = 68 %.

In this work the SiDT unit is coupled, to give polymers with push-pull structures, with some thiophene-substituted monomeric units, in particular differently substituted dithiophene (-DT-) or tetrathiophene (-TT-) monomers. 3-substituted thiophenes are one of the most studied moieties used as comonomers^[23] and monomeric units^[24] for semiconductor/optical applications. These semiconductors exhibit unique self-assembly ability and form highly structured thin films when deposited from solution under appropriate conditions. Moreover, they can be easily substituted in position 3 or 4 of the thiophene rings enabling an easy tuning of the polymer physical, chemical and electrical properties. In this work, by increasing the length of the thiophene based comonomer passing from dithiophene (-DT-) to tetrathiophene (-TT-) monomers, additional solubilizing alkyl chains (*n*-dodecyl groups) have been placed on the thiophene rings, in position 3 or 4, in order to improve the overall polymer solubility even at

room temperature and to evaluate their effects on thin films properties and device performance.

In addition, the substitution of electron-rich cyano groups on the oligothiophene units have been tested. Indeed, the presence of the CN groups on the oligothiophene moiety where the HOMO is localized should reduce the HOMO energy of the polymer, enabling greater open-circuit photovoltages comparing to the unsubstituted oligothiophene based polymers.

Therefore, in this section, it is reported the synthesis, characterization and structure-property relationship of a series of novel donor polymers **P(1)-DT-SiDT**, **P(2)-DT-SiDT**, **P(3)-TT-SiDT**, and **P(4)-TT-SiDT** (Figure 10).

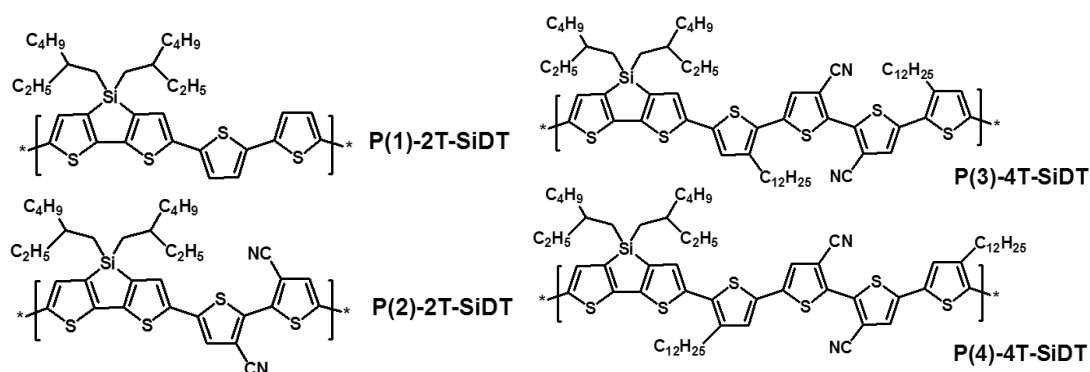


Figure 10 Chemical structures of polymers **P(1)-DT-SiDT**, **P(2)-DT-SiDT**, **P(3)-TT-SiDT**, and **P(4)-TT-SiDT**.

Solution-processed BHJ solar cells, using **P(1)-DT-SiDT**, **P(2)-DT-SiDT**, **P(3)-TT-SiDT**, and **P(4)-TT-SiDT** as electron donor materials and PC₆₁BM (or PC₇₁BM) as electron acceptor counterparts, were fabricated, optimized, and fully characterized. The optical, electrical, morphological, and photophysical properties of the corresponding thin films are reported and discussed in order to evaluate the relationship between molecular tuning, electronic structure, nanoscale morphology, kinetics of charge transfer processes and OPVs performance for this class of polymers.

Finally, PCEs up to ~ 5% and V_{oc} greater than 0.8 V have been achieved, without the need of additional processes such as thermal or solvent annealing.

2.1.1. Experimental

2.1.1.1. Materials and Methods

All reagents, PEDOT:PSS (poly(3,4-ethylenedioxythiophene): poly(4-styrenesulfonate), Clevis P VP A1 4083, H.C. Starck), PC₆₁BM and PC₇₁BM (American Dye Source), Molybdenum Oxide (MoO₃, Sigma-Aldrich), 1,8-diodooctane (Sigma-Aldrich) and various anhydrous solvents (Sigma-Aldrich) were purchased from commercial sources and used without further purification, unless otherwise noted.

The synthesis and characterization (NMR spectra, Elemental analysis, GPC analysis, electrochemical analysis) of all intermediates and polymers were done by Dr. Facchetti's group at Polyera Corporation, Skokie, Illinois, USA. Cyclic voltammetry (CV) was performed on a VC-2 Cell Stand electrochemical station equipped with BAS Epsilon software (Bioanalytical Systems, Inc., Lafayette, IN). The electrolyte solution was dry acetonitrile containing 0.1 M tetra-n-butylammonium hexafluorophosphate electrolyte. A 1.0 mm diameter platinum disk electrode, platinum wire counter electrode and Ag reference electrode were employed. Ferrocene/Ferrocinium (Fc/Fc⁺, 0.54 V vs. SCE) was used as an internal reference for all measurements. Thermogravimetric (TGA) and differential scanning calorimetry (DSC) analysis were performed simultaneously on a STA i series instrument at a ramp rate of 10°C/min under N₂ (ramp: 25 to 600°C) at atmospheric pressure in a platinum crucible.

2.1.1.2. OPV Device Fabrication and Characterization

Patterned ITO-coated glasses ($R_s \sim 10 \Omega/\text{sq}$) were cleaned in sequential sonications (for 15 min) in deionized water, acetone and isopropanol. After final sonication step, substrates were dried with a stream of N₂ gas and then placed in an oxygen plasma chamber for 10 min. Next, a thin layer (~ 30 nm) of PEDOT:PSS (Clevios P VP Al 4083) was spun-cast on the ITO surface and subsequently annealed at 150°C for 15 min. Alternatively, 5 nm of MoO₃ were deposited onto ITO substrates by thermal evaporation in a vacuum of $\sim 2 \times 10^{-6}$ Torr. Samples were then transferred inside the glove box (<0.1 ppm of O₂ and H₂O) for active layer and top contact deposition. In the meantime, the active blends were formulated inside the glove box, in various ratios (wt/wt), with a total concentration of 16 mg/mL in dry CHCl₃. The mixture solutions were sonicated at $\sim 50^\circ\text{C}$ for 1 hour and then spun-cast on top of the ITO/PEDOT:PSS surface. Before cathode deposition, the substrates were then either thermally annealed by varying the temperature and the time of the process or left as-cast. To complete the device fabrication, LiF/Al or Ca/Al cathodes (0.6 nm/100 nm or 20 nm/80 nm, respectively) were next deposited sequentially without breaking vacuum ($\sim 3 \times 10^{-6}$ Torr) using a thermal evaporator directly connected to the glove box. The I-V curves of complete OPV devices were recorded by a Keithley 236 source-measure unit under simulated AM1.5G illumination of 100 mW/cm² (Abet Technologies Sun 2000 Solar Simulator). The light intensity was determined by a calibrated silicon solar cell fitted with a KG5 color glass filter to bring spectral mismatch to unity. The active area of the solar cell was exactly 6 mm². During testing, each cell was carefully masked, by calibrated mask, to prevent an excess photocurrent generated from the parasitic device regions outside the overlapped electrode area. All solar cells were tested inside the glove box with oxygen and moisture free environment.

External Quantum Efficiency (EQE) was measured with a home built system on encapsulated devices: monochromatic light was obtained with a Xenon arc lamp from Lot-Oriel (300 Watt power) coupled with a Spectra-Pro monochromator. The

photocurrent produced by the device passed through a calibrated resistance (51 Ω) and the voltage signal was collected after the resistance with a Lock-In Digital Amplifier-SR830. Signal was pulsed by means of an optical chopper (\sim 500 Hz frequency). A calibrated Silicon photodiode was used as reference.

2.1.1.3. Hole-only Devices Fabrication and Characterization

The single-carrier diodes are based on the use of electrodes that suppress the injection of either electrons or holes, resulting in hole- or electron-only devices. The hole-only devices, used to investigate the hole transport behavior of the active layers, were fabricated following the same procedure presented above except for the top electrode, which was replaced with Au (50 nm) (glass/ITO/PEDOT:PSS/Blend/Au). The charge mobility was calculated by fitting the current density-voltage curves, recorded in dark conditions with the Mott-Gurney equation (Space Charge Limited Current, SCLC model),^[25] reported in **Equation 12**:

$$J = (9/8) \mu \epsilon_r \epsilon_0 (V^2/d^3) \quad \text{Eq. 12}$$

where J is the current density, μ is the mobility, ϵ_r is the relative permittivity of the blend, ϵ_0 is the permittivity of vacuum, d is the thickness of the active layer, and V is the voltage.

2.1.1.4. Thin-film characterization

All thin-film characterizations were performed in air. Solution and thin film optical absorption spectra were recorded on a JASCO V-550 spectrophotometer. The thickness of the various films was measured by a profilometer (KLA Tencor, P-6) on glass/ITO/PEDOT:PSS substrates. Atomic Force Microscopy (AFM) images were taken with a Solver Pro (NT-934 MDT) scanning probe microscope in tapping semi-contact mode. The AFM images were recorded directly on the tested devices.

Photoluminescence (PL) spectra were obtained by exciting the samples with the second harmonic of a femtosecond Ti:Sapphire laser at 450 nm. Time resolved measurements were performed with a monochromator coupled to a Hamamatsu streak camera (time resolution \sim 2 ps). PL spectra were recorded with an optical multichannel analyzer. All photoluminescence measurements were performed with the samples kept in vacuum (\sim 10^{-6} mbar) at room temperature. The decay times are obtained by fitting the experimental data with the bi-exponential function reported in **Equation 13**:

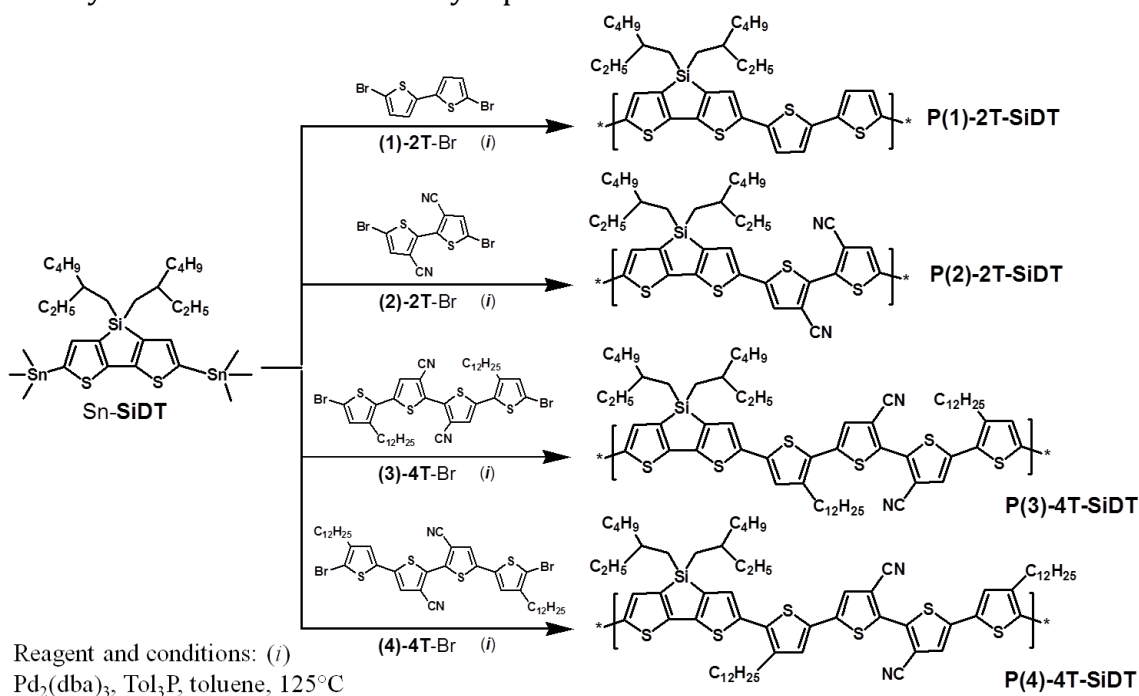
$$y = y_0 + w_1 e^{\left(-\frac{t-t_0}{t_1}\right)} + w_2 e^{\left(-\frac{t-t_0}{t_2}\right)} \quad \text{Eq. 13}$$

where t_1 and t_2 represent the components of the decay lifetime, w_1 and w_2 the corresponding pre-exponential factors (weights) and y_0 and t_0 two fitting constants.

2.1.2. Results and discussion

2.1.2.1 Polymers synthesis and thermal properties

The present P(1)-2T-SiDT, P(2)-2T-SiDT, P(3)-4T-SiDT, and P(4)-4T-SiDT copolymers (abbreviated in the text as **P(1)**, **P(2)**, **P(3)** and **P(4)**, respectively) were synthesized as schematically represented in **Scheme 5**.



Scheme 5. Schematized synthesis procedure of the **P(1)-P(4)** polymers.

The 4,4-bis(2-ethylhexyl)-2,6-bis(trimethyltin)-dithieno[3,2-*b*:2',3'-*d*]silole (Sn-SiDT) monomer and dibrominated (unsubstituted or 3,3'-dicyano)-oligothiophenes based ((1)-2T-Br, (2)-2T-Br, (3)-4T-Br, and (4)-4T-Br) comonomers, were combined and purified *via* Stille crosscoupling reaction in refluxing toluene, using tris(dibenzylideneacetone)dipalladium(0) ($\text{Pd}_2(\text{dba})_3$) and Tri(*o*-tolyl)phosphine (Tol_3P) as catalysts. The resulting polymers were precipitated in methanol, collected by filtration, washed with methanol and further purified by Soxhlet extraction to remove low molecular weight fractions. The remaining part was extracted with chloroform and the resulting polymers structures and purities have been supported by ^1H NMR spectra and elemental analysis, here not reported for brevity.

The polymers thermal properties were investigated both by TGA and DSC at a temperature ramp rate of $10^\circ\text{C}/\text{min}$ under nitrogen atmosphere. The TGA data indicate that all polymers are robust with decomposition temperatures (T_d) above

350°C (**Table 1**), defined as the temperature at 5% mass loss. Notably, no significant thermal transitions were identified in the DSC data up to ~ 320°C.

2.1.2.2. Polymers optical and electrochemical properties

The purified polymers **P(1)-P(4)** have average molecular weights (M_n), determined by high temperature GPC, ranging from 4.6 kDa to 8.6 kDa with a polydispersity index (PDI) between 1.8 and 2.3, as summarized in **Table 1**.

Table 1. Molecular weights and thermal, optical and electrochemical properties of **P(1)-P(4)**. [a] determined by GPC using polystyrene standards and 1,2,4-trichlorobenzene as eluent; [b] in CHCl_3 ; [c] spin-coated from CHCl_3 solutions on glass substrates; [d] $E_{\text{gap}}^{\circ} = 1240/\lambda_o$.

Polymer	M_n [kDa] ^[a]	M_w [kDa] ^[a]	PDI	T_d [°C]	Solution ^[b]			Thin-film ^[c]			E_{HOMO} [eV]	E_{LUMO} [eV]
					λ_{max} [nm]	λ_o [nm]	E_{gap}° [eV] ^[d]	λ_{max} [nm]	λ_o [nm]	E_{gap}° [eV] ^[d]		
P(1)	8.6	15.9	1.8	> 350	514	610	2.03	530	655	1.89	- 5.22	- 3.19
P(2)	4.6	10.8	2.3	> 380	550	685	1.81	586	717	1.73	- 5.63	- 3.82
P(3)	6.7	15.0	2.3	> 350	542	708	1.75	588	723	1.71	- 5.47	- 3.72
P(4)	6.4	12.5	2.0	> 360	529	636	1.95	599	726	1.71	- 5.52	- 3.57

Polymers **P(1)** and **P(2)** are sufficiently soluble in chlorinated solvents for device fabrication (e.g. ~10 mg/ml in chloroform), thanks to the presence of the two branched 2-ethylhexyl alkyl chains linked to the Silicon atom in the dithienosilole unit. However, increasing the length of the thiophene based comonomer, passing from **P(1)-P(2)** to **P(3)-P(4)**, additional *n*-dodecyl chains have been introduced on the 3 or 4 thiophene positions, to improve the co-polymer solubility even at room temperature.

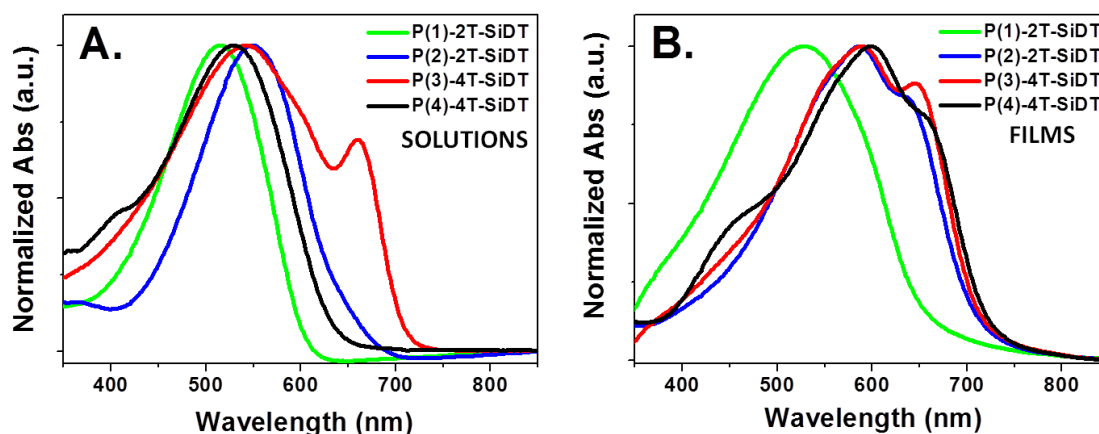


Figure 11 UV-Vis absorption spectra of pristine polymers in: (A) CHCl_3 solutions, (B) thin-films spin-coated from CHCl_3 .

The optical absorption spectra of the pristine polymers **P(1)**-**P(4)** in dilute chloroform solutions and as thin films are displayed in **Figure 11**. The detailed absorption data, including absorption maxima wavelengths (λ_{max}) in solution and film, as well as the corresponding onset (λ_0) and bandgap values (E_{gap}^0) are summarized in **Table 1**. All compounds exhibit relatively broad absorption bands, which indicates that a significant part of the solar spectral flux is absorbed, contributing to the generation of photocurrents.

The solution absorption profiles of polymers **P(1)**-**P(4)** (**Figure 9A**) exhibit a narrow variation of the λ_{max} values, ranging from 514 to 550 nm. By comparing **P(1)** and **P(2)** spectra, a 36 nm red shift between the corresponding λ_{max} values can be observed. This effect is related to the presence of the -CN groups, that simultaneously lowers both the HOMO and LUMO energy levels and enhance T2 acceptor capabilities resulting in a lower polymer bandgap (**Table 1**). However, the electronic effect of the -CN substituents seems to be attenuated by the presence of the two additional adjacent thiophene rings present in **P(3)** and **P(4)**, reducing the λ_{max} red shift of these two polymers with respect to **P(1)**. It is worth noting that, despite the isomeric structures of the **P(3)** and **P(4)** in which the only difference is the position of the alkyl chains linked to the thiophene spacers, the shape of the corresponding absorption spectra are significantly different. In particular, the broader spectrum of **P(3)** and the sharp shoulder peak at the longer wavelength region (~ 650 nm) might suggest a more favorable backbone conformation, which could be responsible of a partial pre-aggregation of the polymer backbone in solution.^[26]

The thin film spectra of **P(1)**-**P(4)** (**Figure 11B**) are significantly broadened (except **P(3)**) and red shifted relatively to the solution spectra. The resulting red shift magnitude ($\Delta\lambda_{\text{max}} = \lambda_{\text{max}}^{\text{sol}} - \lambda_{\text{max}}^{\text{film}}$) increases, proceeding from **P(1)** to **P(4)** ($\Delta\lambda_{\text{max}} = 16, 36, 46$ and 70 nm, respectively), probably due to the progressive enhancement of the interchain π - π interactions as a function of the substitution and length of the thiophene-based comonomers. Except **P(1)**, the thin film absorption spectra of the polymers **P(2)**, **P(3)** and **P(4)** show vibronic structures

around the maximum of absorption, with a more pronounced shoulder at ~ 650 nm, indicating a partial polymer chain ordering in the solid state. It should be noted that **P(3)** exhibits the most intense shoulder relatively to the main absorption peak, suggesting stronger intermolecular interactions, in agreement with the polymer behavior in solution.

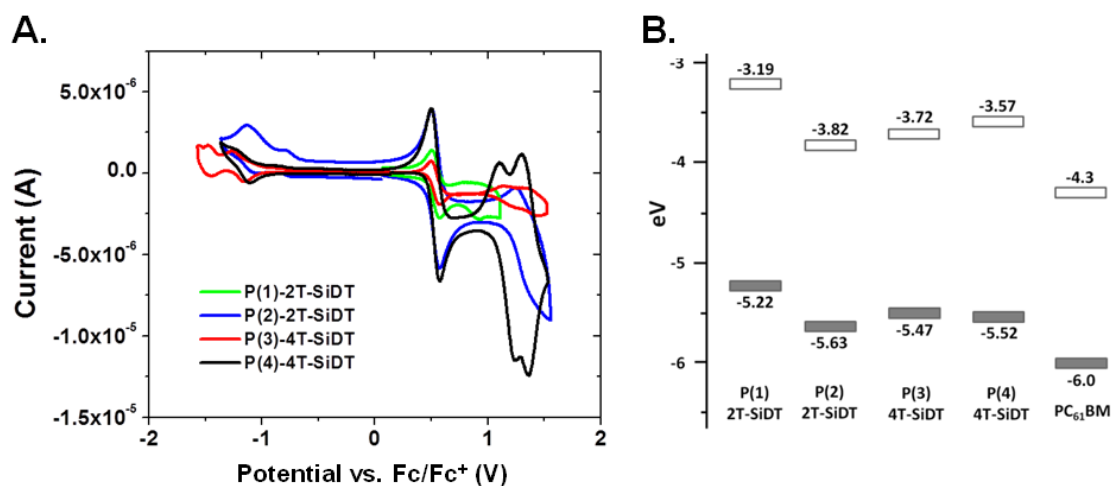


Figure 12 A. CV of **P(1)-P(4)** polymers. B. Schematic energy level diagram with HOMO and LUMO levels of **P(1)-P(4)** polymers and of PC₆₁BM.

The cyclic voltammetry (CV) curves of **P(1)-P(4)** are reported in **Figure 10a** and the polymers E_{HOMO} and E_{LUMO} values, also reported in **Table 1**, are schematically depicted in **Figure 12b**. As shown in **Figure 12a**, the electrochemical oxidation onsets (E_{ox}) of **P(1)-P(4)** are 0.78 V, 1.19 V, 1.03 V and 1.08 V, respectively. On the basis of the oxidation onsets, the HOMO energy levels of the present polymers were estimated to lie at -5.22 eV, -5.63 eV, -5.47 eV and -5.52 eV for **P(1)-P(4)**, respectively.^[27] It has to be noted that these polymers are also expected to be more resistant to oxidation in ambient conditions comparing to P3HT ($E_{\text{HOMO}} \sim -5.0$ eV).^[28]

The reduction peaks of the cyclic voltammograms were not assigned since they were not clearly visible, thus the LUMO energy levels were calculated by the equation: $E_{\text{LUMO}} = E_{\text{HOMO}} + E_{\text{gap}}^0$ (E_{gap}^0 were determined from the optical absorption spectra of pristine polymers in solution, **Table 1**). The LUMO levels for **P(1)-P(4)** were then estimated to lie at 3.19 eV, 3.82 eV, 3.72 eV and 3.57 eV, respectively, yielding E_{LUMO} offsets between the polymers and PC₇₁BM of more than 0.3 eV, which should ensure efficient exciton dissociation.^[29]

Note that the incorporation of electron-withdrawing -CN substituents on the thiophene rings effectively lowers both LUMO and HOMO energies. Indeed, comparing to **P(1)**, a ΔE_{LUMO} (difference between the LUMO energies of the two polymers) of 0.63 eV and ΔE_{HOMO} (difference between the HOMO energies of the two polymers) of 0.41 eV were observed for **P(2)**. Since the LUMO energy lowering is greater than the HOMO one, **P(2)** results to be a more stable and lower bandgap

polymer comparing to **P(1)** (with a ΔE_{gap} , calculated as the difference between the two polymers E_{gap} values, of 0.22 eV). A less marked effect can be expected for polymers **P(3)** and **P(4)**, where the introduction of two electron-rich thiophene spacers should increase the π -electron density, thus attenuating the electronic effect of the -CN groups on the macromolecular frontier orbitals energy levels. As supposed, **P(4)** exhibits, comparing to **P(1)**, a ΔE_{LUMO} of 0.38 eV, ΔE_{HOMO} of 0.30 eV and ΔE_{gap} of 0.08 eV. However, the discrepancy observed for **P(3)**, which exhibits, with respect to **P(1)**, a ΔE_{LUMO} of 0.53 eV, ΔE_{HOMO} of 0.25 eV and ΔE_{gap} of 0.28 eV, can be explained considering the additional contribution of the intermolecular π - π interactions observed in solution, which further lower the E_{gap}^0 (see **Table 1**) and thus the resulting LUMO level of **P(3)**.

The obtained HOMO and LUMO energies of **P(1)-P(4)** suggest that high open-circuit voltages (V_{OC})^[29] should be achievable when **P(1)-P(4)** are combined, for example, with PC₆₁BM in BHJ OPV devices.

2.1.2.3. Devices optimization and characterization

The potential of polymers **P(1)-P(4)** as donor materials in OPV devices was investigated in BHJ solar cells using PC₆₁BM or PC₇₁BM as acceptor counterparts. The device structure employed was the standard glass/ITO/PEDOT:PSS/Active Layer/LiF/Al. The active blend was spin-coated from dry chloroform solutions (chloroform was found to be the optimum solvent) and the most efficient OPV devices were obtained without additional thermal treatments.

Table 2. OPV characteristics of the most representative polymer:PC_{xx}BM based BHJ solar cells. [a] Additive: 2% (v/v) of 1,8-diiodooctane; [b] 5 nm of MoO₃ as anode buffer layer; [c] Alternative cathode: Ca (20 nm)/ Al (80 nm).

Polymer : PC_{xx}BM ratio (wt/wt)	V_{oc} [mV]	J_{sc} [mA/cm²]	FF [%]	PCE [%]
P(1) : PC ₆₁ BM (1.5:1)	451	1.30	31	0.18
P(1) : PC ₆₁ BM (1:1)	671	2.22	43	0.64
P(1) : PC ₆₁ BM (1:1.5)	360	3.44	36	0.45
P(1) : PC ₇₁ BM (1:1)	426	3.18	45	0.61
P(2) : PC ₆₁ BM (1.5:1)	542	1.59	30	0.26
P(2) : PC ₆₁ BM (1:1)	627	1.94	39	0.47
P(2) : PC ₆₁ BM (1:1.5)	461	2.04	38	0.36
P(2) : PC ₇₁ BM (1:1)	712	1.12	32	0.25
P(3) : PC ₆₁ BM (1.5:1)	854	6.67	51	2.90
P(3) : PC ₆₁ BM (1:1)	872	7.05	57	3.49
P(3) : PC ₆₁ BM (1:1.5)	875	6.59	52	3.02
P(3) : PC ₇₁ BM (1:1)	905	4.52	55	2.25
P(3) : PC ₇₁ BM (1:1) ^[a]	838	8.05	59	4.00

P(3) : PC ₇₁ BM (1:1) ^[a,b]	820	8.57	62	4.32
P(3) : PC ₇₁ BM (1:1) ^[a,b,c]	830	8.78	62	4.52
P(4) : PC ₆₁ BM (1.5:1)	880	5.25	42	1.96
P(4) : PC ₆₁ BM (1:1)	775	7.70	46	2.78
P(4) : PC ₆₁ BM (1:1.5)	907	4.38	54	2.15
P(4) : PC ₇₁ BM (1:1)	908	3.97	49	1.77
P(4) : PC ₇₁ BM (1:1) ^[a]	831	7.73	57	3.70
P(4) : PC ₇₁ BM (1:1) ^[a,b]	820	8.60	61	4.30
P(4) : PC ₇₁ BM (1:1) ^[a,b,c]	850	9.25	63	4.90

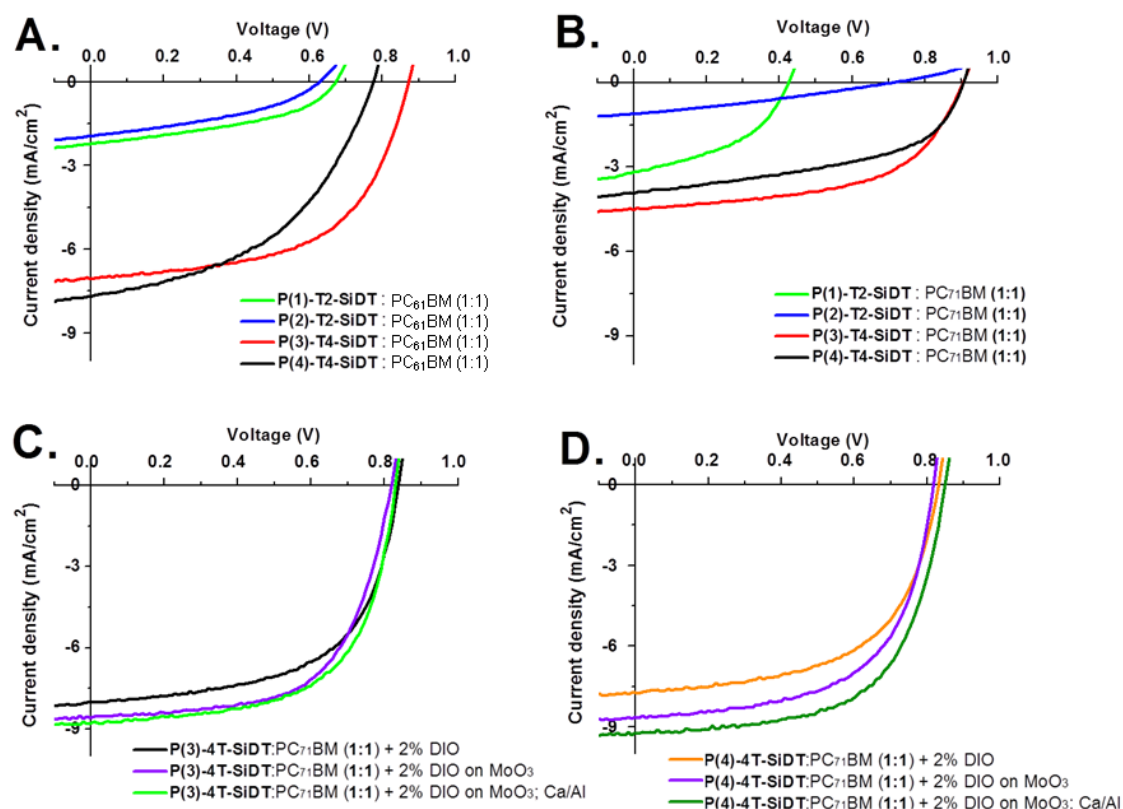


Figure 13 J-V plots, under illumination, of optimized as-cast BHJ solar cells based on: (A) 1:1 (wt/wt) **P(1)-P(4)**:PC₆₁BM films; (B) 1:1 (wt/wt) **P(1)-P(4)**:PC₇₁BM films; (C and D) 1:1 (wt/wt) **P(3)**:PC₇₁BM and **P(4)**:PC₇₁BM films using progressively: *i*) 2% (v/v) of DIO, *ii*) MoO₃ as anode interfacial layer, and *iii*) Ca /Al as cathode.

Table 2 summarizes the photovoltaic parameters, while current density-voltage (J-V) plots under standard illumination for the solar cells based on **P(1)-P(4)**:PC₆₁BM (or PC₇₁BM) active blends are shown in **Figure 13**.

A first optimization of the **P(1)-P(4)** based BHJ solar cells was carried out by using PC₆₁BM as acceptor material. The optimal D:A ratio was found to be 1:1 (wt/wt) for all polymers. Upon increasing (1.5:1) or decreasing (1:1.5) the donor content in the active blend a significant drop in J_{SC} , V_{OC} and FF was observed, resulting in lower PCEs.

By comparing the performances of optimized OPV devices based on 1:1 (wt/wt) **P(1)-P(4):PC₆₁BM** films (**Figure 13A** and **Table 2**) the main difference is represented by J_{SC} , which reflects the gap in the overall PCEs. Indeed, the less efficient solar cells based on **P(1)** and **P(2)** yield current densities of ~ 2 mA/cm² with maximum PCEs of 0.64 % and 0.46 %, respectively, while the solar cells based on **P(3)** and **P(4)** afford J_{SC} of ~ 7 mA/cm² with PCEs of 3.49 % and 2.78 %, respectively.

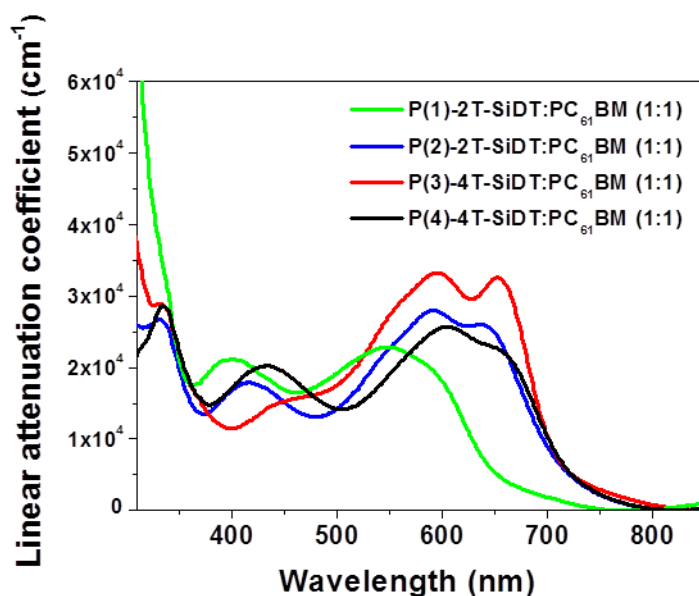


Figure 14 Linear attenuation coefficient spectra of the **P(1)-P(4):PC₆₁BM** active layers.

The light harvesting properties of the **P(1)-P(4):PC₆₁BM** active layers can be estimated by their linear absorption coefficient spectra, which are reported in **Figure 14**. Since only slight differences, except for **P(1)**, in terms of linear absorption coefficients were found for the **P(2)-P(4):PC₆₁BM** films and since the thickness of the films is almost constant (~ 100 nm), the higher J_{SC} values observed for **P(3)-P(4):PC₆₁BM** based devices comparing to **P(1)-P(2):PC₆₁BM** based ones, can be mainly ascribed to the variations in terms of morphological, photophysical and charge transport properties of the blends.

To better understand the charge transport properties of the polymers, the dark I-V curves of hole-only devices, prepared as reported in the experimental section and consisting in a stack of glass/ITO/PEDOT:PSS/polymer/Au, were measured, allowing to evaluate the hole mobility (μ_h) of pristine polymer films by the SCLC method.^[30] As expected, μ_h was found to be one order of magnitude higher for **P(3)** and **P(4)** ($4 \cdot 10^{-4}$ cm² V⁻¹ s⁻¹ and $6 \cdot 10^{-4}$ cm² V⁻¹ s⁻¹, respectively) with respect to **P(1)** and **P(2)** ($\sim 10^{-5}$ cm² V⁻¹ s⁻¹ for both polymers). It has to be noted that the charge mobilities calculated for **P(3)** and **P(4)** are in agreement with those of other highly efficient donor polymers.^[31]

For each polymer:PC₆₁BM based solar cell the average value of V_{OC} (V_{OC}^{av}), estimated from the open circuit voltages observed at different D:A wt/wt ratios (**Table 2**), track the progression:

$$V_{OC}^{av} \mathbf{P(1)} < V_{OC}^{av} \mathbf{P(2)} < V_{OC}^{av} \mathbf{P(3)} \approx V_{OC}^{av} \mathbf{P(4)}$$

rather than:

$$V_{OC}^{av} \mathbf{P(1)} < V_{OC}^{av} \mathbf{P(3)} \approx V_{OC}^{av} \mathbf{P(4)} < V_{OC}^{av} \mathbf{P(2)}$$

which was expected from $E_{LUMO}^A - E_{HOMO}^D$ theoretical considerations^[29] (**Table 1**). The low V_{OC}^{av} of **P(2)**, despite its low lying HOMO level, could be ascribed to its poor film-forming properties, as confirmed by AFM images (see below), likely leading to poor exciton stabilization and dissociation, and low D:A phase segregation, all factors that are known to influence the V_{OC} .^[32] **P(3)** and **P(4)** based solar cells, in agreement with the $E_{LUMO}^A - E_{HOMO}^D$ offset and in combination with good film forming properties, show relatively high V_{OC}^{av} (up to ~ 850 mV).

Several efforts to optimize the thin-film nanomorphology of 1:1 (wt/wt) **P(1)-P(4):PC₆₁BM** solar cells were carried out, for instance by using different solvents (*e.g.* chlorobenzene or *o*-dicholobenzene) and thermal annealing (in the range 80-140°C and for different times), but no significant improvements were achieved. Therefore, alternative approaches to enhance the OPV performance of the **P(1)-P(4)** based polymer solar cells, with particular attention for the most efficient donors **P(3)** and **P(4)**, have been employed in order to improve the device light harvesting, nanoscale self-organization of the active BHJ layer and related charge transport/extraction processes. To this end, we used respectively: *i*) PC₇₁BM as acceptor material, *ii*) 1,8-diodooctane (DIO) as processing solvent additive, *iii*) Molybdenum oxide (MoO₃) and Calcium (Ca) as alternative anode and cathode interfacial layers.

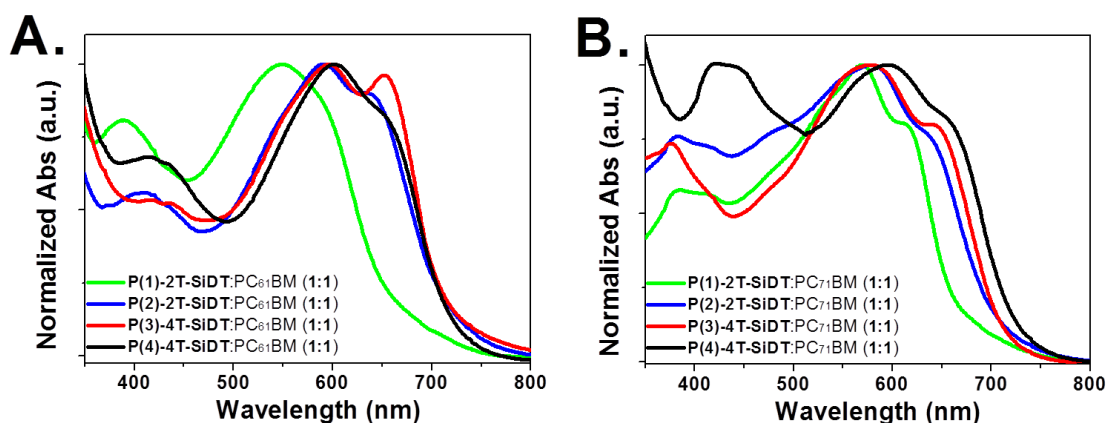


Figure 15 UV-Vis absorption spectra of: **A)** as-cast 1:1 (wt/wt) **P(1)-P(4):PC₆₁BM** films spin-coated from CHCl₃ solutions, **B)** as-cast 1:1 (wt/wt) **P(1)-P(4):PC₇₁BM** films spin-coated from CHCl₃ solutions.

P(1)-P(4):PC₇₁BM films, deposited from chloroform solution by using the best performing blend ratio found for PC₆₁BM, were then prepared in order to enhance the blend film absorption in the spectral range between 350 and 550 nm, as shown

in **Figure 15A and B**.^[33] The resulting OPV performance have been reported in **Table 2**. Despite the improved overall light harvesting of the composite blends, the resulting BHJ OPV devices exhibit lower PCEs comparing to the analogous PC₇₁BM based ones.

This result may reflect suboptimal film morphologies as observed by AFM investigation (see next section), likely due to a poorer miscibility of PC₇₁BM poor with the polymers,^[34] thus limiting the D:A phase-segregation, charge generation and transport within the active blends, in agreement with the observed low photocurrents.

The incorporation of solvent additives, such as 1,8-diiodooctane (DIO), to the blend solutions is a widely used method to promote an optimal self-organization of the BHJ components in order to improve the corresponding OPV characteristics.^[35] Indeed, it was found that the addition of 2% (v/v) of DIO to **P(3)-P(4):PC₇₁BM** blend solutions led to improved film morphologies, as will be discussed later with the morphological analysis, and greatly enhanced PCE. **P(3)** based BHJ OPVs shows indeed V_{oc} , J_{sc} , FF and PCE of 838 mV, 8.05 mA/cm², 59 % and 4.00 %, respectively. Similarly, **P(4)** based solar cells yields a PCE of 3.70% with V_{oc} , J_{sc} , and FF of 831 mV, 7.73 mA/cm² and 57%, respectively. For both polymers, the mayor improvement has to be ascribed to the almost doubled J_{sc} , indicative of well-ordered nanoscale morphology of the active layer, which correlate well with the simultaneous increase of FF and charge mobilities.

Indeed, the hole mobilities (μ_h) (estimated by SCLC model) of optimized (1:1 wt/wt) **P(3)-P(4):PC₇₁BM** films processed with DIO (2% v/v) were found to be $1.1 \cdot 10^{-4} \text{ cm}^2 \text{ V}^{-1} \text{ s}^{-1}$ and $2.0 \cdot 10^{-4} \text{ cm}^2 \text{ V}^{-1} \text{ s}^{-1}$, respectively, very similar to those measured for the pristine polymers. In comparison, the μ_h of (1:1 wt/wt) **P(3)-P(4):PC₇₁BM** based devices processed without DIO were found to be $7.2 \cdot 10^{-5} \text{ cm}^2 \text{ V}^{-1} \text{ s}^{-1}$ and $8.1 \cdot 10^{-5} \text{ cm}^2 \text{ V}^{-1} \text{ s}^{-1}$, respectively, in agreement with above mentioned film morphological features.

Further improvements in terms of PCE, up to $\sim 5\%$, for (1:1 wt/wt) **P(3)-P(4):PC₇₁BM** based solar cells were obtained by replacing conventional anode and cathode interfacial layers (PEDOT:PSS and LiF) with thin films of Molybdenum oxide (MoO₃, 5 nm) and Calcium (Ca, 20 nm), respectively. The introduction of MoO₃ (5 nm) mainly determines an increase of the FF and J_{sc} values. Enhanced FF, passing from 59 % to 62 % and from 57 % to 61% for **P(3)** and **P(4)** based devices, respectively, could be ascribed to the quasi-ohmic contact between the HOMO level of the polymer and the conduction band-edge of MoO₃ ($\sim 5.4 \text{ eV}$),^[36] that favors the hole extraction process and reduces the contact resistance.^[37] Moreover, MoO₃ interlayer seems also to promote a more favorable redistribution of the light intensity within the active layer, as a result of the refractive index matching between MoO₃ and active blend^[36], in agreement with the enhanced J_{sc} measured for **P(3)** and **P(4)** based cells (from 8.02 to 8.57 mA/cm², and from 7.73 to 8.60 mA/cm², respectively).

Additionally, the use of Ca/Al as cathode generates higher V_{oc} and J_{sc} values as a result of its lower work function, compared to LiF/Al, which primarily increases

the built-in electric field of the cell, also responsible for optimal charge extraction and collection processes.^[38] As a result, the most efficient **P(3)** based solar cell exhibits $V_{OC} = 830$ mV, $J_{SC} = 8.78$ mA/cm², and $FF = 62$ %, with $PCE = 4.52$ %. Similarly, the **P(4)** based solar cell shows $V_{OC} = 850$ mV, $J_{SC} = 9.25$ mA/cm², and $FF = 63$ %, with $PCE = 4.90$ %.

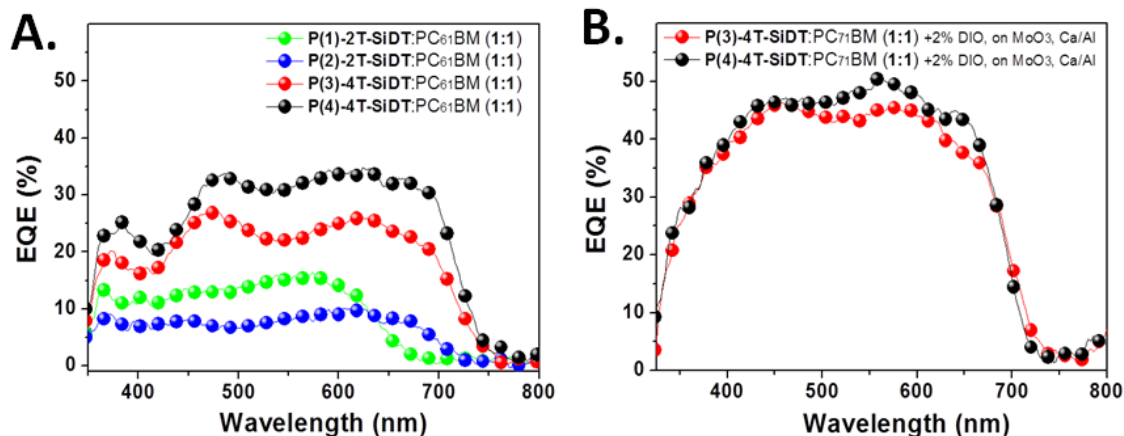


Figure 16 EQE plots of optimized as-cast BHJ solar cells based on: (A) 1:1 (wt/wt) **P(1)-P(4):PC₆₁BM** films; (B) 1:1 (wt/wt) **P(3)-P(4):PC₇₁BM** (1:1) films using 2% (v/v) of DIO, MoO₃ as anode interfacial layer, and *iii*) Ca /Al as cathode.

A deeper understanding of the different photocurrent generation efficiencies can be given by the study of the spectral responses of the devices. **Figure 16A** and **B** shows the external quantum efficiency (EQE) spectra of best devices based on 1:1 (wt/wt) **P(1)-P(4):PC₆₁BM** and **P(3)-P(4):PC₇₁BM** films. The EQE plots are consistent with the broad optical absorption spectra of the active blends (**Figure 15A** and **B**). EQE spectra of 1:1 (wt/wt) **P(1)-P(4):PC₆₁BM** (**Figure 16B**) exhibit the highest generated-electrons over incident-photons ratio, comprised within 10 % and 35 %, in the spectral range between 450 and 600 nm, corresponding to the lower energy absorption band of the polymers.

Figure 16B shows the EQE responses of the most efficient **P(3)-P(4):PC₇₁BM** based devices, in which the profiles are greatly enhanced in the whole wavelength range (350-700 nm) with maxima of 46% and 51% (at ~ 560 nm), respectively for **P(3)** and **P(4)** based solar cells, as expected from the high photocurrents measured for these devices. Convolution of these EQE spectra with the AM1.5 solar spectrum gave calculated short circuit current densities in good agreement, within the ~ 5% experimental error, with those obtained from J-V measurements.

Finally, because of the relatively large bandgap (~1.7 eV) of **P(3)** and **P(4)** the photocurrent is generated in the spectral range below 700 nm, as shown in the EQE spectra. Therefore, it is worth noting that this class of polymers can be also suitable for a bottom cell in a solution-processable tandem solar cell.

2.1.2.4. Morphological analysis

After analyzing the optical and electrical properties of the **P(1)-P(4):PC_{xx}BM** active layers, morphological analysis were performed (by tapping-mode AFM) in order to gain a deeper understanding on how the molecular structure of polymers **P(1)-P(4)** affects the solar cell output parameters.

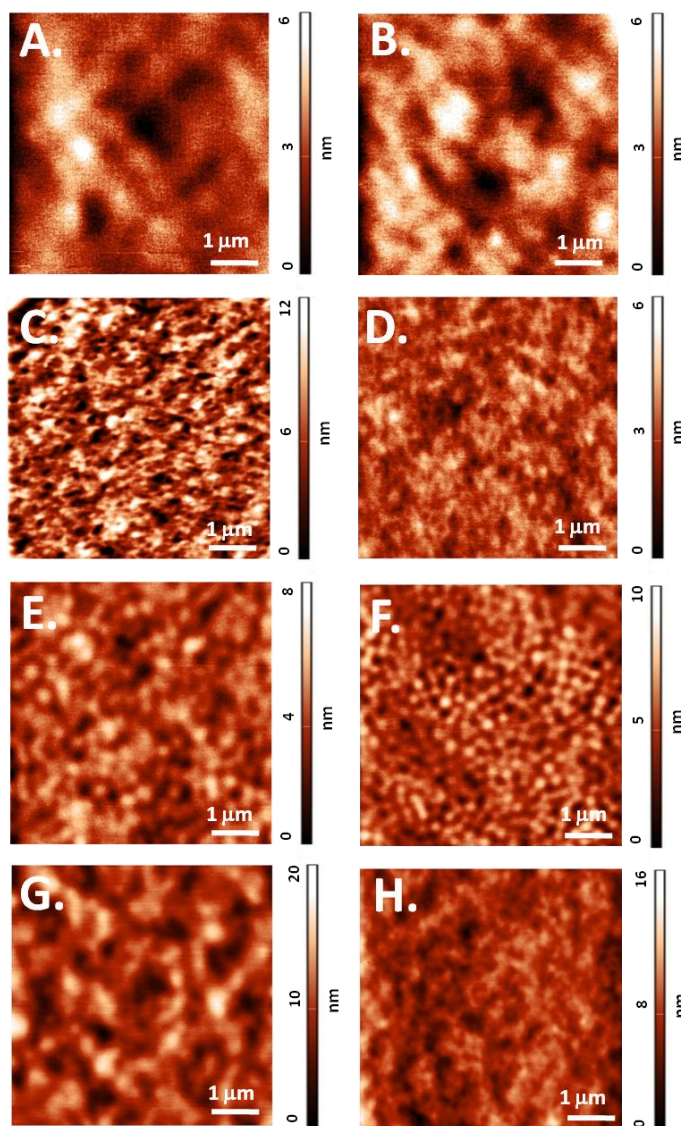


Figure 17 Tapping mode AFM images (size: 5 μm x 5 μm) of optimized as-cast 1:1 (wt/wt) **P(1)-P(4):PC_{xx}BM**: (A) **P(1):PC₆₁BM** (RMS = 0.7 nm); (B) **P(2):PC₆₁BM** (RMS = 0.8 nm); (C) **P(3):PC₆₁BM** (RMS = 1.9 nm); (D) **P(4):PC₆₁BM** (RMS = 1.0 nm); (E) **P(3):PC₇₁BM** (RMS = 1.2 nm); (F) **P(4):PC₇₁BM** (RMS = 1.2 nm); (G) **P(3):PC₇₁BM** processed with 2% (v/v) of DIO (RMS = 3.8 nm); (H) **P(4):PC₇₁BM** processed with 2% (v/v) of DIO (RMS = 2.7 nm).

Figure 17 shows topographic images of representative as-cast 1:1 (wt/wt) **P(1)-P(4):PC₆₁BM** (or **PC₇₁BM**) films processed with and without additive.

The topographic images of optimized as-cast **P(1):PC₆₁BM** and **P(2):PC₆₁BM** based films (**Figure 17A** and **17B**) exhibit a smooth and almost featureless

surfaces, with very low roughness of 0.7 and 0.8 nm (calculated as Root mean square, or RMS, deviation) which might suggest a low ordering, self-organization and phase-segregation of the BHJ components. As a result, poorly formed percolation pathways could be expected leading to limited charge transport and/or collection processes within the active blends, as confirmed by the low J_{SC} , FF and PCE obtained from the corresponding BHJ OPVs. On the other hand, the surface morphology of **P(3)-P(4):PC₆₁BM** films is significantly different from those observed for **P(1)-P(2):PC₆₁BM** blends. As shown in **Figure 17C** and **D**, for both **P(3)** and **P(4)** based blends, the roughness of the films is improved to 1.9 and 1 nm respectively, with domains sizes drastically reduced and with the formation of more defined and much finer nanostructures. These blend film topological features are likely due to an enhanced polymer aggregation and blend phase-segregation, leading to the registered higher OPV responses of the resulting **P(3)-P(4)** based solar cells.

To better understand the evolution of OPV device performance of the most efficient **P(3)-P(4)** polymers, the surface morphology of the polymer:PC₇₁BM films, produced with and without additive (DIO, 2% v/v), was also investigated. For the 1:1 (wt/wt) **P(3)-P(4):PC₇₁BM** films processed without DIO, the AFM topographic images reveal the formation of small and regular unconnected grains or circular islands (**Figure 17E** and **F**). As a consequence of the miscibility gap between the polymers and PC₇₁BM in organic solvents, the formation of island-like PC₇₁BM clusters in polymer:PC₇₁BM blends is often observed and has been found to be detrimental to solar cell performance.^[39,34a] Indeed, this kind of morphology is expected to result in inefficient exciton separation and lack of the bicontinuous interpenetrating pathways necessary for charge transport, in agreement with the relatively low hole mobilities and OPV performance of **P(3)-P(4):PC₇₁BM** based devices (**Table 1**). On the other hand, the use of processing solvent additives such as DIO is known to improve the morphology of the active layer by generating much finer nanostructures, removing grain boundaries and promoting an optimal D:A intermixing.^[35] As a result, the **P(3)-P(4):PC₇₁BM** based solutions processed with 2% (v/v) DIO generate films with more continuous and well-organized domains, as shown by AFM images (**Figure 17G** and **H**). The improved morphologies and the relatively high charge mobilities measured on these films, confirm the formation of optimal nanoscale phase separations and interpenetrating networks in the entire photoactive layer, in perfect agreement with the more than doubled photocurrents and PCEs up to ~ 5% of the devices fabricated/processed under these conditions.

2.1.2.5. Photo-luminescence (PL) quenching studies

Photoluminescence (PL) and time resolved photoluminescence (TRPL) are experimental techniques that can provide information about the efficiency and kinetics of the charge-transfer processes occurring within the D:A blend. PL spectra and lifetimes of pristine **P(1)-P(4)** films spin-coated on glass/PEDOT:PSS

were used as reference and compared with those of the corresponding 1:1 (wt/wt) D:A blends.

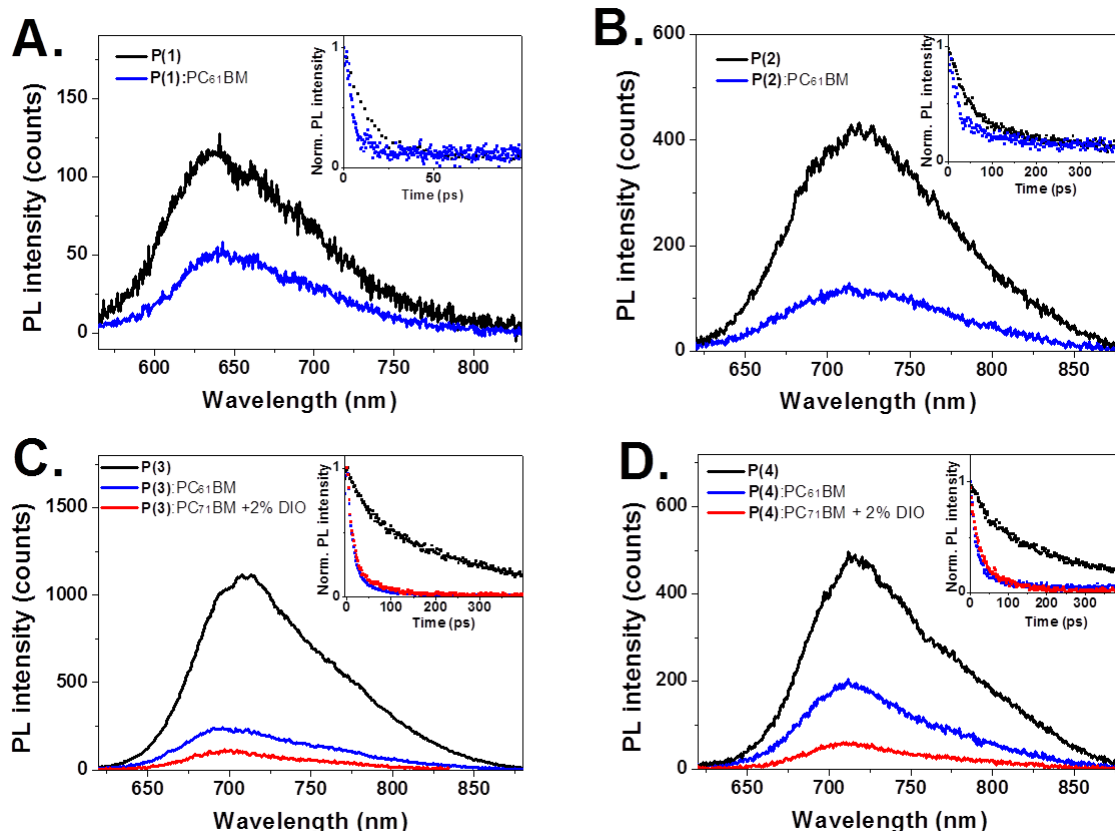


Figure 18 PL spectra of pristine polymer and blend films, spin-coated from CHCl₃ on glass, of: (A) **P(1)** and 1:1 (wt/wt) **P(1):PC₆₁BM**; (B) **P(2)** and 1:1 (wt/wt) **P(2):PC₆₁BM**; (C) **P(3)**, 1:1 (wt/wt) **P(3):PC₆₁BM** and 1:1 (wt/wt) **P(3):PC₇₁BM** processed with 2% (v/v) of DIO; (D) **P(4)**, 1:1 (wt/wt) **P(4):PC₆₁BM** and **P(4):PC₇₁BM** processed with 2% (v/v) of DIO. Laser excitation: $\lambda_{\text{max}} = 450$ nm. **Insets:** unquenched PL decays of pristine polymer films and quenched PL decays of blend films. Decays are all measured at the λ maximum of emission of the irradiated film.

PL experiments were performed by exciting the samples with a pulsed laser at 450 nm. Intense PL spectra with structureless bands centered at 636, 719, 712 and 716 nm were registered for pristine **P(1)**, **P(2)**, **P(3)** and **P(4)** films, respectively (**Figure 18**). The Stokes shift between the absorption and emission maxima of **P(1)-P(4)** films (<130 nm, a value comparable to that of other polymers, for example ~100 nm for MDMO-PPV),^[40] allows the attribution of the registered PL band to the emission from the first singlet excited state to the ground state, transition with a relatively small conformational relaxation.

Table 3. TRPL lifetimes and PL quenching ratios measured for **P(1)-P(4)** based films. [a] films spin-coated on PEDOT:PSS from CHCl₃ solutions.

Film ^[a]	PL lifetime (t_{1^p}, t_{2^p}) [ps] ^[b] Weights (W_{1^p}, W_{2^p}) [%]	Quenching Ratio [Q]
P(1)	$t_{1^p} = 59 \pm 15$ (6 %), $t_{2^p} = 12 \pm 1$ (94 %)	--
P(2)	$t_{1^p} = 304 \pm 9$ (29 %), $t_{2^p} = 44 \pm 2$ (71 %)	--
P(3)	$t_{1^p} = 374 \pm 3$ (68 %), $t_{2^p} = 42 \pm 3$ (32 %)	--
P(4)	$t_{1^p} = 324 \pm 8$ (63 %), $t_{2^p} = 39 \pm 3$ (37 %)	--
P(1) : PC ₆₁ BM	$t^b = 5.4 \pm 0.2$ (100 %)	0.67
P(2) : PC ₆₁ BM	$t_{1^b} = 183 \pm 31$ (17 %), $t_{2^b} = 20 \pm 1$ (83 %)	0.84
P(3) : PC ₆₁ BM	$t_{1^b} = 67 \pm 3$ (7 %), $t_{2^b} = 13 \pm 1$ (93 %)	0.94
P(4) : PC ₆₁ BM	$t_{1^b} = 75 \pm 1$ (15 %), $t_{2^b} = 17 \pm 1$ (85 %)	0.92
P(3) : PC ₇₁ BM + 2% DIO	$t_{1^b} = 92 \pm 7$ (11 %), $t_{2^b} = 16 \pm 1$ (89 %)	0.91
P(4) : PC ₇₁ BM + 2% DIO	$t_{1^b} = 74 \pm 5$ (29 %), $t_{2^b} = 18 \pm 1$ (71%)	0.84

For these emissions, biexponential decays were registered in the TRPL experiments, and the corresponding fitting parameters and decay lifetimes are reported in **Table 3**. It is worth noting that the introduction of the -CN group on the polymer backbone, passing from **P(1)** to **P(2)**, increases the fluorescence lifetimes by ~ 5 times. This effect, accompanied by the already discussed tuning of the HOMO and LUMO energy levels, spectral bathochromic shift and a probable, but not measured, increase in PL quantum yield, has been also reported in other cyano-substituted conjugated polymers.^[41]

Also the introduction of two additional thiophene rings in the copolymer backbone of **P(3)** and **P(4)** significantly influences the PL lifetime. In particular, passing from **P(2)** to **P(3)-P(4)**, independently from the position of the alkyl chains, the longer component of the PL decay (at ~ 300 -350 ps) becomes predominant in the biexponential fitting expression. Since for some polymers longer PL decay lifetimes are attributed to higher crystallinity^[42], an overall enhanced crystalline phase of **P(3)** and **P(4)** films comparing to **P(1)** and **P(2)** can be expected. This would be in agreement with the higher charge transport properties and the increased nanostructuration of the surface morphology of the corresponding active blends, observed by AFM, passing from **P(1)-P(2)** to **P(3)-P(4)** based films.

For the polymer:fullerene blends in which PC₆₁BM was used as acceptor, most of the light is absorbed by the polymer and the contribution of PC₆₁BM to absorption is negligible. Since also the emission quantum yield of fullerene derivatives is usually much lower (<10⁻³) than the emission of highly conjugated polymers^[43], the PL spectra and lifetimes measured for **P(1)-P(4)**:PC₆₁BM blend films has to be mainly ascribed to the polymer quenched emission. Indeed, the occurrence of effective charge-transfer from the polymers to PC₆₁BM is confirmed by the observed quenching of the PL emission when going from pure **P(1)-P(4)** to **P(1)-P(4)**:PC₆₁BM films (**Figure 18**), accompanied by the strong decrease of the PL lifetimes, where the shorter component of the biexponential decay (5 ps for **P(1)** and ~ 20 ps for **P(2)-P(4)**) becomes predominant (**Table 3** and insets **Figure 18**).^[44] The PL quenching ratios Q can be calculated for each polymer through the PL decays lifetimes, following **Equation 14**:

$$Q = 1 - \frac{\sum_{j=0}^n w_j^b t_j^b}{\sum_{i=0}^n w_i^p t_i^p} \quad \text{Eq. 14}$$

where t_i^p and t_j^b are the i^{th} and j^{th} components of the lifetime found by fitting the PL decay of the polymer alone and the D:A blend films respectively, and w_i^p and w_j^b are their relative weights in the fitting expression.^[45] Therefore, the so obtained Q counts for all the deactivation processes for the polymer excited state due to the presence of PC₆₁BM, including charge transfer, that is assumed to be the main deactivation pathway. An increase in Q is found going from **P(1)**:PC₆₁BM to **P(2)**:PC₆₁BM. This could be ascribed to the lengthening of the **P(2)** PL lifetime, as a result of the previously mentioned electronic effect of the -CN groups on the polymer electronic states. In fact, since **P(2)** has a longer lived excited state comparing to **P(1)**, the probability that its polaron diffuses at the D:A interface and gives an electron-transfer reaction with fullerene, rather than a radiative decay, increases comparing to **P(1)**.

A further increase in Q passing from **P(2)**:PC₆₁BM to **P(3)-P(4)**:PC₆₁BM is observed, accordingly to the corresponding increased J_{SC} . This can be due to the presence of two additional thiophene rings in the polymer repeating unit that might promote the intermolecular electronic coupling between the polymer chains and/or between polymer and fullerene, the latter leading to increased quenching ratio, indicative of a more efficient charge-separation process. Indeed, a much finer and defined blend film nanostructuration, likely due to enhanced polymer aggregation and D:A phase segregation, was observed in the AFM topographic images of **P(3)-P(4)**:PC₆₁BM films comparing to **P(1)-P(2)**:PC₆₁BM.

For the PL and TRPL study on **P(1)-P(4)**:PC₇₁BM blend films, additional considerations have to be taken into account. Differently from PC₆₁BM, the C₇₀-based acceptor exhibits a significant visible light absorption.^[46] Therefore charge generation by photo-excitation of the polymer:PC₇₁BM based films could arise, other than from the polymer excitons, also from the fullerene excitons, either by direct hole transfer from the fullerene to the polymer, or by exciton energy

transfer from the fullerene to the polymer, followed by the conventional electron transfer from the polymer exciton to the fullerene.^[47] Since at 450 nm the **P(1)-P(4)** polymers and the PC₇₁BM exhibits comparable extinction coefficients and the PC₇₁BM emission lies in the same spectral region (~720 nm)^[44] as the **P(2)-P(4)** pristine polymers, the quenched PL registered for the **P(2)-P(4):PC₇₁BM** blend films could be attributed both to the polymer or fullerene, and a univocal interpretation of the relative quenching processes results more complicated than for the **P(1)-P(4):PC₆₁BM** blends. In any case, the PL quenching experiments performed on optimized **P(3)** and **P(4)** blends with PC₇₁BM as acceptor and DIO (3%, v/v) as additive, showed a further decrease in the PL intensities comparing to **P(3)-P(4):PC₆₁BM** films (**Figure 18C** and **18D**). This indicates that equally efficient (or better) charge separation occurs between the best performing polymers, **P(3)** and **P(4)**, and the acceptors, PC₆₁BM and PC₇₁BM, for those films where morphology is optimal for the device performances. In fact, very similar PL decays were measured for the **P(3)-P(4):PC₆₁BM**-based blends and the **P(3)-P(4):PC₇₁BM** (with 3% DIO) based ones in the TRPL experiments (**Table 3**). Moreover, this might indicate that the use of DIO does not have a strong influence on the charge separation process kinetics, but it might rather affect the polymeric phase morphology such as domain sizes, crystallinity and spatial arrangement. The additive-induced morphology of **P(3)-P(4):PC₇₁BM** blends also corresponded, as expected, to the most efficient **P(3)** and **P(4)** based devices.^[48]

2.1.3. Conclusions

A new series of silole-based polymers have been designed, synthesized and characterized. Rational and sequential structural modifications on the thiophene-based spacers allowed the evaluation of the polymer chemical structures on the main properties of this interesting class of donor materials. It was found that the incorporation of -CN substituents and the presence of two additional alkylthiophene moieties (**P(3)** and **P(4)**) in the polymer backbone significantly influence the optical, electronic, morphological, photophysical, charge transport and subsequently the performance of the resulting devices.

As expected, the presence of the -CN substituents in the backbone of **P(2)** lowers the bandgap and the LUMO energy of the polymer enhancing its optical and photophysical properties, comparing to the unsubstituted polymer **P(1)**. Moreover, the presence of the longer alkylthiophene moieties in **P(3)** and **P(4)** significantly increases the polymer solubility, electrical properties (light absorption and hole mobility) and improves the nano-structuring and opto-electrical properties of the corresponding blend films, comparing to **P(1)** and **P(2)**. As a result, while the PCEs of **P(1)-P(2)** based OPV devices are lower than 1%, the optimized **P(3)-P(4)** based cells exhibit PCEs approaching 5%. In particular, the BHJ solar cell based on **P(4):PC₇₁BM** film showed a PCE of 5% with V_{oc} , J_{sc} and FF of 850 mV, 9.25 mA/cm² and 63 %, respectively.

The obtained results combined with a relatively simple synthetic procedures, make this series of polymers a promising benchmark for further developments of new efficient semiconducting donor polymers for applications in BHJ OPVs. Indeed, the device performance could be further improved by the optimization of the photoactive materials taking advantages from the findings and basic considerations reported and discussed in this study.

2.2. A new push-pull polymer with unsaturated spacer

2.2.1. Introduction

Within the strategies used to lower the bandgap of donor polymers for BHJ OPV application is the afore mentioned push-pull approach, where π electron-rich and π electron-poor fragments are alternated along the π -conjugated backbone.^[49] This section focuses on a new push-pull polymer where 4,8-dialkoxy-benzo[1,2-*b*:4,5-*b'*]dithiophene (BDT) and 2,1,3-benzothiadiazole (BTD) (**Figure 19**) are alternated as π electron-rich and π electron-poor groups, being separated by a vinyl-spacer to form a new polymeric structure.

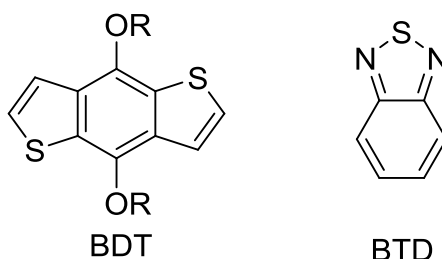


Figure 19 Structure of donor BDT and acceptor BTD constituting units of the of the investigated D-A polymers.

The donor BDT group has been recently used in a significant number of highly efficient polymers for BHJ devices,^[50] including some of the present record polymers with overall conversion efficiencies approaching 8%.^[51] The acceptor BTD ring has lately received great attention thanks to its electron-withdrawing strength and ability to effectively lower the LUMO energy.^[52] Again, the use of BTD allowed to build a new polymer with top-ranked PCE (6.1%) and a remarkable internal quantum efficiency approaching unity.^[53]

Furthermore, the use of the donor BDT and/or acceptor BTD led to polymers with optimal HOMO, LUMO, and bandgap energies, closely matching those of ideal conjugated polymers for OPV devices, showing that these polycyclic heteroaromatic rings are very effective constituting units for the design of well performing π -conjugated polymers for BHJ cells. Nevertheless, very few reports have described the simultaneous use of both fragments in the same polymeric backbone.^[54] In these studies, an aryl-aryl bonding was always present to link the

BDT and BTB groups either directly to each other or alternated with thienyl spacers.

The most simple combination, the polymer **P(BDT-BTD)**, was investigated by Hou, Yang and co-workers (**Figure 20**).^[54a] An electrochemical bandgap of 1.9 eV and a PCE of 0.90% in combination with PC₆₁BM were reported.

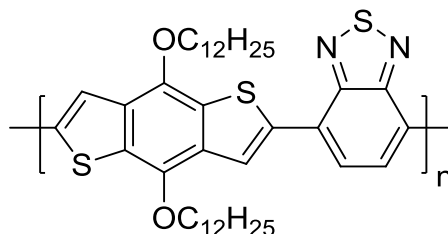


Figure 20 Structure of polymer **P(BDT-BTD)**.

In spite of the very large variety of push-pull polymers, relatively few examples of vinylene-linked conjugated polymers for OPV, where the π electron-rich and the π electron-poor moieties are heteroaromatic fragments separated by a vinylene (V) spacer, have been described. This could be mostly due to the more stringent synthetic issues and to the lack of convenient commercial precursors. However incorporating vinylene bonds in an aromatic polymer backbone could lead to an increase of the degree of coplanarity of the polymer monomeric units, as the vinylene bond reduces steric hindrance of nearby aromatic rings,^[55] thus leading to enhanced π -conjugation, intermolecular π -stacking, and, accordingly, reduced bandgap.^[56] Swager, Epstein and coworkers have pioneered the use of V-linked push-pull polymers with π electron rich alkoxybenzene rings^[57] as alternatives to conventional poly(p-phenylenevinylene) (PPV) systems.^[58] Naso, Farinola and coworkers have investigated several fluorinated PPVs.^[59] Reynolds et al. have recently reported a vinylene-linked BTD-based polymer with a low bandgap energy (1.7 eV) but still modest OPV efficiencies (0.3%).^[60] Abbotto et al. has recently described two V-linked push-pull polymers where the electron-poor moiety was a pyridine ring with different substitution patterns and the electron-rich moiety was either 3,4-ethylenedioxythiophene (EDOT),^[61] or pyrrole.^[62] The energetic characterization of the EDOT polymers **P(2,5-Py-V-EDOT)** and **P(2,6-Py-V-EDOT)** revealed HOMO (-5.1/-5.0 eV), LUMO (-3.4 eV) and narrow bandgap (1.6/1.7 eV) energies fitting materials-design rules for optimized OPV. However, as for Reynolds's case, photovoltaic devices in combination with PC₇₁BM afforded a relatively modest PCE of $\sim 0.5\%$ (AM 1.5G, 100 mW/cm²), which was mostly attributed to the low molecular-weight of the polymers accessible via the chemical route.

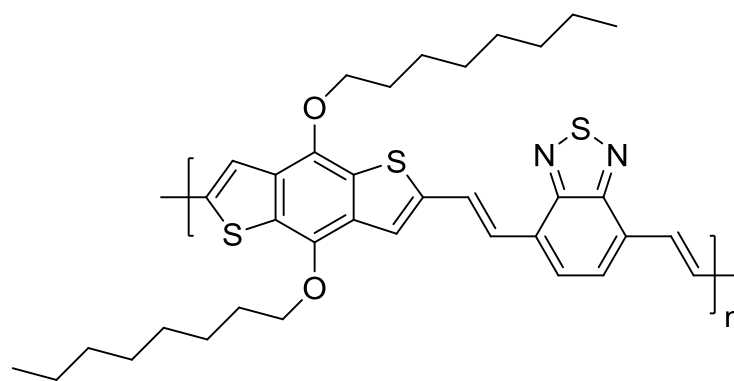


Figure 21 Structure of the polymer **P(BDT-V-BTD)** investigated in this work.

The first example of a vinylene-linked **BDT-BTD** low-bandgap polymer **P(BDT-V-BTD)** (**Figure 21**) is presented here. The polymer has been synthesized via metal catalyzed poly-coupling reaction and fully characterized in its optical, electrochemical, charge carrier mobility, and photovoltaic properties. DFT/TDDFT computations have been performed for model oligomers to analyze their optical and electronic properties.

2.2.2. Experimental

2.2.2.1. Polymer characterization and computational investigations

Absorption spectra were recorded on a V-570 Jasco spectrophotometer. Transition temperatures were determined by DSC using a Mettler Toledo DSC 821 instrument with a heating and cooling rate of 15 °C/min under nitrogen. TGA was performed with a Mettler Toledo TGA/DSC STARE system at a heating rate of 10 °C/min under nitrogen. GPC analyses was recorded on a Waters 1515 separation module using polystyrene as a standard and THF as an eluant.

The electrochemical characterization was performed by differential pulsed voltammetry (DPV) and cyclic voltammetry in a two compartment three electrode cell assembled in an Argon filled glove box ($[O_2] < 1$ ppm) using an EG&G PARSTAT 2263 potentiostat/galvanostat. A gold disc, a Pt flag, and a Ag/AgCl wire were used as working, counter, and pseudoreference electrode, respectively. The electrolyte was a 0.1 M solution of tetrabutylammonium perchlorate (Fluka, electrochemical grade, $\geq 99.0\%$) in anhydrous dichloromethane (Sigma Aldrich $> 99.8\%$). The working electrode disc was well polished with an 0.1 μm alumina suspension, sonicated for 15 min in deionized water and washed with 2-propanol before use. The pseudoreference electrode was calibrated either by adding ferrocene (0.5 mM) to test solution (reductive DPV) or externally by a 0.5 mM solution of ferrocene in the electrolyte (in absence of the polymer). Both calibrations provided the same result; the corresponding cathodic peak potentials differed for less than 5 mV.

Some computational investigations have been performed with the Gaussian 03 program package.^[63] 3-21G* and 6-31G* basis sets were used for geometry

optimizations. A 6-31G* basis set were used for single point energy calculations. For all calculations, a polarizable continuum model (PCM) to describe solvation effects has been used.^[64]

2.2.2.2. Devices fabrication and characterization

Photovoltaic devices were fabricated with the standard architecture ITO/PEDOT:PSS/**P(BDT-V-BTD)**:PC_{xx}BM/LiF/Al. Indium-Tin Oxide (ITO) covered glass substrates (sheet resistance $\sim 10 \Omega/\text{sq}$) were cleaned sequentially by ultrasonic treatment in deionized water, acetone and isopropyl alcohol, then dried and placed in a Oxygen/UV plasma chamber cleaner for 10 minutes. A poly(3,4-ethylenedioxythiophene) /poly(styrenesulfonate) (PEDOT:PSS) (Baytron P) layer about 80 nm thick was spin-coated at 2000 rpm (60 s) onto the substrates, followed by annealing at 150 °C for 30 minutes. PC₆₁BM and PC₇₁BM were bought from American Dye Source. Two blended solutions of **P(BDT-V-BTD)** and PC₆₁BM in dry CHCl₃ were prepared, with polymer concentration of 7 mg/mL and PC₆₁BM concentrations of 7 and 10.5 mg/mL, leading to solutions with polymer:fullerene weight ratios of 1:1 and 1:1.5 respectively. Another solution was prepared with **P(BDT-V-BTD)** (7 mg/mL) and PC₇₁BM (10.5 mg/mL) in dry CHCl₃ leading to a solution with **P(BDT-V-BTD)**:PC₇₁BM weight ratio of 1:1.5. Blend solutions were kept in an ultrasonic bath for 2 hours, then spin-coated in air at 1500 rpm for 60 seconds onto glass/ITO/PEDOT:PSS substrates (active layer thickness 50 nm). LiF and Al cathodes (0.6 nm and 70 nm thick) were deposited sequentially through a mask on top of the active layer in a vacuum chamber at a pressure of $\sim 10^{-6}$ Torr. The active area of the device was 6 mm². Current density-voltage curves were recorded with a Keithley 236 source-meter unit by illuminating a single device through a mask with simulated AM 1.5G irradiation (100 mW/cm²) from an Abet Technologies Sun 2000 Solar Simulator. All devices were tested in oxygen and water free environment inside a glove box filled with nitrogen. The thicknesses of the films were measured by a profilometer. AFM images were taken with a Solver Pro (NTMDT) scanning probe microscope in semi-contact tapping mode. Absorption of thin films was measured using a JASCO spectrometer.

EQE was measured with a home built system on encapsulated devices: monochromatic light was obtained with a Xenon arc lamp from Lot-Oriel (300 Watt power) coupled with a Spectra-Pro monochromator. The photocurrent produced by the device passed through a calibrated resistance (51 Ohms) and the Voltage signal was collected after the resistance with a Merlin Lock-In Digital Amplifier. Signal was pulsed by means of an optical chopper (around 500 Hz frequency). IQE was calculated starting from the EQE and absorption spectra, taking into account the following assumptions: i) 7% of incident light is reflected at the air /glass interface, ii) the Al contact is considered a perfect mirror, therefore the fraction of light absorbed by the active layer (A%) is calculated from the doubled absorption spectrum (Abs) of the active layer, as in **Equation 15**:

$$A\% = 1 - 10^{-2Abs} \quad \text{Eq. 15}$$

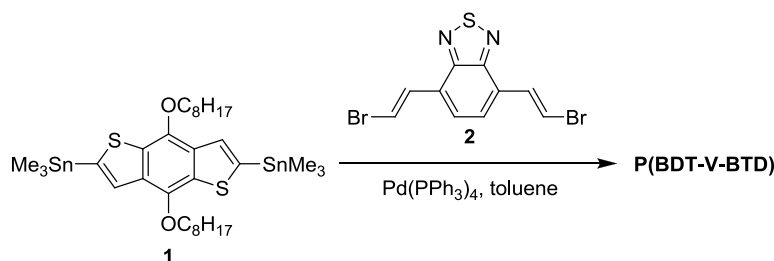
thus $IQE = EQE/A\%$.

Bottom-gate/top-contact OFETs were fabricated on hexamethyldisilazane (HMDS)-treated, p-doped Silicon wafers covered with a SiO₂ dielectric layer. Trimethylsilation of the SiO₂ surface was done by exposure to HMDS vapours in air-free, room temperature reaction. **P(BDT-V-BTD):PC₆₁BM** 1:1.5 (w/w) or **P(BDT-V-BTD)** pristine films were prepared in the same condition used for the OPVs active layers preparation. To complete the OFET devices, 50 nm of Au were thermally evaporated over the semiconducting layer through a shadow mask in a vacuum chamber at a pressure of $\sim 10^{-6}$ Torr to yield the source and drain electrodes (channel length = 1000 μm and channel width = 70 μm).

2.2.3. Results and Discussion

2.2.3.1. Synthesis, chemical characterization, and optical properties

The polymer synthesis and NMR, GPC, DSC and TGA characterization was done in Prof. Abbotto group at University of Milano-Bicocca, Italy. **P(BDT-V-BTD)** was obtained according to **Scheme 6** by a Stille poly-cross-coupling reaction catalyzed by Pd(PPh₃)₄ starting from the bis-trimethyltin derivative **1** and the bis-2-bromovinyl BTD derivative **2**.



Scheme 6 Synthesis of the polymer **P(BDT-V-BTD)**.

Polymerization proceeded in good yields producing materials with moderate number-average molecular weights. The polymer was precipitated in methanol, collected by filtration, and purified by Soxhlet extraction. Low-molecular-weight oligomers were removed by extraction with *n*-hexane. The soluble higher-molecular-weight fraction was extracted with chloroform with a significant portion of solid residue, not soluble in common organic solvents, remaining in the Soxhlet thimble.

¹H NMR spectra confirmed the polymer structure. UV-vis spectroscopy, GPC, DSC, and TGA were used to characterize the new polymer. **Table 4** summarizes the main structural, optical, and thermal properties of the polymer along with those of the reference polymer **P(BDT-BTD)** containing the same donor and acceptor heteroaromatic units but without the vinylene spacer.^[54a]

A second polymer, where the two linear octyl chains of the BDT unit were replaced by two 2-ethylhexyl branched chains, was prepared starting from the corresponding bis-trimethyltin precursor.^[54b] Although photophysical properties were similar to that of the octyl derivative, solubility and film processability unexpectedly resulted poorer and no significant photovoltaic response in OPV cells in combination with PC₆₁BM or PC₇₁BM was measured. For these reasons the 2-ethylhexyl substituted polymer was no further considered in this work.

The GPC data revealed molecular-weights which are somewhat smaller than **P(BDT-BTD)**. The small optical bandgap (around 1.7 eV) calculated is in perfect agreement with that observed for reference **P(BDT-BTD)**.

Table 4. Structural and optical properties of **P(BDT-V-BTD)** in CHCl₃ solution and as a thin film and comparison with reference polymers. [a] obtained by GPC. [b] optical bandgap, calculated on the low energetic edge of the absorption spectrum, λ_o , as $E_{gap}^o = 1240/\lambda$. [c] Glass transition temperature determined by DSC; [d] Decomposition temperature determined by TGA (5% weight loss). [e] From ref. 16a. [f] Data in THF.

Polymer	$M_w^{[a]}$ (kg mol ⁻¹)	$M_n^{[a]}$ (kg mol ⁻¹)	PDI	CHCl ₃ solution			film			$T_g^{[c]}$ (°C)	$T_d^{[d]}$ (°C)
				λ_{max} (nm)	λ_o (nm)	E_{gap}^o [b] (eV)	λ_{max} (nm)	λ_o (nm)	E_{gap}^o [b] (eV)		
P(BDT-V-BTD)	12.3	7.2	1.7	560	730	1.7	561	850	1.5	-	330
P(BDT-BTD) ^[e]	31	18	1.7	591 ^[f]	730 ^[f]	1.7 ^[f]	595	850	1.5	-	270

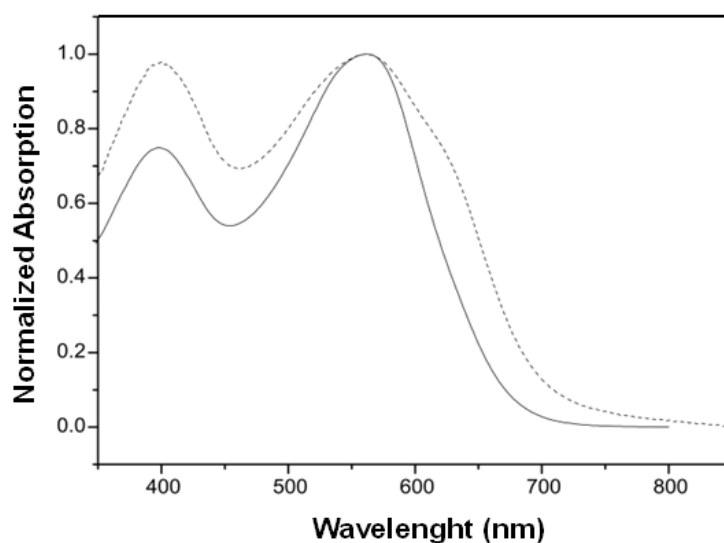


Figure 22 Normalized absorption spectra of **P(BDT-V-BTD)** measured in CHCl₃ solution (solid line) and as thin film (dashed line).

Figure 22 shows the UV-Vis spectra in solution and as thin film of **P(BDT-V-BTD)**. When measured as thin film, the absorption spectrum of **P(BDT-V-BTD)** is broadened in the low-energy portion, likely due to aggregated networks from π - π interactions in the solid state also arising from the vinylene-induced increased planarity. This results in lower energy absorption onset and optical bandgap (1.5 eV), again as similarly found for **P(BDT-BTD)**. A thermogravimetric and differential scanning calorimetry analysis was carried out in order to determine the thermal stability and transitions of the new polymer. The polymer exhibited a reasonable thermal stability with a degradation temperature above 300 °C and higher than that of the reference polymer (**Table 4**). The thermal stability is therefore satisfactory for use in OPVs and other optoelectronic devices. The DSC scan revealed no obvious thermal transitions in the temperature range from 25 to 400 °C.

2.2.3.2. Electrochemical characterization

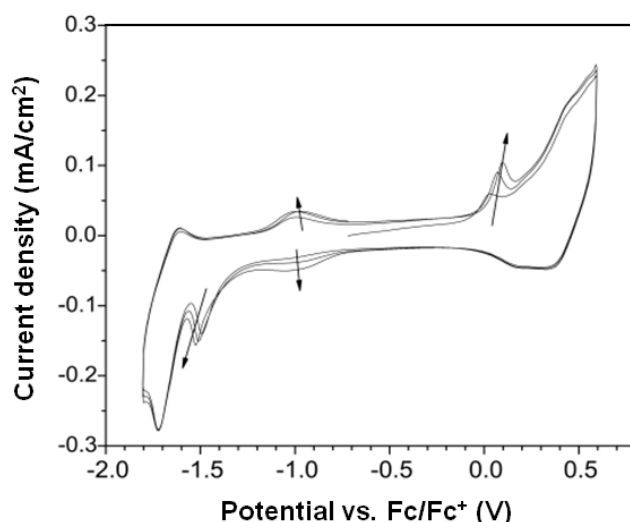


Figure 23 Full range CV of **P(BDT-V-BTD)** in 0.1 M TBAPF₆ CH₂Cl₂ solution at 20 mV/s.

The electrochemical characterization was done in Prof. Abbotto group at University of Milano-Bicocca, Italy. The polymer powder was dissolved (0.5 mM) in an electrolyte solution of 0.1 M tetrabutylammonium perchlorate (TBAClO₄) in CH₂Cl₂. Cyclic voltammeteries performed in the potential range between 0.7 and -1.8 V showed several redox processes (**Figure 23**). Oligomer oxidation and reduction processes lie at potential above 0.2 and below -1.5 V, respectively, and the corresponding peak positions and currents are stable upon cycling. Before both processes, sharp charge-trapping-like peaks were observed, the current and potential of which shifted cycle by cycle. The reversible redox process at around -1.0 V was observed only after the first scan. The process increased upon cycling

and is likely due to the redox system of coupled chains which grows at high oxidative potentials (> 0.5 V).

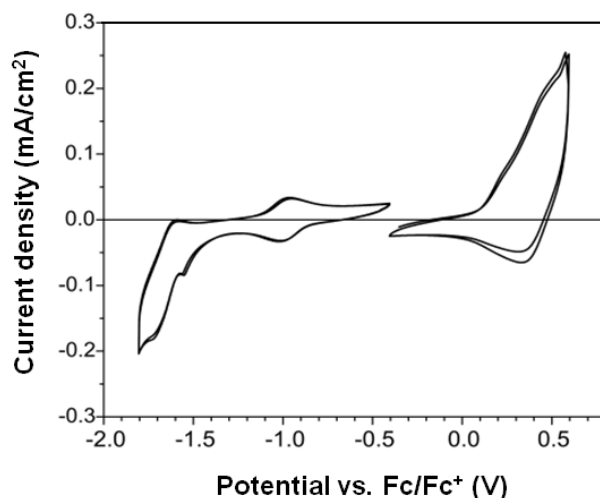


Figure 24 CVs of **P(BDT-V-BTD)** in 0.1 M TBAPF₆ CH₂Cl₂ solution at 20 mV/s performed in different potential ranges.

To better understand the electrochemical behaviour, the two potential regions wherein oligomers oxidation and reduction take place were separately explored (**Figure 24**). Here the charge trapping peaks were no longer visible and accordingly the current relative to the intermediate potential redox process did not increase.

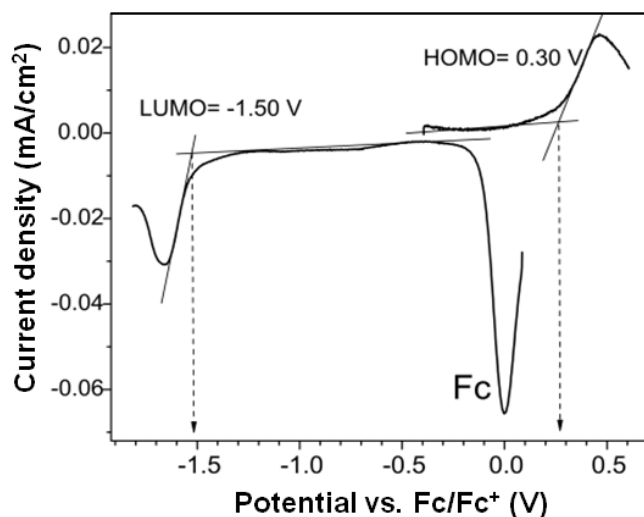


Figure 25 DPVs of **P(BDT-V-BTD)** in 0.1 M TBAPF₆ CH₂Cl₂ solution at 10 mV/s.

HOMO-LUMO energy values were determined by Differential Pulsed Voltammetry (**Figure 25**). Since both peaks showed irreversible features compared to the peak of the internal standard (Fc/Fc⁺), in this specific case energy values were estimated by the onsets of the rising currents. The onsets were calculated by taking the intercepts between peak tangent and current baseline.

The results are collected in **Table 5** along with those of the reference polymer.

Table 5 Electrochemical properties of P(BDT-V-BTD) in 0.1 M TBAPF6 CH₂Cl₂ solution and comparison with reference polymers. All potentials are reported vs. Fc/Fc⁺ and HOMO and LUMO energies are derived from the electrochemical data based on the assumption that the Fc/Fc⁺ redox couple is 5.2 eV relative to vacuum. [a] Electrochemical bandgap, obtained from the difference between the reduction and the oxidation potential onset (or LUMO and HOMO energies). [b] From ref. 16a. [c] HOMO and LUMO recalculated from ref. 16a by considering that the Fc/Fc⁺ redox couple is 5.2 eV relative to vacuum.

Polymer	E _{ox} ^o (V)	HOMO (eV)	E _{red} ^o (V)	LUMO (eV)	E _{gap} ^{EC} [a] (eV)
P(BDT-V-BTD)	0.30	-5.5	-1.50	-3.7	1.8
P(BDT-BTD) ^[b]		-5.1 (-5.6) ^[c]		-3.2 (-3.7) ^[c]	1.9

The different energetic values with respect to reference **P(BDT-BTD)** are somehow difficult to explain, being the acceptor and donor components identical. Indeed, if the data for **P(BDT-BTD)**^[54a] are re-calibrated (the pseudo-reference Ag electrode re-calibrated vs. ferrocene) the oxidation/reduction onsets lie in a potential region very similar to the vinylene-linked polymer. Thus, the recalculated HOMO/LUMO levels of the **P(BDT-BTD)** were actually in excellent agreement with those of **P(BDT-V-BTD)**.

2.2.3.3. Structural theoretical calculations

To get insight into the structural properties of the investigated systems, some simple theoretical calculations on the monomers **BDT-V-BTD** and **BDT-BTD** and on their selected oligomers **(BDT-V-BTD)_n** and **(BDT-BTD)_n** were performed by Dr. De Angelis group at ISTM-CNR of Perugia, Italy. To reduce the computational overhead, the n-octyl and n-dodecyl chains of the monomers **BDT-V-BTD** and **BDT-BTD** were replaced with a methyl (-CH₃) substituent, thus looking at the **P(Me-BDT-V-BTD)** and **P(Me-BDT-BTD)** models. In particular, the theoretical study of a polymeric systems can be performed via two different approaches: (i) by considering the infinite polymer as a periodic system, and (ii) by analyzing extended systems with increasing but finite dimension.^[61] Here the second approach has been chosen.

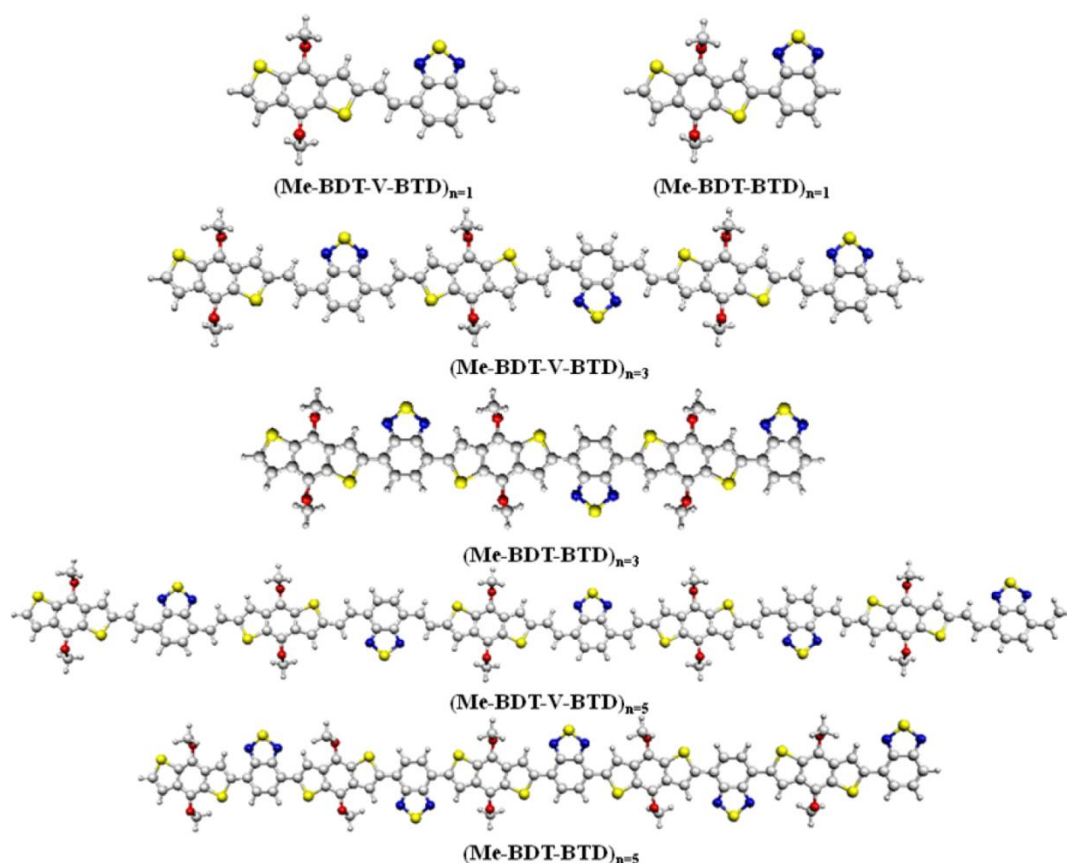


Figure 26 Optimized geometries of **(Me-BDT-V-BTD)_n** and **(Me-BDT-BTD)_n** monomers ($n = 1$) and oligomers ($n = 3, 5$).

The optimized geometries of representative systems are shown in **Figure 26**. The optimized structures are planar in all cases, apart from the methoxy groups lying outside the plane. This suggests that in the **P(BDT-V-BTD)**, the -V- spacer does not have a major role in helping the planarization of the polymer backbone, but it could rather have an influence on the polymer solid state morphology, electronic and optical properties.

2.2.3.4. Photovoltaic properties

The use of **P(BDT-V-BTD)** in combination with fullerene derivatives ($PC_{61}BM$ and $PC_{71}BM$) as donor and acceptor materials in BHJ OPV devices was investigated. The standard OPV configuration glass/ITO/PEDOT:PSS/donor:acceptor/LiF/Al was used. Devices fabrication details are reported in the Experimental Section.

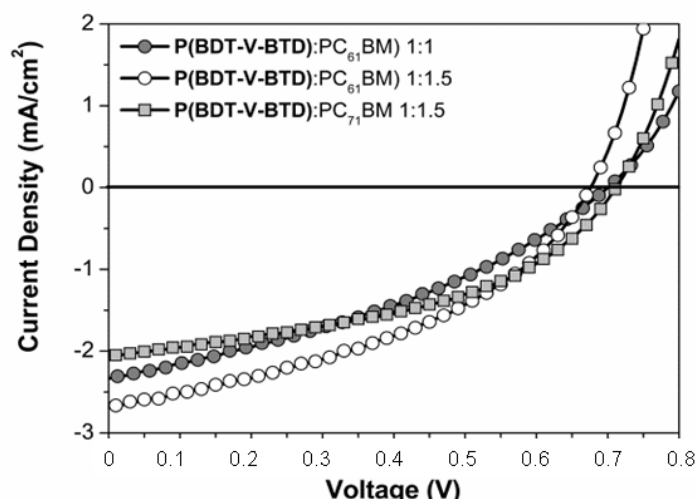


Figure 27 J-V curves, under illumination, of optimized **P(BDT-V-BTD):PCBM** solar cells.

Table 6 Photovoltaic parameters of optimized **P(BDT-V-BTD):PCBM** based devices, compared to reference polymer **P(BDT-BTD)** solar cell. [a] Values taken from ref 16a.

Materials	D:A ratio (wt/wt)	J_{sc} (mA/cm ²)	V_{oc} (V)	FF (%)	PCE (%)
P(BDT-V-BTD): PC ₆₁ BM	1.2:1	2.20	0.70	34	0.52
P(BDT-V-BTD): PC ₆₁ BM	1:1	2.34	0.70	35	0.58
P(BDT-V-BTD): PC ₆₁ BM	1:1.5	2.69	0.68	41	0.74
P(BDT-V-BTD): PC ₇₁ BM	1:1.5	2.05	0.71	45	0.66
P(BDT-V-BTD): PC ₆₁ BM	1:1.8	2.24	0.68	38	0.58
P(BDT-BTD): PC ₆₁ BM ^[a]	1:1	2.97	0.68	44	0.90

Figure 27 shows the characteristic current density-voltage plots of the most representative solar cells with different donor:acceptor weight ratios and different acceptors, measured under standard AM 1.5G illumination.

The best performing device yielded a PCE of 0.74% with current density, open circuit voltage and fill factor of 2.69 mA cm⁻², 0.68 V, and 41%, respectively (**Table 6**). The V_{oc} values measured for the **P(BDT-V-BTD)** based devices are almost independent on the blend composition and on the acceptor (PC₆₁BM or PC₇₁BM). The mean V_{oc} value of 0.68 V well matches with the V_{oc} reported for solar cells based on the analogous single bonded **P(BDT-BTD)** donor material (see **Table 6**), in agreement with the similar molecular structure and the HOMO energy levels of the two polymers (**Table 5**). On the other hand, within all **P(BDT-V-BTD)** based solar cells, the measured FF and J_{sc} did not exceed 45% and 2.69 mA cm⁻², respectively. This could be due to unfavourable thin-film electrical and/or morphological characteristics hampering the PCEs of the devices, despite the optimization of the polymer optoelectronic properties.

Many efforts to improve the device performances were carried out by following a variety of strategies. In general, the variation of the donor:acceptor blend ratios is well known to affect significantly the photovoltaic parameters. By increasing the polymer amount in the blend films, going from 1:1 to 1.2:1 **P(BDT-V-BTD):PC₆₁BM** weight ratio, corresponding to blend films with an excess of polymer, we observed a slight decrease of the overall OPV performance (PCE going from 0.58 to 0.52, mainly due to decreased J_{sc} and FF) (**Table 6**). On the opposite, by increasing the PC₆₁BM content, from 1:1 to 1:1.5 D:A weight ratio, a raise in J_{sc} (from 2.34 to 2.69 mA cm⁻²) and FF (from 35% to 41%) were obtained, leading to a PCE of 0.74%. These results could be likely ascribed to enhanced charge separation and transport processes in the active blend due to a more favorable self-organization of the interpenetrating donor and acceptor phases. A further increase of the PC₆₁BM content led to reduced J_{sc} , and consequently PCEs (**Table 6**), confirming the best donor:acceptor blend weight ratio of 1:1.5.

It is well known that thermal and solvent annealing of the active layer or of complete BHJ OPV devices could lead to improved blend film nano-morphology, electrical properties and device performances.^[65] It was found that thin film thermal annealing in the range 60-140 °C, and for different times, resulted in film degradation, adversely affecting photovoltaic parameters. Moreover, different solvents (e.g., toluene, chlorobenzene and ortho-dichlorobenzene) were used to spin-cast the blends, but poor quality films were obtained as a consequence of the limited polymer solubility. The most macroscopically homogeneous and electrically uniform films were obtained from chloroform solutions, resulting in the best OPV performances.

In order to increase the device photocurrent generation, strategies to improve the light collection ability of the blend film were carried out. The photocurrent generation, together with other parameters such as hole mobility, optimum annealing temperature and ideal morphology, is also determined by the amount of photons absorbed by the active layer, which in turns depends on the onset wavelength of the polymer (E_{gap}^0) and on the film absorbance.

A high polymer absorption molar coefficient (ϵ) is obtained in solution ($\epsilon_{max} = 3.5 \times 10^5 \text{ mol}^{-1}\text{cm}^{-1}$ considering $M_w = 12.3 \text{ kg mol}^{-1}$), which is of the same order of magnitude of other well performing OPV polymers.^[66] Therefore, in addition to the intrinsically high polymer molar absorption, the active layer film thickness was increased with the aim to enhance the overall blend film absorbance. Indeed, in **P(BDT-V-BTD):PC₆₁BM** based devices, increasing the film thickness up to 50 nm led to an improvement in photocurrent generation and overall efficiency. However, a further increase in the active layer thickness, although leading to enhanced film absorbance, did not afford improved J_{sc} and PCE. Optimized 50-nm thick active layer films showed absorbance values lower than 0.3 over the visible spectral window. Therefore, it is likely that such low film absorption, limited by thickness (50 nm), besides other morphological and electrical device features, is an important factor limiting the photocurrent response of **P(BDT-V-BTD)** based devices. On the other hand, since the active layers in optimized devices still have >

50% transparency in the visible region, their potential use as photoactive materials in semi-transparent cells for tandem or stackable devices could be considered in future works on **P(BDT-V-BTD)** based devices.^[67]

An additional strategy to improve the photocurrent response of **P(BDT-V-BTD)** based solar cells is based on the replacement of PC₆₁BM with PC₇₁BM as acceptor material in the active layer, in order to exploit the superior light harvesting properties of the latter in the visible region.^[68] Although an enhancement in the absorption spectrum of the **P(BDT-V-BTD):PC₇₁BM** blend film was recorded in comparison with the analogous PC₆₁BM based film, no significant improvements of PCE values were observed (**Table 6**). This result might be attributed to the possible PC₇₁BM aggregation tendency and its poor miscibility with the polymer, resulting in lower thin-film quality with limited nanoscale morphology, phase separation and, thereby, inferior electrical properties compared to PC₆₁BM based devices.^[69]

Hole mobility (μ_h) of **P(BDT-V-BTD)** based films was measured in order to investigate the polymer charge carrier transport properties which, together with other parameters such as optical absorption, morphology and energetic levels alignment, affect the performances of a donor material in BHJ OPV devices. The μ_h of the polymer in pristine and blended films (with PC₆₁BM) was measured in organic field effect transistor (OFET) devices.^[70] The transfer plots of a top-contact OFET prepared with optimized **P(BDT-V-BTD)** film spun on Si/SiO₂/HDMS showed, as expected, a p-type behaviour with $\mu_h = 6.3 \cdot 10^{-5} \text{ cm}^2 \text{ V}^{-1} \text{ s}^{-1}$, in agreement with other low band-gap polymers showing similar OFET hole mobilities and comparable or better photovoltaic performances compared to **P(BDT-V-BTD)**.^[61,71] Moreover, OFET devices prepared with optimized **P(BDT-V-BTD):PC₆₁BM** film exhibited a μ_h value of $4.6 \cdot 10^{-5} \text{ cm}^2 \text{ V}^{-1} \text{ s}^{-1}$, very similar to that measured for the polymer alone, indicating that the presence of PC₆₁BM does not significantly affect the morphology and the continuity of the polymer phase.

Polymer carrier mobility is strictly correlated with molecular weight and nano-morphology. In particular, recent works on P3HT clearly confirmed the relationship between polymer charge carrier mobility, OPV performance, and molecular weight.^[72] In fact it was demonstrated that P3HT OFET mobility is controlled by the probability of carriers to cross the low-conductive disordered regions lying within the highly-conductive crystalline domains. This probability is higher for high molecular weight P3HT samples where molecular connections bridge the crystalline domains, while it is lower in low molecular weight P3HT films where the inter-crystalline molecular connections are missing. Therefore, it is possible that the relatively low molecular weight of **P(BDT-V-BTD)**, which affects the polymer electrical and morphological characteristics, could represent one of the critical factor that limits the photovoltaic performance of the corresponding BHJ solar cells.

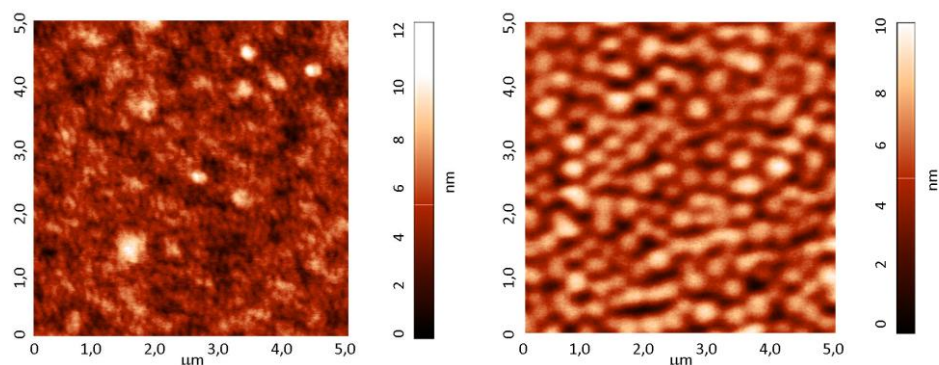


Figure 28 AFM topographic images of: **a)** the **P(BDT-V-BTD):PC₆₁BM** and **b)** **P(BDT-V-BTD):PC₇₁BM** blend films affording the best OPV performances.

To get an insight into the micro- and nano-structural organization of the polymer in the active layer, the morphological features of the **P(BDT-V-BTD):PC₆₁BM** and **P(BDT-V-BTD):PC₇₁BM** blend films affording the best OPV performances were investigated by tapping-mode AFM.

The measurements revealed surface roughness (RMS) of ~ 1.3 and ~ 1.5 nm for the **P(BDT-V-BTD):PC₆₁BM** and the **P(BDT-V-BTD):PC₇₁BM** films, respectively (**Figure 28a** and **b** respectively), suggesting a smooth and homogeneous surface of the blends. The two thin films have similar morphologies but different domain size, which depends on the nature of the acceptor in the blend. **P(BDT-V-BTD):PC₆₁BM** film exhibits smaller features with respect to the **P(BDT-V-BTD):PC₇₁BM** film, likely due to the lower aggregation tendency of PC₆₁BM compared to PC₇₁BM.^[69] This might also justify the better performance of the PC₆₁BM based devices.

To analyze the spectral response of the best performing solar cell, the EQE spectrum of **P(BDT-V-BTD):PC₆₁BM** 1:1.5 (wt/wt) based device was measured.

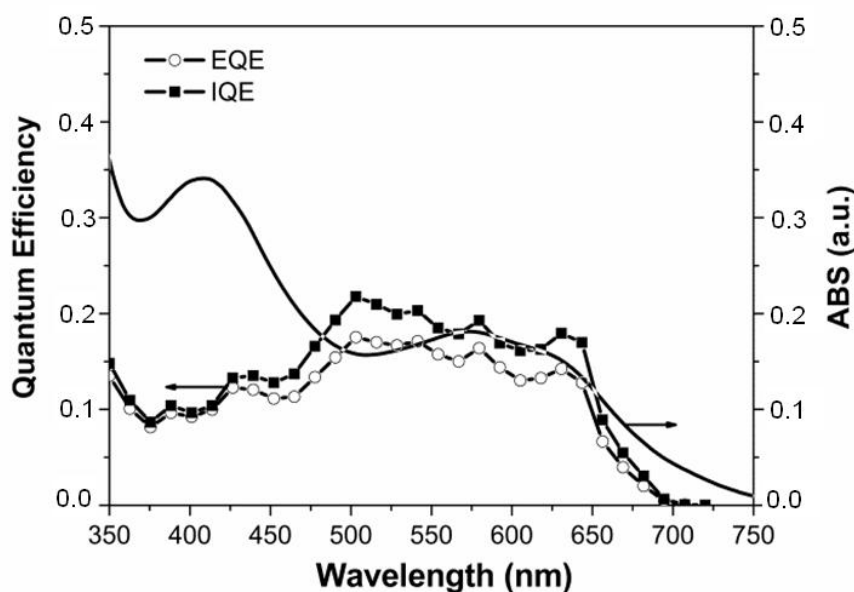


Figure 29 EQE (open circles) and IQE (filled squares) spectra of optimized **P(BDT-V-BTD):PC₆₁BM**, 1:1.5 (w/w) devices. The absorption spectrum of the active layer (black line) is included for comparison.

The EQE spectrum (**Figure 29**) shows the highest generated-electrons over incident-photons ratio, comprised within 0.15 and 0.17, in the spectral range between 450 and 650 nm, which corresponds to the lower-energy absorption band of the polymer. This indicates that photocurrent mainly arises from the absorption of **P(BDT-V-BTD)** in the photoactive layer. The short-circuit current density of the device inferred from convoluting the EQE over the entire wavelength range (350 – 750 nm) matches well, within the experimental error, with the J_{sc} value obtained in the J-V curve measurement (2.53 and 2.69 mA cm⁻², respectively). An estimation of the IQE of the (BDT-V-BTD):PC₆₁BM 1:1.5 (w/w) device is also given in **Figure 29**. While IQE values inferior to unity over the entire spectral range reveal limited photocurrent generation capability of the device,^[73] the fraction of light absorbed by the active layer (A%, calculated from Absorbance, see Experimental Section) results as high as 0.8 in the range 450 – 650 nm, which is consistent with the similarity of the IQE and EQE curves. Therefore, the modest photocurrent generation capability in the optimized **P(BDT-V-BTD):PC₆₁BM** devices has rather to be attributed to limited polymer charge mobility than to poor active layer light collection efficiency.

2.2.4. Conclusions

A new heteroarylene-vinylene donor-acceptor low bandgap polymer is presented. The design has been based on the unprecedented combination of strong π electron-rich (BDT) and π electron-poor (BTD) alternating units together with a vinylene spacer in order to exploit increased planarization along the π backbone and efficient π delocalization with respect to the most common approach in the literature presenting direct aryl-aryl connection.

The electrochemical investigation has highlighted the ambipolar character of the new polymer, with both p- and n-doping processes being observable. The coupling of the two strong π electron-rich and π electron-poor moieties effectively led to the obtainment of the low band gap **P(BDT-V-BTD)** polymer, with HOMO and LUMO energies in agreement with the reference **P(BDT-BTD)**. On the other hand, the presence of the vinylene spacer allowed for lower bandgap energies and improved thermal stability compared to the corresponding species with direct bonding between the two heteroaromatic units. In conclusion, the experimental studies have ascertained structural, photophysical, and electronic properties matching optimal materials design rules for efficient donor polymers in OPV devices. Investigation of the photovoltaic properties in BHJ OPV devices containing **P(BDT-V-BTD)** as the donor has given high photovoltages but low photocurrents, comparing to the reference polymer. The still non-optimal thin-film nano-morphologies and hole mobility properties, likely due to the relatively low molecular weight, could account for the modest PCE lower than 1%, which is nonetheless similar to those obtained for the reference **P(BDT-BTD)**. Efforts are

under way to efficiently convert the encouraging properties of these heteroarylene-vinylene donor-acceptor polymers into more efficient OPV devices.

3. CONCLUSIONS

In this chapter some of the strategies for the optimization of the performances of BHJ OPV devices by the accurate study and tuning of the properties of the polymeric donor material have been investigated. In particular, the strategy of using push-pull polymers, having electron withdrawing and electron donating alternate units, has been explored.

In the first family of newly synthesized polymers studied, the electron rich unit di-thieno-silole (SiDT) was coupled with differently substituted dithiophene and terthiophene electron rich moieties in four different push-pull polymers. The strategy included the incorporation of strongly electron withdrawing substituents (-CN) on the thiophene-based unit, in order to lower the bandgap and the HOMO and LUMO energies of the polymer, enhancing its optical, photophysical and photovoltaic properties. Moreover, alkylthiophene chains were added on the quarter-thiophene moiety in order to increase the polymer solubility and electrical properties (light absorption and hole mobility) and also to improve the nanostructuring and opto-electrical properties of the corresponding blend films. As a result of the application of these strategies, while the PCEs of OPV devices prepared with SiDT-unsubstituted dithiophene based polymer were lower than 1%, the cells based on SiDT and substituted quaterthiophene electron poor and rich monomeric units respectively exhibited PCEs approaching 5%, with V_{oc} , J_{sc} and FF of 850 mV, 9.25 mA/cm² and 63 %, respectively.

On the other hand, in a new heteroarylene-vinylene push-pull low bandgap polymer, the unprecedented combination of the strong π electron-rich (BDT) and the π electron-poor (BTD) alternating units separated by a vinylene spacer was studied. The presence of the vinylene linker led to increased planarization along the π backbone and efficient π delocalization with respect to reference system, in which the electron rich and poor moieties are directly connected through aryl-aryl ligand. Indeed, while the HOMO and LUMO energies were in agreement with the reference polymer, the presence of the vinylene spacer allowed the lowering of the polymer optical bandgap, probably due to a polymer increased intermolecular π - π stack. As a result of this strategy, high photovoltages (but low photocurrents) were obtained by using this new polymer as donor material in BHJ OPV devices. The still non-optimal thin-film nano-morphologies and hole mobility properties, likely due to the relatively polymer low molecular weight, could account for the modest PCE lower than 1%, which is nonetheless similar to those obtained for the reference polymer in which the two BDT and BTD moieties are directly linked.

The tuning of the chemical structure of the monomeric units, inter-moieties spacers and solubilizing side-groups were then shown to effectively modulate the polymer optical, electrical, morphological, and photophysical properties. The

obtained results combined with a relatively simple synthetic procedures, make the presented approaches a promising benchmark for further developments of new efficient semiconducting donor polymers for applications in BHJ OPVs. Indeed, the device performance could be further improved by the optimization of the photoactive materials taking advantages from the findings and basic considerations reported and discussed in these studies.

4. BIBLIOGRAPHY

- [1] (a) A. Mishra, P. Bauerle, *Angew. Chem. Int. Ed.*, 2012, 51, 2020; (b) A. K. K. Kyaw, D. H. Wang, V. Gupta, J. Zhang, S. Chand, G. C. Bazan, A. J. Heeger, *Adv. Mater.*, 2013, 25, 2397; (c) E. Cantatore, "Applications of Organic and Printed Electronics: A Technology-Enabled Revolution", 2013, Springer-Verlag, p. 27.
- [2] (a) S. Glenis, G. Tourillon, F. Garnir, V. Dyakonov, M. Schwoerer, *Synthetic Metals*, 1993, 54, 427; (b) R. N. Marks, J. J. M. Halls, D. D. C. Bradley, R. H. Friend, A. B. Holmes, *J. Phys. Cond. Matt.*, 1994, 6, 1379; (c) G. Yu, C. Zhang, A. J. Heeger, *Appl. Phys. Lett.*, 1994, 64, 1540.
- [3] G. Yu, J. Gao, J. C. Hummelen, F. Wudl, A. J. Heeger, *Science*, 1995, 270, 1789.
- [4] G. Li, V. Shrotriya, J. Huang, Y. Yao, T. Moriarty, K. Emery, Y. Yang, *Nat. Mater.*, 2005, 4, 864.
- [5] (a) G. Zhao, Y. He, Y. Li, *Adv. Mater.*, 2010, 22, 0. (b) Y. He, Chen, H.-Y., J. Hou, Y. Li, *J. Am. Chem. Soc.*, 2010, 132, 1377.
- [6] (a) J. Y. Kim, K. Lee, N. E. Coates, D. Moses, T.-Q. Nguyen, M. Dante, A. J. Heeger, *Science*, 2007, 317, 222; (b) G. Yu, J. Gao, J. C. Hummelen, F. Wudl, A. J. Heeger, *Science*, 1995, 270, 1789; (c) S. Gunes, H. S. Neugebauer, N. S. Sariciftci, *Chem. Rev.*, 2007, 107, 1324; (d) K. Coakley, M. D. McGehee, *Chem. Mater.*, 2004, 16, 4533; (e) C. J. Brabec, N. S. Sariciftci, J. C. Hummelen, *Adv. Funct. Mater.*, 2001, 11,15; (f) B. C. Thompson, J. M. J. Frechet, *Angew. Chem., Int. Ed.*, 2008, 47, 58; (g) Y. Li, Y. Zou, *Adv. Mater.*, 2008, 20, 2952.
- [7] R. F. Service, *Science*, 2011, 332, 293.
- [8] (a) H. Sirringhaus, *Nat. Mater.*, 2003, 2, 641. (b) A. Pron, P. Rannou, *Progr. Polym. Sci.*, 2002, 27, 135; (c) W. Kowalsky, E. Becker, T. Benstem, H.-H. Johannes, D. Metzendorf, H. Neuner, J. Schobel, *Adv. Solid State Phys.*, 2000, 40, 795; (d) G. Horowitz, *Adv. Mater.*, 1990, 2, 287.
- [9] (a) H. Meier, U. Stalmach, H. Kolshorn, *Acta Polym.*, 1997, 48, 379; (b) J. L. Bredas, R. Silbey, D. S. Boudreaux, R. R. Chance, *J. Am. Chem. Soc.*, 1983, 105, 6555; (c)
- [10] S.-S. Sun, L. R. Dalton, Introduction to organic electronic and optoelectronic materials and devices, CRC press, Taylor and Francis Group, 2008.
- [11] P. M. Beaujuge, C. M. Amb, J. R. Reynolds, *Acc. Chem. Res.*, 2010, 43(11), 1396.
- [12] (a) H. E. Katz, *Chem. Mater.*, 2004, 16, 4748; (b) S. Allard, M. Forster, B. Souharce, H. Thiem, U. Scherf, *Angew. Chem., Int. Ed.*, 2008, 47, 4070.
- [13] R. Hamilton, C. Bailey, W. Duffy, M. Heeney, M. Shkunov, D. Sparrowe, S. Tierney, I. McCulloch, R. J. Kline, D. M. DeLongchamp, M. Chabinyc, *Proc. SPIE, Int. Soc. Opt. Eng.*, 2006, 6336, 158.
- [14] (a) T. Yamamoto, et al., *J. Am. Chem. Soc.*, 1996, 118, 10389; (b) Zhang, Q. T.; Tour, J. M. J. *Am. Chem. Soc.* 1998, 120, 5355-5362.
- [15] (a) H. Y. Chen, J. H. Hou, S. Q. Zhang, Y. Y. Liang, G. W. Yang, Y. Yang, L. P. Yu, Y. Wu, G. Li, *Nature Photon.*, 2009, 3, 649; (b) Y. Y. Liang, D. Q. Feng, Y. Wu, S. T. Tsai, G. Li, C. Ray, L. P. Yu, *J. Am. Chem. Soc.*, 2009, 131, 7792; (c) Y. Y. Liang, Z. Xu, J.

B. Xia, S. T. Tsai, Y. Wu, G. Li, C. Ray, L. P. Yu, *Adv. Mater.* 2010, 22, E135; (d) L. Huo, S. Zhang, X. Guo, F. Xu, Y. Li, J. Hou, *Angew. Chem. Int. Ed.*, 2011, 50, 9697; (e) H. X. Zhou, L. Q. Yang, A. C. Stuart, S. C. Price, S. B. Liu, W. You, *Angew. Chem. Int. Ed.*, 2011, 50, 2995; (f) S. C. Price, A. C. Stuart, L. Yang, H. Zhou, W. You, *J. Am. Chem. Soc.*, 2011, 133, 4625; (g) Y. Huang, X. Guo, F. Liu, L. Huo, Y. Chen, T. P. Russell, C. C. Han, Y. Li, J. Hou, *Adv. Mater.*, 2012, 24, 3383; (k) H.-C. Chen, Y.-H. Chen, C.-C. Liu, Y.-C. Chien, S.-W. Chou, P.-T. Chou, *Chem. Mater.*, 2012, 24, 4766; (l) C. Y. Chang, Y. J. Cheng, S. H. Hung, J. S. Wu, W. S. Kao, C. H. Lee, C. S. Hsu, *Adv. Mater.*, 2012, 24, 549; (m) Y.-X. Xu, C.-C. Chueh, H.-L. Yip, F.-Z. Ding, Y.-X. Li, C.-Z. Li, X. Li, W.-C. Chen, A. K. Y. Jen, *Adv. Mater.*, 2012, 24, 6356; (n) X. Guo, M. Zhang, J. Tan, S. Zhang, L. Huo, W. Hu, Y. Li, J. Hou, *Adv. Mater.*, 2012, 24, 6536; (o) H. J. Son, L. Lu, W. Chen, T. Xu, T. Zheng, B. Carsten, J. Strzalka, S. B. Darling, L. X. Chen, L. Yu, *Adv. Mater.*, 2012, 25, 838; (p) L. Dou, W.-H. Chang, J. Gao, C.-C. Chen, J. You, Y. Yang, *Adv. Mater.*, 2012, 25, 825; (q) M. S. Su, C. Y. Kuo, M. C. Yuan, U. S. Jeng, C. J. Su, K. H. Wei, *Adv. Mater.* 2011, 23, 3315; (r) H. Yan, M.-H. Yoon, A. Facchetti, T. Marks, *J. Appl. Phys. Lett.*, 2005, 87, 183501.

[16] (a) J. Ohshita, K. Kimura, K.-H. Lee, A. Kunai, Y.-W. Kwak, E.-C. Son, Y. Kunugi, *J. Polym. Sci., Part A: Polym. Chem.*, 2007, 45, 4588; (b) K. L. Chan, M. J. McKiernan, C. R. Towns, A. B. Holmes, *J. Am. Chem. Soc.* 2005, 127, 7662; (c) M. S. Liu, J. D. Luo, A. K. Y. Jen, *Chem. Mater.* 2003, 15, 3496.

[17] (a) H. Huang, J. Youn, R. P. Ortiz, Y. Zheng, A. Facchetti, T. Marks, *Chem Mater.* 2011, 23, 2185; (b) P.M. Beaujuge, W. Pisula, H. N. Tsao, S. Ellinger, K. Mullen, J.R. Reynolds, *J. Am. Chem. Soc.*, 2009, 131, 7514; (c) G. Lu, H. Usta, C. Risko, L. Wang, A. Facchetti, M. A. Ratner, T. J. Marks, *J. Am. Chem. Soc.* 2008, 130, 7670; (d) H. Usta, G. Lu, A. Facchetti, T. J. Marks, *J. Am. Chem. Soc.* 2006, 128, 9034.

[18] (a) X. Guo, N. Zhou, S. J. Lou, J. W. Hennek, R. Ponce Ortiz, M. R. Butler, P.-L. T. Boudreault, J. Strzalka, P.-O. Morin, M. Leclerc, J. T. López Navarrete, M. A. Ratner, L. X. Chen, R. P. H. Chang, A. Facchetti, T. J. Marks, *J. Am. Chem. Soc.* 2012, 134, 18427; (b) I. McCulloch, R. S. Ashraf, L. Biniek, H. Bronstein, C. Combe, J. E. Donaghey, D. I. James, C. B. Nielsen, B. C. Schroeder, W. Zhang, *Acc. Chem. Res.*, 2012, 45, 714; (c) B. C. Schroeder, Z. Huang, R. S. Ashraf, J. Smith, P. D'Angelo, S. E. Watkins, T. D. Anthopoulos, J. R. Durrant, I. McCulloch, *Adv. Funct. Mater.* 2012, 22, 1663; (d) J. Hou, H.-Y. Chen, S. Zhang, G. Li, Y. Yang, *J. Am. Chem. Soc.* 2008, 130, 16144.

[19] (a) C. Risko, G. P. Kushto, Z. H. Kafafi, J. L. Bredas, *J. Chem. Phys.* 2004, 121, 9031; (b) X. W. Zhan, C. Risko, F. Amy, C. Chan, W. Zhao, S. Barlow, A. Kahn, J. L. Bredas, S. R. Marder, *J. Am. Chem. Soc.* 2005, 127, 9021.

[20] (a) Y. Liang, D. Feng, Y. Wu, S. T. Tsai, G. Li, C. Ray, L. Yu, *J. Am. Chem. Soc.* 2009, 131, 7792; (b) J. E. Johns, E. A. Muller, J. M. J. Frechet, C. B. Harris, *J. Am. Chem. Soc.* 2010, 132, 15720; (c) T.-Y. Chu, J. Lu, S. Beaupré, Y. Zhang, J.-R. Pouliot, J. Zhou, A. Najari, M. Leclerc, Y. Tao, *Adv. Funct. Mater.* 2012, 22, 2345; (d) Z.-G. Zhang, J. Min, S. Zhang, J. Zhang, M. Zhang, Y. Li, *Chem. Commun.*, 2011, 47, 9474.

[21] R. C. Coffin, J. Peet, J. Rogers, G. C. Bazan, *Nature Chemistry*, 2009, 1, 657.

- [22] T.-Y. Chu, J. Lu, S. Beaupré, Y. Zhang, J.-R. Pouliot, S. Wakim, J. Zhou, M. Leclerc, Z. Li, J. Ding, Y. Tao, *J. Am. Chem. Soc.*, 2011, 133, 4250.
- [23] (a) M. Heeney, C. Bailey, K. Genevicius, M. Shkunov, D. Sparrowe, S. Tierney, I. McCulloch, *J. Am. Chem. Soc.*, 2005, 127, 1078; (b) I. McCulloch et al., *Nat. Mater.* 2006, 5, 328.
- [24] (a) A. Pron, P. Rannou, *Prog. Polym. Sci.*, 2002, 27, 135; (b) I. F. Perepichka, D. F. Perepichka, H. Meng, F. Wudl, *Adv. Mater.*, 2005, 17, 2281.
- [25] (a) N. Zhou, X. Guo, R. Ponce Ortiz, S. Li, S. Zhang, R. P. H. Chang, A. Facchetti, T. J. Marks, *Adv. Mater.* 2012, 24, 2242.
- [26] (a) B. S. Ong, Y. Wu, P. Liu, S. Gardner, *J. Am. Chem. Soc.*, 2004, 126, 3378; (b) J. Ohshita, K. Kimura, K.-H. Lee, A. Kunai, Y.-W. Kwak, E.-C. Son, Y. Kunugi, *J. Polym. Sci., Part A: Polym. Chem.*, 2007, 45, 4588.
- [27] Y. Zhu, R. D. Champion, S. A. Jenekhe, *Macromolecules*, 2006, 39, 8712.
- [28] L. Huo, J. Hou, S. Zhang, H. Y. Chen, Y. Yang, *Angew. Chem. Int. Ed.* 2010, 49, 1500.
- [29] (a) M. C. Scharber, D. Mühlbacher, M. Koppe, P. Denk, C. Waldauf, A. J. Heeger, C. J. Brabec, *Adv. Mater.* 2006, 18, 789; (b) C. J. Brabec, A. Cravino, D. Meissner, N. S. Sariciftci, T. Fromherz, M. T. Rispens, L. Sanchez, J. C. Hummelen, *Adv. Funct. Mater.*, 2001, 11, 374.
- [30] (a) D. S. Chung, D. H. Lee, C. Yang, K. Hong, C. E. Park, J. W. Park and S. K. Kwon, *Appl. Phys. Lett.*, 2008, 93, 033303; (b) P. W. M. Blom, M. J. M. De Jong and J. J. M. Vleggaar, *Appl. Phys. Lett.*, 1996, 68, 3308.
- [31] (a) N. Zhou, X. Guo, R. Ponce Ortiz, S. Li, S. Zhang, R. P. H. Chang, A. Facchetti, T. J. Marks, *Adv. Mater.* 2012, 24, 2242; (b) L. Dou, W.-H. Chang, J. Gao, C.-C. Chen, J. You, Y. Yang, *Adv. Mater.* 2013, 25, 825; (c) J. Ohshita, K. Kimura, K.-H. Lee, A. Kunai, Y.-W. Kwak, E.-C. Son, Y. Kunugi, *J. Polym. Sci., Part A: Polym. Chem.*, 2007, 45, 4588.
- [32] (a) M. D. Perez, C. Borek, S. R. Forrest and M. E. Thompson, *J. Am. Chem. Soc.*, 2009, 131, 9281; (b) J. Liu, Y. Shi and Y. Yang, *Adv. Funct. Mater.*, 2001, 11, 420; (c) D. M. Stevens, J. C. Speros, M. A. Hillmyer, C. Daniel Frisbie, *J. Phys. Chem. C*, 2011, 115, 20806.
- [33] (a) M. M. Wienk, J. M. Kroon, W. J. H. Verhees, J. Knol, J. C. Hummelen, P. A. van Hal, R. A. J. Janssen, *Angew. Chem. Int. Ed.*, 2003, 42, 3371; (b) M. Morana, M. Wegscheider, A. Bonanni, N. Kopidakis, S. Shaheen, M. Scharber, Z. Zhu, D. Waller, R. Gaudiana, C. Brabec, *Adv. Funct. Mater.* 2008, 18, 1757.
- [34] (a) M.-S. Su, C.-Y. Kuo, M.-C. Yuan, U.-S. Jeng, C.-J. Su, K.-H. Wei, *Adv. Mater.* 2011, 23, 3315; (b) F. Zhang, Z. Zhuo, J. Zhang, X. Wang, X. Xu, Z. Wang, Y. Xin, J. Wang, J. Wang, W. Tang, Z. Xu, Y. Wang, *Solar Energy Materials & Solar Cells*, 2012, 97, 71-77.
- [35] (a) X. Liu, S. Huettner, Z. Rong, M. Sommer, R. H. Friend, *Adv. Mater.* 2012, 24, 669-74; (b) J. T. Rogers, K. Schmidt, M. F. Toney, E. J. Kramer, G. C. Bazan, *Adv. Mater.* 2011, 23, 2284; (c) J. K. Lee, W. L. Ma, C. J. Brabec, J. Yuen, J. S. Moon, J. Y. Kim, K. Lee, G. C. Bazan, A. J. Heeger, *J. Am. Chem. Soc.* 2008, 130, 3619.

- [36] Y. Sun, C. J. Takacs, S. R. Cowan, J. H. Seo, X. Gong, A. Roy, Alan J. Heeger, *Adv. Mater.*, 2011, 23, 2226.
- [37] (a) H.-L. Yip, A. K. Y. Jen, *Energy Environ. Sci.*, 2012, 5, 5994.
- [38] M. O. Reese, M. S. White, G. Rumbles, D. S. Ginley, S. E. Shaheen, *Applied Physics Letters*, 2008, 92, 053307.
- [39] (a) J. C. Bijleveld, V. S. Gevaerts, D. Di Nuzzo, M. Turbiez, S. G. J. Mathijssen, D. M. de Leeuw, M. M. Wienk, R. A. J. Janssen, *Adv. Mater.* 2010, 22, E242. (b) N. C. Miller, E. Cho, R. Gysel, C. Risko, V. Coropceanu, C. E. Miller, S. Sweetnam, A. Sellinger, M. Heeney, I. McCulloch, J.-L. Brédas, M. F. Toney, M. D. McGehee, *Adv. Energy Mater.*, 2012, 2, 1208.
- [40] R. S. Becker, J. S. de Melo, A. L. Macüanita, F. Elisei, *J. Phys. Chem.*, 1996, 100, 18683.
- [41] (a) B. Pal, W.-C. Yen, J.-S. Yang, W.-F. Su, *Macromolecules* 2007, 40, 8189; (b) T. Offermans, P. A. van Hal, S. C. J. Meskers, *Physical Review B*, 2005, 72, 045213.
- [42] A. Ruseckas, E. B. Namdas, T. Ganguly, M. Theander, M. Svensson, M. R. Andersson, O. Inganas, V. Sundstrom, *J. Phys. Chem. B*, 2001, 105, 7624-763.
- [43] D. M. Guldi, M. Prato, *Acc. Chem. Res.*, 2000, 33, 695-703
- [44] (a) M. M. Wienk, J. M. Kroon, W. J. H. Verhees, J. Knol, J. C. Hummelen, P. A. van Hal, R. A. J. Janssen, *Angew. Chem., Int. Ed.*, 2003, 42, 3371; (b) X. Gong, M. H. Tong, F. G. Brunetti, J. Seo, Y. M. Sun, D. Moses, F. Wudl, A. J. Heeger, *Adv. Mater.*, 2011, 23, 2272.
- [45] S. V. Chasteen, V. Sholin, S. A. Carter, G. Rumbles, *Solar Energy Materials & Solar Cells*, 2008, 92, 651.
- [46] Y. He, Y. Li, *Phys. Chem. Chem. Phys.*, 2011, 13, 1970.
- [47] S. D. Dimitrov, C. B. Nielsen, S. Shoaee, P. S. Tuladhar, J. Du, I. McCulloch, J. R. Durrant, *J. Phys. Chem. Lett.*, 2012, 3, 140.
- [48] Z. Ma, E. Wang, K. Vandewal, M.R. Andersson, F. Zhang, *Appl. Phys. Lett.* 2011, 99, 143302.
- [49] E. E. Havinga, W. Hove, H. Wynberg, *Polymer Bulletin*, 1992, 29, 119-126.
- [50] Some recent examples are: (a) A. Najari, S. Beaupré, P. Berrouard, Y. Zou, J. -R. Pouliot, C. Lepage-Pàrusse, M. Leclerc, *Adv. Funct. Mater.* 2011, 21, 718; (b) G. Zhang, Y. Fu, Q. Zhang, Z. Xie, *Chem. Commun.* 2010, 46, 4997; (c) C. Piliago, T. W. Holcombe, J. D. Douglas, C. H. Woo, P. M. Beaujuge, J. M. J. Frechet, *J. Am. Chem. Soc.* 2010, 132, 7595; (d) Y. Zhang, S. K. Hau, H. -L. Yip, Y. Sun, O. Acton, A. K. -Y. Jen, *Chem. Mater.* 2010, 22, 2696; (e) Y. Zou, A. Najari, P. Berrouard, S. Beaupré, B. Réda Aich, Y. Tao, M. Leclerc, *J. Am. Chem. Soc.* 2010, 132, 5330; (f) L. Huo, J. Hou, H. -Y. Chen, S. Zhang, Y. Jiang, T. L. Chen, Y. Yang, *Macromolecules* 2009, 42, 6564.
- [51] (a) Y. Liang, Z. Xu, J. Xia, S. -T. Tsai, Y. Wu, G. Li, C. Ray, L. Yu, *Adv. Mater.* 2010, 22, E135; (b) H. -Y. Chen, J. Hou, S. Zhang, Y. Liang, G. Yang, Y. Yang, L. Yu, Y. Wu, G. Li, *Nature Photonics* 2009, 3, 649.
- [52] Some recent examples are: (a) S. K. Lee, J. M. Cho, Y. Goo, W. S. Shin, J. -C. Lee, W. -H. Lee, I. -N. Kang, H. -K. Shim, S. -J. Moon, *Chem. Commun.* 2011, 47, 1791; (b) H. Zhou, L. Yang, S. Liu, W. You, *Macromolecules* 2010, 43, 10390; (c) P. M. Beaujuge, J. Subbiah, K. R. Choudhury, S. Ellinger, T. D. McCarley, F. So, J. R.

Reynolds, *Chem. Mater.* 2010, 22, 2093-2106; (d) M. C. Scharber, M. Koppe, J. Gao, F. Cordella, M. A. Loi, P. Denk, M. Morana, H. -J. Egelhaaf, K. Forberich, G. Dennler, R. Gaudiana, D. Waller, Z. Zhu, X. Shi, C. J. Brabec, *Adv. Mater.* 2010, 22, 367; (e) X. Zhang, T. T. Steckler, R. R. Dasari, S. Ohira, W. J. Potscavage Jr, S. P. Tiwari, S. Coppee, S. Ellinger, S. Barlow, J. -L. Bredas, B. Kippelen, J. R. Reynolds, S. R. Marder, *J. Mater. Chem.* 2010, 20, 123; (f) S. C. Price, A. C. Stuart, W. You, *Macromolecules* 2010, 43, 797.

[53] S. H. Park, A. Roy, S. Beaupre, S. Cho, N. Coates, J. S. Moon, D. Moses, M. Leclerc, K. Lee, A. J. Heeger, *Nature Photonics* 2009, 3, 297.

[54] (a) J. Hou, M. -H. Park, S. Zhang, Y. Yao, L. -M. Chen, J. -H. Li, Y. Yang, *Macromolecules* 2008, 41, 6012; (b) J. Hou, H. -Y. Chen, S. Zhang, Y. Yang, *J. Phys. Chem. C* 2009, 113, 21202; (c) S. C. Price, A. C. Stuart, W. You, *Macromolecules* 2010, 43, 4609.

[55] (a) Y. Fu, H. Cheng, R. L. Elsenbaumer, *Chem. Mater.* 1997, 9, 1720; (b) E. H. Elandaloussi, P. Frère, P. Richomme, J. Orduna, J. Garin, J. Roncali, *J. Am. Chem. Soc.* 1997, 119, 10774.

[56] S.-Y. Jang, B. Lim, B.-K. Yu, J. Kim, K.-J. Baeg, D. Khim, D.-Y. Kim, *J. Mater. Chem.* 2011, 21, 11822.

[57] A. J. Epstein, J. W. Blatchford, Y. Z. Wang, S. W. Jessen, D. D. Gebler, T. L. Gustafson, L. B. Lin, H. -L. Wang, Y. W. Park, T. M. Swager, A. G. MacDiarmid, *Synth. Metals* 1996, 78, 253.

[58] C. Li, M. Liu, N. G. Pschirer, M. Baumgarten, K. Müllen, *Chem. Rev.* 2010, 110, 6817.

[59] G. M. Farinola, F. Babudri, A. Cardone, O. H. Omar, F. Naso, *Pure Appl. Chem.* 2008, 80, 1735.

[60] J. Mei, N. C. Heston, S. V. Vasilyeva, J. R. Reynolds, *Macromolecules* 2009, 42, 1482.

[61] A. Abbotto, E. H. Calderon, M. S. Dangat, F. De Angelis, N. Manfredi, C. M. Mari, C. Marinzi, E. Mosconi, M. Muccini, R. Ruffo, M. Seri, *Macromolecules* 2010, 43, 9698.

[62] A. Abbotto, E. Herrera Calderon, N. Manfredi, C. M. Mari, C. Marinzi, R. Ruffo, *Synth. Metals* 2011, 161, 763-769.

[63] M. J. Frisch et al., *Gaussian 03*, Gaussian, Inc., Wallingford CT, 2004.

[64] M. Cossi, V. Barone, *J. Chem. Phys.* 2001, 115, 4708.

[65] A. J. Moulé, K. Meerholz, *Adv. Funct. Mater.*, 2009, 19, 1.

[66] M. Coakley, M.D. McGehee, *Chem. Mater.*, 2004, 16, 4533.

[67] V. Shrotriya, E. H. Wu, G. Li, Y. Yao, Y. Yang, *Appl. Phys. Lett.*, 2006, 88, 064104.

[68] (a) J. W. Arbogast, C. S. Foote, *J. Am. Chem. Soc.*, 1991, 113, 8886; (b) M. M. Wienk, J. M. Kroon, W. J. H. Verhees, J. Knol, J. C. Hummelen, P. A. Van Hal, R. A. Janssen, *Angew. Chem., Int. Ed.*, 2003, 42, 3371.

[69] Y. He, Y. Li, *Phys. Chem. Chem. Phys.*, 2011, 13, 1970.

[70] (a) S. Loser, C. J. Bruns, H. Miyauchi, R. Ponce Ortiz, A. Facchetti, S. I. Stupp, T. J. Marks, *J. Am. Chem. Soc.*, 2011, 133, 8142; (b) H. L. Gomes, P. Stallinga, F.

Dinelli, M. Murgia, F. Biscarini, D. M. De Leeuw, M. Muccini, K. Mullen, *Polym. Adv. Technol.*, 2005, 16, 227; (c) Z.-X. Xu, V. A. L. Roy, P. Stallinga, M. Muccini, S. Toffanin, H.-F. Xiang, C.-M. Che, *Appl. Phys. Lett.*, 2007, 90, 223509.

[71] J. Kim, S.H. Kim, I.H. Jung, E. Jeong, Y. Xia, S. Cho, I.-W. Hwang, K. Lee, H. Suh, H.-K. Shim, H.Y. Woo, *J. Mater. Chem.*, 2010, 20, 1577.

[72] (a) R. C. Coffin, J. Peet, J. Rogers, G. C. Bazan, *Nature Chem.*, 2009, 1, 657; (b) P. Pingel, A. Zen, R. D. Abellón, F. C. Grozema, L. D. A. Siebbeles, D. Neher, *Adv. Funct. Mater.*, 2010, 20, 2286; (c) M. Tong, S. Cho, J. T. Rogers, K. Schmidt, B. B. Y. Hsu, R D. Moses, C. Coffin, E. J. Kramer, G. C. Bazan, A. J. Heeger, *Adv. Funct. Mater.*, 2010, 20, 3959.

[73] G. F. Burkhard, E. T. Hoke, S. R. Scully, M. D. McGehee, *Nano Letters*, 2009, 9, 4037.

CHAPTER III: CHARGE EXTRACTING (BUFFER) LAYERS

1. INTRODUCTION ON THE ROLE OF BUFFER LAYERS

The steep increase of the overall performance of OPVs registered in the last years has been mainly due to the combination of optimized active layer nanoscale morphology and improved electronic properties of the active materials, mainly of the donor component, as seen in the Chapter II. However, the performance of a BHJ OPV device, and in general of any solar cell, is also affected by the electrodes.

The role of electrodes in solar cells is to efficiently collect and extract charges. In the first chapter it has been explained the importance of having a sufficient energy level alignment between the charge transporting material energy and the charge collecting electrode energy levels, in order to achieve high solar cells efficiencies. Moreover, since in BHJ OPV devices the electrons and holes transporting materials are both in contact with the anode and the cathode, non-geminate recombination of charges due to non-selective charge extraction at the BHJ film/electrode interface should be somehow avoided. To meet both these needs, the structure of BHJ polymer/fullerene solar cells usually includes functional layers interposed between the BHJ active layer and the electrode interfaces, both to favor charge extraction and to enhance the selectivity of the electrodes towards electrons or holes.^[1] These additional layers, called buffer layers, are then essential for achieving maximum performance in polymer solar cells and the usual structures of BHJ solar cells include both an anode buffer layer (ABL) and a cathode buffer layer (CBL).

A number of electrode buffer layers has first been established for organic light-emitting diodes and later on has been transferred to polymer solar cells.^[2] Buffer layers can strongly affect the properties of the organic/electrode interface by inducing interfacial charge redistributions, device polarity modifications, and/or chemical reactions.^[3] Buffer materials are mainly selected on the basis of their energy levels and charge transport properties, but they can also serve as smoothers for an excessive roughness of the substrate,^[4] as barriers for the diffusion of the top electrode through the active layer, and as oxygen and water scavengers. Moreover, in some cases, they can enable better light absorption playing the additional role of optical spacers, enabling a favorable distribution of light into the device.^[5]

Buffer layers are also used for reversing the cell polarity.^[6] In fact glass/ITO is commonly used as the anode, usually in combination with a low-work function metal such as Al. This device polarity is commonly indicated as “standard device configuration” (OPV, **Figure 30a**). For the ITO to be used as cathode, its work function should be tuned towards higher energies, in order to increase its electron affinity, and this is usually achieved by using the appropriate CBL, while a lower energy metal (such as Ag or Au) should be used as metal electrode. The device geometry in which the ITO is used as cathode and the metal electrode as anode is called “inverted device configuration” (i-OPV, **Figure 30b**).

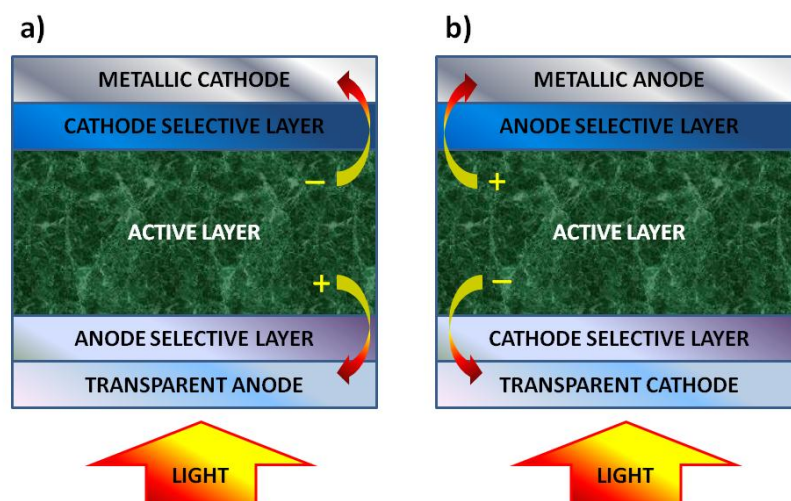


Figure 30 Schematic representation of: (a) a standard configuration solar cell (OPV) and (b) inverted configuration solar cell (i-OPV).

Historically BHJ OPVs have been developed in the normal device configuration, where the ABL is the first layer of the OPV stack to be deposited on the glass/ITO substrate. Since the late 1990s, PEDOT:PSS, has been the most widely used anode buffer layer, in conventional cell architecture (through solvent-treated ABLs), because it shows many favorable properties, such as high electrical conductivity, good transparency in the visible range, good planarization of eventual ITO superficial spikes and, being soluble in water, a good resistance to the organic solvents used for the subsequent deposition of the active layer.^[7] Other organic ABL used in BHJ OPV devices and reported in literature include polymers such as Poly[3,4-(1-hydroxymethyl)ethylenedioxythiophene] (PHEDOT),^[8] doped poly(aniline)s (i.e. a-PANIN),^[9] poly[(9,9-dioctylfluorene)-co-N-(4-(1-methylpropyl)phenyl)diphenylamine] (PFT),^[10] small molecules such as copper phthalocyanines (CuPcs)^[11] and self assembled monolayers.^[12] Some inorganic materials can also be used as ABL: they mainly consist in semiconducting transparent transition metal oxides such as MoO₃, V₂O₅, VO_x, NiO and WO₃.^[13] One of the main disadvantages in using these materials is that they often need to be deposited by evaporation techniques in high temperature/high vacuum conditions to achieve optimal electrical, morphological and optical properties, this limiting their use to high-costs or lab-scale applications. Only recently MoO₃ layers processed from metal-oxide nanoparticle dispersions have been reported in literature.^[14]

In inverted configuration devices the use of PEDOT:PSS as ABL presents some drawbacks, the most important being the high polarity of its dispersion in water, leading to wettability problems associated with the underlying organic active layer. This could render necessary the use of surfactants or additives in the PEDOT:PSS aqueous suspension, which however could decrease the PEDOT:PSS electrical conductivity. For this reason, evaporated ABL such as CuPc or MoO₃, V₂O₅ etc. are often used as ABL in inverted device configuration.

Lithium fluoride (LiF)^[15] and Ca are the most frequently used CBL in conventional solar cells, usually combined with an aluminium electrode. On the other hand, some semiconducting metal oxides are well known in literature for applications as CBL, including TiO₂, TiO_x, ZnO^[16] and Cs₂CO₃.^[17] These CBLs are more often used in inverted device structures, since they often require high temperature treatments after film deposition, processes which are incompatible with the underlying organic active layer in case of normal configuration devices.

In the following sections a study on the influence of different CBL (TiO_x and ZnO) buffer layers on the corresponding devices performances is presented. Particular attention is given to the morphological and electrical characteristics of the studied metal oxide layers used in inverted devices configurations affecting the overall device performances.

2. TiO_x AND ZnO BASED CBL: EFFECTS ON THE CHARGE RECOMBINATION AND EFFICIENCY OF INVERTED DEVICES

As discussed in the introduction, traditionally BHJ OPV devices have been developed in the standard configuration, with the ITO working as the anode and the metal as cathode. Nevertheless, in conventional organic BHJ solar cells the metal cathode must have a low work function (such as Ca or Al), with consequent problems of device stability in air and/or moisture due to the easy oxidation of the low WF metal. Moreover, PEDOT:PSS could degrade the ITO electrode, due to its strong acidity, this also affecting the device stability with time.

On the other hand, inverted device configurations have recently attracted lots of attention due to their increased stability comparing to standard devices. In fact in this configuration the higher WF metal electrode (such as Au and Ag) is more resistant to air and moisture oxidation, thus improving the overall cell stability.^[18]

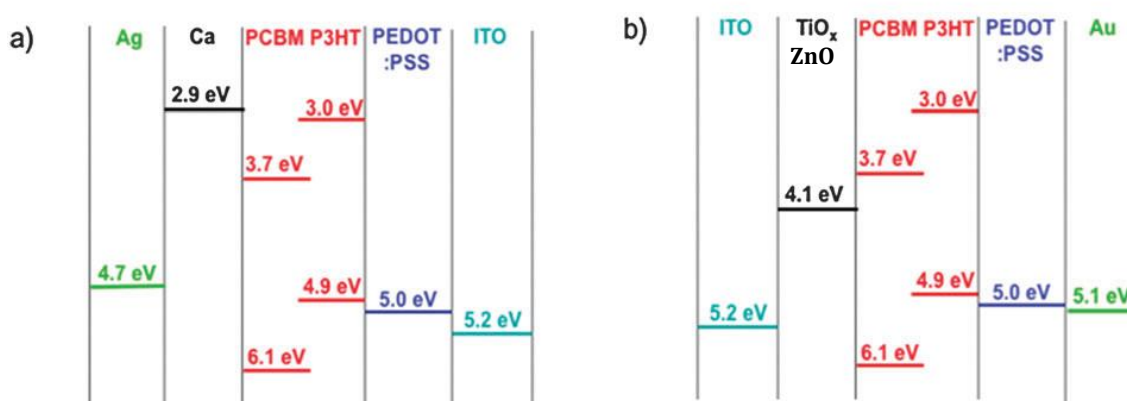


Figure 31 Energy levels with respect to the vacuum diagrams of the materials used in our conventional (a) and inverse (b) solar cells.

Therefore, the advantages or drawbacks of using a standard or inverted configurations have been presented for a series of devices prepared by using a reference blend of P3HT and PC₆₁BM as the active layer. Two different CBL (TiO_x

and ZnO) were used to prepare devices with the inverse configuration, the reference LiF was used as CBL in the standard configuration and PEDOT:PSS was used in all cases as ABL (**Figure 31**).

The difference in efficiency within the cells was measured and correlated to the morphological properties of the CBL and eventually to the morphological changes induced by the bottom buffer layer on the active blend. Moreover, the electrical properties of the devices under working conditions were analyzed through charge extraction and charge recombination experiments, using short and open circuit transient photovoltage measurements. The results have been finally discussed and analyzed in order to explain the influence of the metal oxide selective contact on the overall device efficiency.

2.1. Experimental

Indium tin oxide (ITO, 4 Ohm/sq) covered glass substrates were first cleaned with acetone in order to remove the photo-protective layer. Substrates were then placed in an ultrasonic bath, once in acetone and twice in 2-propanol, each bath lasting 5 min. Finally they were dried at 80 °C for 10 min followed by 20 min of ozone treatment.

In the case of the inverted devices, the metal oxide layers for i-OPVs were prepared with different procedures depending on the material. The TiO_x layer was deposited onto clean ITO substrates by spin coating a solution of commercial Titanium(IV)-butoxide (reagent grade, 97%) diluted in isopropyl alcohol until the desired thickness was reached (around 30 nm). Samples were then dried in the oven at 90 °C for 5 min. The ZnO layer was prepared by spin coating a nanoparticle dispersion prepared according to Pacholski method.^[19] Briefly, 0.11 g of zinc acetate dihydrate was dissolved in 50 ml of methanol under vigorous stirring at 60 °C. Subsequently, a 0.03 M solution of KOH (25 ml) in methanol was added dropwise, at 60 °C, and the reaction mixture was stirred for 2 h at 60 °C. The obtained colloidal suspension, without any further purification treatment, was spin coated at 2000 rpm for 30 s onto the substrate. The thickness of the ZnO layer was estimated to be around 10 nm. The ZnO deposition process was followed by a 5 min air annealing at 150 °C. All the metal oxide layers were treated with oxygen-plasma for 20 minutes just before spin coating.

For the normal configuration devices, PEDOT:PSS (Clevios P VP Al 4083) was deposited onto the ITO substrates by spin coating (5000 rpm, 1 min, resulting thickness around 30 nm) and annealed at 110 °C for 10 min.

For all devices, chlorobenzene (SDSr, analytical grade) solutions of regioregular poly(3-hexylthiophene-2,5-diyl) (P3HT, Rieke Specialty Polymers) and PC₆₁BM, (Nano-Cr) were used. The P3HT:PC₆₁BM solution (19 mg/mL total concentration, P3HT:PC₆₁BM ~ 1:0.9 w/w) was prepared and stirred at 70 °C overnight in inert atmosphere. The active layer was deposited via the automatic doctor blading technique, at a speed of 20 mm/s and a temperature of 70 °C, which lead to

approximately 300 nm thick films. Films were annealed at 150 °C for 20 minutes in inert atmosphere.

For the inverted devices, the PEDOT:PSS working as ABL (Clevios P VP Al 4083) was spin coated over the active layer (2000 rpm, 1 min, resulting thickness of about 30 nm), after the addition of a suitable surfactant (Zonyl FS300 from Baytron, 1 wt %) to improve the active layer wettability and annealed at 110 °C for 10 min. The metal contact (100 nm of Au) was deposited on PEDOT:PSS by high vacuum thermal deposition at a pressure of around $1 \cdot 10^{-6}$ mbar.

For normal devices, the top electrode was composed of 10 nm of Ca (as CBL) and 100 nm of Ag by high vacuum thermal deposition at a pressure of around $1 \cdot 10^{-6}$ mbar.

Evaporation through a shadow mask led to devices with 9 mm² active area.

The I-V measurements were carried out with an ABET 150 W Xe lamp equipped with an adequate set of filters to achieve a solar spectrum of AM 1.5G (intensity 100 mW·cm⁻²), a Keithley model 2600 digital source meter and homebuilt Labview software.

The transient photovoltage measurements (TPV) were done with a system schematized in **Figure 32**.

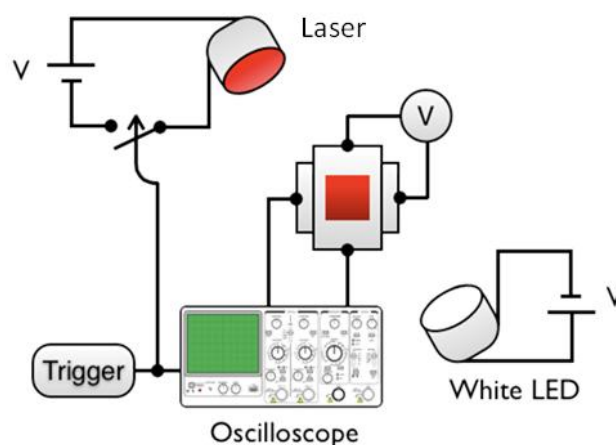


Figure 32 Schematic representation of the TPV experimental setup.

The devices were directly connected to an oscilloscope (Tektronix TDS2022, 1 MO) and illuminated with a ring of white Luxeon Lumileds white LEDs. A small perturbation (~ 2 mV) was applied through a light pulse (N₂ laser excitation through a Coumarine 153 dye solution produced 550 nm emission with ~ 50 ns pulses) and the corresponding voltage drop was measured. The charges recombination rate (k_R) was calculated for illumination intensities ranging from 0.1 sun to 1 sun. The V_{oc} of the device before laser perturbation under that light illumination intensity was measured by a simple voltmeter.

Charge Extraction (CE) measurements were performed with a setup schematized in **Figure 33**.

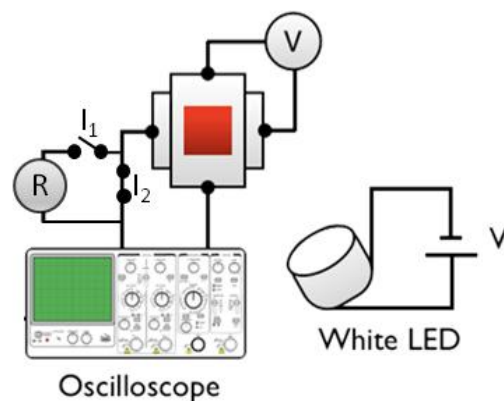


Figure 33 Schematic representation of the CE experimental setup.

The devices were held in an open circuit equilibrium through illumination with white light (white Luxeon Lumileds LEDs). Then the light was switched off and the circuit contemporarily closed (switch I_2 open and switch I_1 close), while the charges were forced to pass through a resistor (R , with resistance ~ 50 Ohm) (**Figure 33**). The time-dependent variation of the potential through R is due to the device discharge and the recombination losses are sufficiently low to be negligible.^[20] Integrating the voltage decay over time at a specific light bias allows to calculate the excess concentration of charge accumulated in the device in the working conditions specified.

2.2. Results and discussion

2.2.1. Metal oxide thin film morphology

The scanning electron microscopy (SEM) topographic images of the ZnO and TiO_x layers deposited on ITO have been registered and are reported in **Figure 34**.

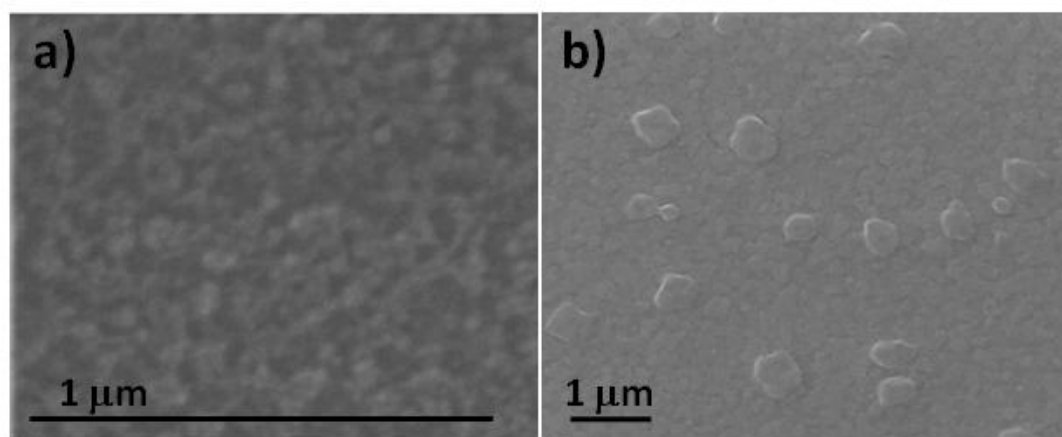


Figure 34 SEM images of the ZnO (**a**) and TiO_x (**b**) layers on ITO.

It can be seen that the ZnO layer consists of a homogeneous distribution of nanoparticles with a diameter of some tens of nanometers, while the TiO_x layer

consists in a compact coating of small (sub-micrometric) nanoparticles with some overlying isolated bigger (micrometric) aggregates.

On the other hand, PEDOT:PSS films prepared by spin coating are known to be very smooth (RMS \sim 1.5 nm) and homogeneous.^[21]

It should be stressed that the different morphologies of the bottom buffer layer could reasonably influence the crystallinity, morphology and homogeneity of the overlying P3HT:PC₆₁BM film, thus influencing some of the overall photovoltaic parameters of the corresponding device.

2.2.1. Devices photovoltaic characterization

The working parameters, under standard light irradiation conditions, are reported for all the studied standard and inverted configuration devices in **Table 7**.

Table 7 Photovoltaic parameters of the studied i-OPVs and OPVs.

Cell	V _{oc} (V)	J _{sc} (mA/cm ²)	FF (%)	PCE (%)
OPV ABL = PEDOT:PSS CBL = Ca	0.60	9.67	56	3.28
i-OPV CBL = ZnO ABL = PEDOT:PSS	0.60	8.91	57	3.09
i-OPV CBL = TiO _x ABL = PEDOT:PSS	0.55	9.06	52	2.61

The devices consisted of the same photoactive P3HT:PCBM organic layer prepared and treated in all cases with the same procedures. On the other hand, since different contact architectures were used, the observed differences in the I-V curve characteristics could be ascribed to the effects of the selective contacts used. The best device efficiency has been obtained for the normal configuration device, having PEDOT:PSS as ABL and Ca as CBL.

Both i-OPVs present a slightly lower J_{sc}. This could be due to: i) a lower thickness of the active layer due to a lower affinity of the P3HT:PC₆₁BM with the metal oxide underlying layer during spin coating deposition; ii) a lower transmittance of the semi-transparent glass/ITO/metal oxide electrode, comparing to the glass/ITO/PEDOT:PSS one; iii) a lower reflectivity of the top PEDOT:PSS/Au contact comparing to the Ca/Ag one, decreasing the back-reflected light towards the active layer, which also contributes to photocurrent generation during device functioning; iv) a higher R_s of the metal oxide/ITO cathode comparing to the Ca/Ag one. The J_{sc} difference between ZnO-based i-OPV comparing to the reference OPV is

the reason for the inferior performances of the former device with respect to the latter. Nevertheless, the differences in J_{sc} are not the mayor factor influencing the overall devices performances.

Regarding FF, the greatest difference is found between the TiO_x based i-OPV device and the other two: only a FF of 52% is measured for the former device, comparing to 56-57% of the other two devices. This decrease could be maybe ascribed to the different morphology of the active layer blend induced by the different polarity, roughness and homogeneity of the underlying substrates. Indeed, the inhomogeneity of the TiO_x surface comparing to the ZnO or the PEDOT:PSS ones, demonstrated by SEM analysis, seem to support this hypothesis.

Finally, the most striking photovoltaic parameter variations measured for this family of devices is their V_{oc} , which is 0.60 V for both the standard OPV and the ZnO-based i-OPV (within 4 mV of difference), while is 0.55 V (~ 50 mV lower) for the TiO_x -based i-OPV.

The V_{oc} in OPV devices is found to be proportional to the difference between the donor HOMO and the acceptor LUMO.^[22] This also means that in this type of solar cell, the V_{oc} could be limited by the distribution of the tail states of the HOMO and LUMO levels and by the recombination processes that could occur at the donor/acceptor interface between electrons in the acceptor LUMO and holes in the donor HOMO.

Therefore, to gain a deeper understanding of the influence of the different metal oxide layers on the recombination processes at the D/A interface and on the charge distribution in the HOMO and LUMO states of the donor and the acceptor, comparative studies with the Transient Photovoltage and the Charge Extraction techniques were performed.

2.2.2. Charge recombination dynamics

CE is a technique used to calculate the amount of charges accumulated in a device under light illumination in open circuit. This condition is a dynamic equilibrium between charge photogeneration and charge recombination processes. A white light pulse, long enough to achieve equilibrium, has to be applied to accumulate charges in the device, which is held under open circuit. Once the light is switched off, the device is contemporarily switched to short circuit and the accumulated charges allowed to travel through a resistance ($R \sim 30$ Ohms) where the cell potential decay is measured. The described trends of light and cell voltage are reported in a graph over time in **Figure 35 (a)**, while an example of the voltage decay obtained with this measure, when the cell is switched to short circuit and the light is switched off, is reported in **Figure 35 (b)**.

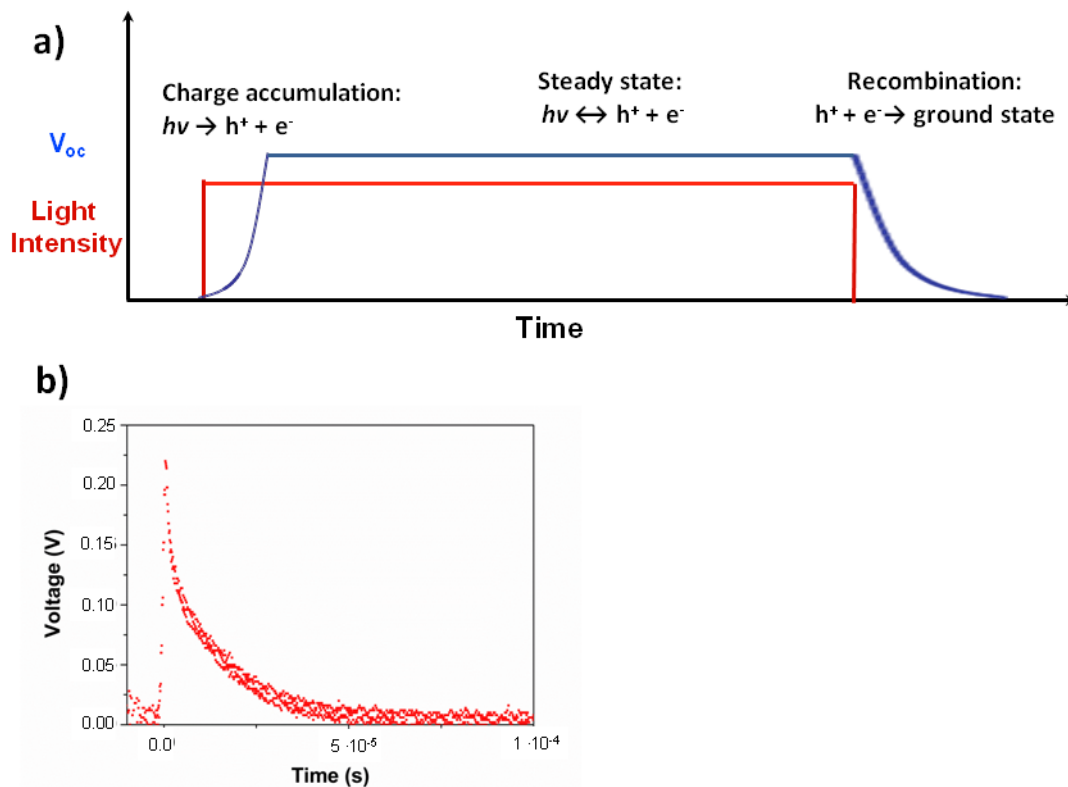


Figure 35 a) Trends of the light intensity (red line) and of the voltage of the cell (blue line) over time in the CE experiment. **b)** Example of the voltage drop across the resistance R during CE measurement.

The decay of the potential with time varies with the device discharge process, including charge recombination kinetics. Therefore, at different light intensities, different discharge transients are recorded. By dividing the transient voltage ($V(t)$) measured through the resistance by R and integrating the so obtained current transient ($I(t)$) over time, the charges extracted from the device after illumination (Q) can be calculated, as in **Equation 16**:

$$Q = \int \frac{V(t)}{R} dt = \int I(t) dt \quad \text{Eq. 16}$$

Therefore, the density of charges (n) accumulated in the device at that light intensity and in open-circuit, is calculated as the ratio between Q and the elementary charge (q), divided by the volume of the charge-accumulating layers of the device (Vol), as in **Equation 17**:

$$n = \frac{Q}{q \cdot \text{Vol}} \quad \text{Eq. 17}$$

Finally, the density of charges n can be calculated for different light intensities, corresponding to different light-biases (light induced V_{oc}).

n was then calculated with CE experiments for all devices, considering the P3HT:PC₆₁BM layer, the TiO_x/P3HT:PCBM and ZnO/P3HT:PC₆₁BM layers as the main capacitors in the standard OPV, in the TiO_x-based i-OPSC and in the ZnO-based i-OPV respectively. **Figure 36** shows the charge densities n , accumulated in the devices at different V_{oc} , obtained under increasingly higher applied light biases (E).

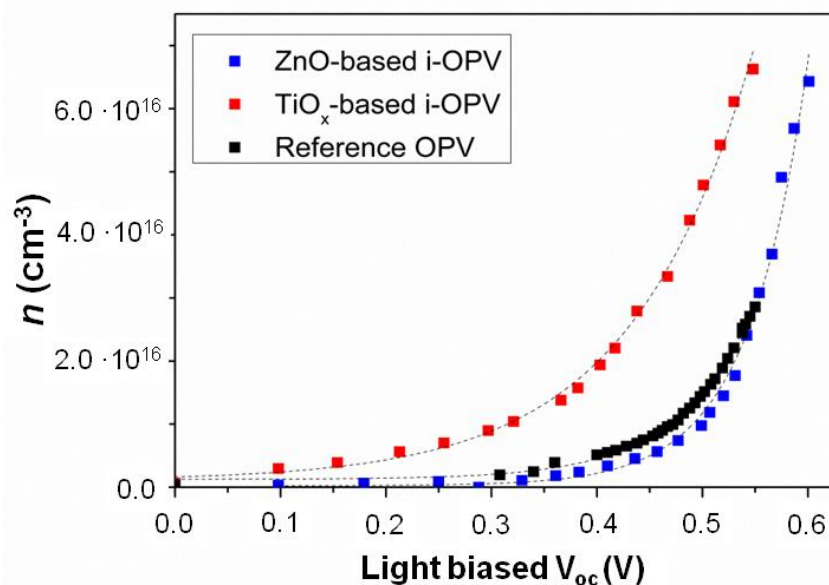


Figure 36 Charge density n accumulated in the ZnO-based i-OPV (blue), TiO_x-based i-OPV (red) and standard OPV (black) devices *versus* the applied light induced equilibrium V_{oc} (E).

A different trend emerges for the devices: in particular, the TiO_x-based device present a higher charge density (charge accumulation) comparing the ZnO-based and the standard devices, for the same light bias (E). In other words, for the same charge density accumulated in the device, different V_{oc} are measured for the different devices. For example, for the TiO_x-based i-OPV at 1 sun illumination, a light bias shift towards lower voltages (~ 50 mV) can be observed. This is in perfect agreement with the V_{oc} values obtained for the studied devices during the I-V curves measurement.

The charge accumulation in BHJ OPVs is usually described by a density of states (DOS) with a Gaussian distribution. For example, the capacitance C of BHJ OPV devices, which is directly indicative of the device charge accumulation and proportional to charge density, can be measured with impedance experiments. Then, the C distribution over energy represents the DOS of the organic semiconductor blend, and can then be fitted to a Gaussian curve having the following expression (**Equation 18**):^[23]

$$C(E) = \frac{N}{\sigma\sqrt{2\pi}} \left(\exp\left(-\frac{(E-E_0)^2}{2\sigma^2}\right) \right) \quad \text{Eq. 18}$$

where E is the potential, N is the maximum limit of charge density per volume unit, E_0 is the potential at maximum capacitance which is related to the theoretical

maximum V_{oc} of the device and σ , correlated with the curvature of the DOS curve, represents the dispersion degree of the DOS of the organic semiconductor blend.

Since capacitance can be related to the total charge density n using **Equation 19**:

$$n(E) = \int C(E) dE \quad \text{Eq. 19}$$

by combining **Equation 18** with **Equation 19** it can be obtained **Equation 20**:

$$n(E) = \frac{N}{2} \left(\operatorname{erf} \left(\frac{E-E_0}{\sigma\sqrt{2}} \right) + 1 \right) \quad \text{Eq. 20}$$

Therefore, by fitting the experimental n vs. E data, obtained in the CE experiment, with **Equation 20**, an estimation of N and σ can be obtained. In this case, the maximum of the DOS distribution, E_0 , relatively to this donor-acceptor couple, is considered to lie at the energetic onset (E_{CT}) of the charge transfer state arising from the ground and excited state interactions between P3HT and PCBM, as recently reported in literature.^[24]

The experimental n values versus light-induced bias (E), fitted with **Equation 20**, gave the fitting parameters reported in **Table 8**.

Table 8 Approximated fitting parameters (N and σ) of experimental n versus E data with Equation 20.

CELL	n (cm ⁻³)	σ (eV)
TiO _x -based i-OPV	$2 \cdot 10^{18}$	0.30
Standard OPV	$3 \cdot 10^{18}$	0.23
ZnO-based i-OPV	$4 \cdot 10^{18}$	0.23

It can be seen that the fits are in agreement with the experimental data if the DOS is assumed to be centered at $E_0 = E_{CT} = 1.1$ eV.^[24b] From the fitting we can also extrapolate the theoretical maximum density of the charge (N) that can be accumulated by the studied devices, corresponding to approximated values lying between 2 and $4 \cdot 10^{18}$ cm⁻³ for all devices. As it can be seen, the range of charge densities and light biased V_{oc} that can be investigated with the CE technique is limited comparing to the the theoretical maximum values of N and E_0 expected from **Equation 20**. Therefore, the extrapolated N and σ values should be considered as approximated values.

The extrapolated N are in all cases two orders of magnitude larger than the measured n at 1 sun of light bias (100 mW cm⁻²). This discrepancy is due to the limit imposed by the bimolecular charge recombination processes, which increase with increasing light intensities and hamper the Fermi level of the electron

acceptor from reaching the LUMO energy and the Fermi level at the electron donor from reaching the HOMO level.

On the other hand, different σ values resulted from the three devices: a σ of ~ 0.23 eV was found for the standard OPV and for the ZnO-based i-OPV, while a slightly higher σ of 0.30 eV was found for TiO_x based i-OPV. Since σ is representative of the disorder of the DOS distribution centered at E_0 , as defined above, this result indicates a broadening of the DOS distribution for the TiO_x-based inverted device, comparing to the other two. This broadening can be attributed to the presence of the TiO_x layer, that either: (a) provides, in addition to the energetic states determined by P3HT and PCBM, additional trap states that can be filled by free charge carriers during the device performance, or (b) influences the morphology of the overlying organic layer and therefore its DOS distribution, or (c) both. However, this DOS broadening could be the factor responsible for the lower V_{oc} measured in the TiO_x-based i-OPV, comparing to the reference and the ZnO-based i-OPV devices.

To get insight into the interfacial charge recombination processes occurring within the active layer, which are also known to limit the V_{oc} in BHJ OPV devices under operating conditions, TPV experiments were performed. The TPV technique has been previously applied to the study of OPVs to analyze the relationship between the charge density, the DOS distribution and the charge recombination kinetics in the organic photoactive layer.^[25]

In the TPV experiments, the device is held in open circuit conditions, so the just-generated charges recombine to return to the previous equilibrium status with a kinetic that is proper of that open-circuit equilibrium state. The obtained data therefore permit: i) the study of the dependence of the recombination with the amount of charge, and thus, with the potential; ii) compare the recombination constants of different devices.

The device is illuminated with white light to reach equilibrium. Then, the system is perturbed with a light pulse, usually with a laser at a wavelength matching the absorption of the active layer. This pulse perturbs the device open-circuit potential and the decay of V_{oc} after the perturbation is measured. The variation of white light intensity allows the measurement of different decays, depending on the amount of charges accumulated in the device. The observed drop in voltage at each light bias was fitted with an exponential decay as in **Equation 21**:

$$V = V_0 \exp (-t/\tau) \quad \text{(Eq. 21)}$$

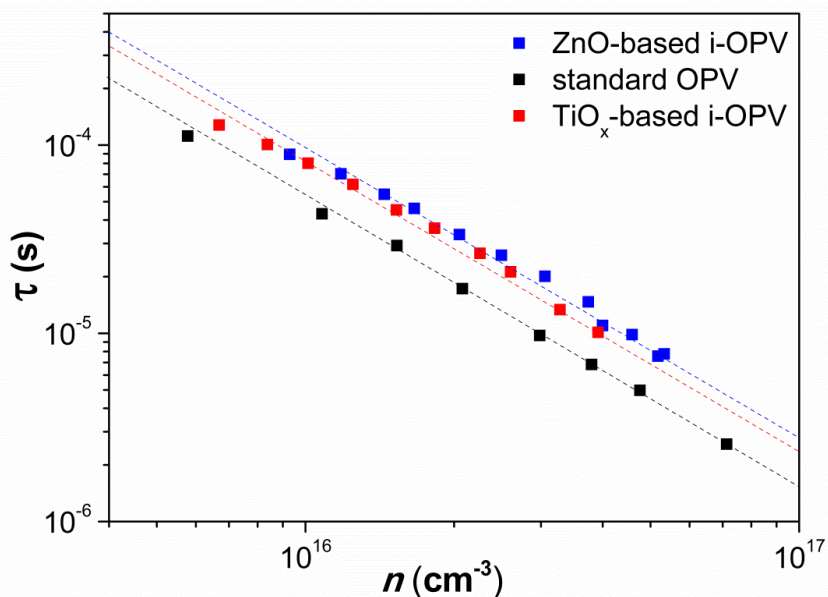


Figure 37 Charges recombination lifetimes (τ) extracted from the TPV experiment fitted towards the n values, extracted from the CE experiment, at the corresponding light biases.

Since the rate of the recombination process is strongly dependent on n , the extracted lifetimes (τ) at each light bias were plotted against the charge density (n) corresponding to the same light bias, and reported in **Figure 37** on a log-log plot. For the three studied devices, the τ versus n plots resulted in equivalent trends, in particular they all showed a pseudo-first order exponential behaviour. As previously found in literature, these trends are indicative of the bimolecular recombination process occurring within the organic layer.^[26] Therefore, for the OPV and i-OPV devices (both TiO_x - and ZnO-based ones), despite the difference in the nature of the selective contacts, the analyzed charge recombination kinetics can be associated only to the bimolecular recombination process occurring between holes in the P3HT phase and electrons in the PC_{61}BM phase. Therefore, additional charge recombination processes occurring in the TiO_x -based i-OPV device and involving the charge accumulated at the TiO_x /active layer interface, or in the bulk TiO_x layer, can be excluded or considered negligible.

Taking into account these considerations, the lower V_{oc} registered for the TiO_x -based i-OPV device compared to the ZnO-based i-OPV and the reference OPV can be reasonably explained on the basis of their different DOS distributions, as shown in **Figure 38**.

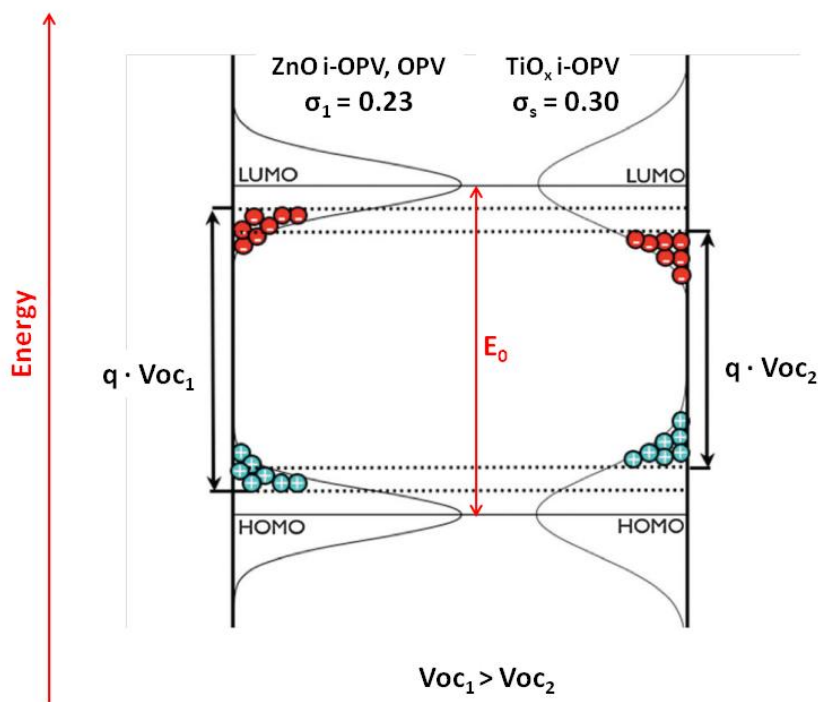


Figure 38 DOS distributions of HOMO and LUMO levels with different disorders ($\sigma_1 = 0.23$ and $\sigma_2 = 0.30$) determining different energy gaps ($q \cdot V_{oc1}$ and $q \cdot V_{oc2}$) and V_{oc} (V_{oc1} and V_{oc2}).

In fact, even though the HOMO and LUMO levels involved in the charge separation (and recombination) processes are centered at the same energy levels and their maxima are separated by the theoretical maximum energy gap E_0 , their DOS around the maxima are differently distributed. The filling of the HOMO and LUMO levels with a broader DOS distribution ($\sigma_2 = 0.30$) then leads to a lower effective energy gap (indicated in the figure as $q \cdot V_{oc2}$) while the filling of the HOMO and LUMO levels with a narrower DOS distribution ($\sigma_1 = 0.23$) leads to a higher effective energy gap ($q \cdot V_{oc1}$). Therefore, for the same charge density, while the recombination kinetic remains the same for all devices (as revealed by the TPV experiment), the broader DOS distribution of the TiO_x -based i-OPV device is the main factor leading to a lower V_{oc} comparing to the standard OPV and to the ZnO-based i-OPV, which in turns both show a narrower DOS (as shown by the CE experiment).

3. CONCLUSIONS

In this work a series of efficient inverse i-OPVs and standard OPVs with P3HT:PC₆₁BM based solar cells were prepared. The best efficiency was found for the device with the standard architecture. Slightly lower efficiency was found for i-OPV device with ZnO as CBL comparing to the standard one, mainly due to a lower I_{sc} probably due to optical losses. On the other hand, slightly lower efficiency was measured for TiO_x -based i-OPVs due to lower V_{oc} , compared to the ZnO-based i-OPV and to the standard device. The analysis of the charge density distribution in the devices under working conditions under different light biases revealed a

difference in the DOS distribution of the TiO_x -based i-OPV, comparing to the ZnO-based i-OPV and the standard devices. Transient photovoltage measurements in open-circuit conditions at different light biases showed that the charge recombination kinetics are comparable for the three different devices. The recombination kinetics were found to be dependent on the charge density through the same exponential function, characteristic of a bimolecular recombination process occurring within the organic layer. Taking into account these considerations, the decreased V_{oc} of the TiO_x -based i-OPV device, leading to its inferior performances, was explained by its different DOS distribution rather than to increased charge recombination kinetics. This different DOS distribution, both of the HOMO and LUMO states, is indeed induced by the TiO_x metal oxide layer on the active layer blend through morphological and/or electrical changes. The results and discussions provided in this work open new insights for further investigations on i-OPVs. For instance, new metal oxides with reduced trap-densities and/or more uniform film surfaces, leading to narrower DOS distributions, could be employed in i-OPV devices, paving the way towards higher V_{oc} and efficient i-OPVs.

4. BIBLIOGRAPHY

- [1] (a) H. Ishii, K. Sugiyama, E. Ito, K. Seki, *Adv. Mater.*, 11, 8, 1999, 605; (b) R. Steim, F. R. Kogler, C. J. Brabec, *J. Mater. Chem.*, 20, 2010, 2499.
- [2] (a) J. Meyer, S. Hamwi, M. Kroeger, W. Kowalsky, T. Riedl, A. Kahn, *Adv. Mater.*, 2012, 24, 5408; (b) J. H. Park, T.-W. Lee, B.-D. Chin, D. H. Wang, O. O. Park, *Macromol. Rapid Commun.*, 2010, 31, 2095; (c) M. S. Liu, Y.-H. Niu, J. Luo, B. Chen, T.-D. Kim, J. Bardecker, A. K.-Y. Jen, *J. of Macromol. Sci., Part C: Polym. Rev.*, 2006, 46, 7.
- [3] S.-S. Sun, L. R. Dalton, *Introduction to organic electronic and optoelectronic materials and devices*, 2008, CRC press Taylor and Francis group.
- [4] F.Z. Dahoua, L. Cattin, J. Garnier, J. Ouerfellid, M. Morslie, G. Louarn, A. Bouteville, A. Khellil, J.C. Bernède, *Thin Solid Films*, 2010, 518, 6117.
- [5] J. K. Lee, N. E. Coates, S. Cho, N. S. Cho, D. Moses, G. C. Bazan, K. Lee, A. J. Heeger, *Appl. Phys. Lett.*, 2008, 92, 243308.
- [6] H. Ma, H.-L. Yip, F. Huang and A. K.-Y. Jen, *Adv. Funct. Mater.*, 2010, 20, 1371.
- [7] A. Elschner, S. Kirchmeyer, W. Lovenich, U. Merker, K. Reuter, *PEDOT: Principles and applications of an intrinsically conductive polymer*, 2011, CRC press, Taylor and Francis group.
- [8] S. Roquet, P. Leriche, I. Perepichka, B. Jusselme, E. Levillain, P. Frère, J. Roncali, *J. Mater. Chem.*, 2004, 14, 1396.
- [9] (a) M.-Y. Chang, C.-S. Wu, Y.-F. Chen, B.-Z. Hsieh, W.-Y. Huang, K.-S. Ho, T.-H. Hsieh, Y.-K. Han, *Org. Electron.*, 2008, 9, 1136; (b) Y.-K. Han, Y.-J. Lee, P.-C. Huang, *J. Electrochem. Soc.*, 2009, 156, K37.
- [10] J. Park, S.-H. Han, S. Senthilarasu, S.-H. Lee, *Sol. Energy Mater. Sol. Cells*, 2007, 91, 751.
- [11] N. Wang, J. Yu, Y. Zang, J. Huang, Y. Jiang, *Sol. Energy Mater. Sol. Cells*, 2010, 94, 263.
- [12] (a) S. Khodabakhsh, B. M. Sanderson, J. Nelson, T. S. Jones, *Adv. Funct. Mater.*, 2006, 16, 95; (b) B. de Boer, A. Hadipour, M. M. Mandoc, T. van Woudenberg, P. W. M. Blom, *Adv. Mater.*, 2005, 17, 621; (c) G. Heimel, L. Romaner, E. Zojer, J. L. Bredas, *Acc. Chem. Res.*, 2008, 41, 721; (d) J. S. Kim, J. H. Park, J. H. Lee, J. Jo, D.-Y. Kim, K. Cho, *Appl. Phys. Lett.*, 2007, 91, 112111.
- [13] (a) V. Shrotriya, G. Li, Y. Yao, C.-W. Chu, Y. Yang, *Appl. Phys. Lett.*, 2006, 88, 073508; (b) J. Meyer, S. Hamwi, M. Kröger, W. Kowalsky, T. Riedl, A. Kahn, *Adv. Mater.*, 2012, 24, 5408.
- [14] S. Murase, Y. Yang, *Adv. Mater.*, 2012, 24, 2459.
- [15] (a) S. E. Shaheen, C. J. Brabec, N. S. Sariciftci, F. Padinger, T. Fromherz, J. C. Hummelen, *Appl. Phys. Lett.*, 2001, 78, 841; (b) C. J. Brabec, S. E. Shaheen, C. Winder, N. S. Sariciftci, P. Denk, *Appl. Phys. Lett.*, 2002, 80, 1288.
- [16] (a) C. Waldauf, M. Morana, P. Denk, P. Schilinsky, K. Coakley, S. A. Choulis, C. J. Brabec, *Appl. Phys. Lett.*, 2006, 89, 233517; (b) J. Y. Kim, S. H. Kim, H. H. Lee, K. Lee, W. Ma, X. Gong, A. J. Heeger, *Adv. Mater.*, 2006, 18, 572; (c) S.

H. Kim, S. H. Park, K. Lee, *Curr. Appl. Phys.*, 2010, 10, S528; (d) A. Hayakawa, O. Yoshikawa, T. Fujieda, K. Uehara, S. Yoshikawa, *Appl. Phys. Lett.*, 2007, 90, 163517; (e) K. Lee, J. Y. Kim, S. H. Park, S. H. Kim, S. Cho, A. J. Heeger, *Adv. Mater.*, 2007, 19, 2445; (f) B. Y. Yu, A. Tsai, S. P. Tsai, K. T. Wong, Y. Yang, C.-W. Chu, J.-J. Shyue, *Nanotechnology*, 2008, 19, 255202; (g) M. S. White, D. C. Olson, S. E. Shaheen, N. Kopidakis, D. S. Ginley, *Appl. Phys. Lett.*, 2006, 89, 143517; (h) K. Takanezawa, K. Hirota, Q.-S. Wei, K. Tajima, K. Hashimoto, *J. Phys. Chem. C*, 2007, 111, 7218; (i) G. Li, V. Shrotriya, J. S. Huang, Y. Yao, T. Moriarty, K. Emery, Y. Yang, *Nat. Mater.*, 2005, 4, 864; (l) A. R. Campbell, J. M. Hodgkiss, S. Westenhoff, I. A. Howard, R. A. Marsh, C. R. McNeill, R. H. Friend, N. C. Greenham, *Nano Lett.*, 2008, 8, 3942; (m) S. K. Hau, H.-L. Yip, N. S. Baek, J. Zou, K. O'Malley, A. K.-Y. Jen, *Appl. Phys. Lett.*, 2008, 92, 253301; (n) J.-C. Wang, W.-T. Weng, M.-Y. Tsai, M.-K. Lee, S.-F. Horng, T.-P. Perng, C.-C. Kei, C.-C. Yu, H.-F. Meng, *J. Mater. Chem.*, 2010, 20, 862.

[17] (a) G. Li, C. W. Chu, V. Shrotriya, J. Huang, Y. Yang, *Appl. Phys. Lett.*, 2006, 88, 253503; (b) H.-H. Liao, L.-M. Chen, Z. Xu, G. Li, Y. Yang, *Appl. Phys. Lett.*, 2008, 92, 173303; (c) F.-C. Chen, J.-L. Wu, S. S. Yang, K.-H. Hsieh, W.-C. Chen, *J. Appl. Phys.*, 2008, 103, 103721.

[18] (a) T. Kuwabara, T. Nakayama, K. Uozumi, T. Yamaguchi, K. Takahashi, *Sol. En. Mater. Sol. Cells*, 2008, 92, 1476; (b) B. Zimmermann, U. Wurfel, M. Niggemann, *Sol. En. Mater. Sol. Cells*, 2009, 93, 491; (c) R. Steim, S. A. Choulis, P. Schilinsky, C. J. Brabec, *Appl. Phys. Lett.*, 2008, 92, 093303; (d) T. Kuwabara, H. Sugiyama, T. Yamaguchi, K. Takahashi, *Thin Solid Films*, 2009, 517, 3766; (e) C. S. Kim, S. S. Lee, E. D. Gomez, J. B. Kim, Y.-L. Loo, *Appl. Phys. Lett.*, 2009, 94, 113302; (f) H. Schmidt, K. Zilberberg, S. Schmale, H. Flugge, T. Riedl, W. Kowalsky, *Appl. Phys. Lett.*, 2010, 96, 243305;

[19] C. Pacholski, A. Kornowski, H. Weller, *Angew. Chem. Int. Ed.*, 2002 41, 1188.

[20] C. G. Shuttle, B. O' Regan, A. M. Ballantyne, J. Nelson, D. D. C. Bradley, J. R. Durrant, *Phys. Rev. B*, 2008, 78.

[21] J. Huang, P. F. Miller, J. C. de Mello, A. J. de Mello, D. D. C. Bradley, *Synth. Metals*, 2003, 139, 569.

[22] (a) Scharber, M. C. et al., *Adv. Mater.*, 2006, 18, 789; (b) D. Veldman, S. C. J. Meskers, R. A. J. Janssen, *Adv. Funct. Mater.*, 2009, 19, 1939; (c) W. Shockley, H. Queisser, *J. Appl. Phys.*, 1961, 32, 510; (d) A. Gadisa, M. Svensson, M. R. Andersson, O. Inganäs, *Appl. Phys. Lett.*, 2004. 84, 1609; (e) J. Nelson, J. Kirkpatrick, P. Ravirajan, *Phys. Rev. B*, 2004, 69, 035337; (f) B. P. Rand, D. P. Burk, S. R. Forrest, *Phys. Rev. B* 2007, 75, 115327; (g) W. J. Potscavage, S. Yoo, B. Kippelen, *Appl. Phys. Lett.*, 2008, 93, 193308; (h) T. Kirchartz, J. Mattheis, U. Rau, *Phys. Rev. B*, 2008, 78, 235320; (i) J. J. Benson-Smith, et al., *Adv. Funct. Mater.*, 2007, 17, 451.

[23] (a) G. Garcia-Belmonte, P. P. Boix, J. Bisquert, M. Sessolo, H. J. Bolink, *Sol. Energy Mater. Sol. Cells*, 2010, 94, 366-375; (b) J. Bisquert, F. Fabregat-Santiago, Mora-Serò, G. Garcia- Belmonte, E. M. Barea, E. Palomares, *Inorg. Chim. Acta*, 2008, 361, 684.

[24] (a) K. Tvingstedt, K. Vandewal, A. Gadisa, F. Zhang, J. Manca, O. Inganas, *J. Am. Chem. Soc.*, 2009, 131, 11819; (b) K. Vandewal, A. Gadisa, W. D. Oosterbaan, S. Bertho, F. Banishoeib, I. Van Severen, L. Lutsen, T. J. Cleij, D. Vanderzande, J. V. Manca, *Adv. Funct. Mater.*, 2008, 18, 2064.

[25] A. Sanchez-Diaz, M. Izquierdo, S. Filippone, N. Martin, E. Palomares, *Adv. Funct. Mater.*, 2010, 20, 2695.

[26] C. G. Shuttle, B. O'Regan, A. M. Ballantyne, J. Nelson, D. D. C. Bradley, J. De Mello, J. R. Durrant, *Appl. Phys. Lett.*, 2008, 92, 093311.

CHAPTER IV: LIGHT MANAGING TECHNIQUES IN OPV

It has been shown that through an accurate engineering of the photoactive materials, of the processing conditions, of the buffer layers and of the architecture of OPV devices, important improvements in devices efficiency can be achieved. Nevertheless, the main limiting factor for the OPV cells performances is the difficulty to maximize the EQE, because of the organic active layer thickness limitations. This is mainly due to the mismatch between the common light absorption depth (hundreds of nanometers) and the exciton diffusion length (tens of nanometers) through the contorted BHJ morphology of the photoactive film, which remains the bottleneck that limits the maximum thickness of the active layer.^[1]

This limit could be overcome by employing light managing techniques able to concentrate, trap or tune the light inside the device, in order to enhance the flux of photons absorbed by the active layer.

1. DIFFERENT APPROACHES FOR LIGHT MANAGING IN OPV

Light managing techniques for optoelectronic devices such as solar cells span from collector mirrors,^[2] fiber based and micro lenses,^[3] light concentrators,^[4] luminescent concentrators,^[5] anti-reflection coatings^[6] and surface plasmon resonators.^[7]

Collector mirrors and concentrating lenses collect the light hitting a certain area and by simply exploiting the physical principles of reflection (mirrors) or refraction (lenses) on curved surfaces, focusing that light onto a smaller area where the solar cell is installed. Therefore, the radiation power density incident on the solar cell results increased and contemporarily the surface coverage of the device can be reduced, with significant materials costs reduction. However, the main limit of this technology is that it usually exploits bulky structures in addition to the normal solar cells or panels, thus rendering more complicated the overall device line production.

Luminescent concentrators are a particular class of equipments through which sunlight is both concentrated and wavelength-tuned. In detail, the incident light, before reaching the active layer, passes through the luminescent concentrator layer, formed by a matrix in which luminescent molecules (which could be organic dyes, inorganic phosphors, or quantum dots, etc..) are dispersed. The role of these molecules is to absorb light which would not be absorbed by the active layer and re-emit it at a longer wavelength, in the range of the absorption spectrum of the active layer.

Anti reflective coatings are beneficial for OPV cells due to the inherent strong reflection from the glass substrates on which devices are usually prepared. Moreover, the various dielectric layers (including the substrate, the photoactive layer, and the buffer layers) included in OPV devices trigger a considerable amount of reflection at interfaces leading to optical losses. Therefore, nanostructured

materials or high-refraction index materials or other strategies able to minimize these losses have been suggested, including “moth-eye” structures,^[8] self-assembled monolayers of nano-silica spheres,^[9] one-dimensional periodically micro-structured lens surfaces,^[10] and hierarchically patterned surfaces using template-mediated UV replica molding.^[11]

Surface plasmon resonators are able to trigger high local absorption in OPV solar cells within the material’s absorption window by exploiting the physical principle of plasmon resonance. Surface plasmons are bound electromagnetic oscillations of electrons at the interface between a metal and a dielectric material stimulated by light and amplifying the electromagnetic radiation at the resonance wavelength. The generation of plasmon resonators then usually needs metal nanoparticles implanted on surfaces or embedded in dielectric media, with obvious increase in the device materials costs together with possible consequent problems such as shorts and surface wrinkling.

On the other hand, the simplest light trapping approach that could enhance the active layer absorption and cell photocurrent is the employment of light scattering centres in the device structure. The randomization of the light propagation pathway inside the solar cell stack results in an increased interaction between the solar radiation and the photoactive absorbing layer. This, in principle, might lead to a substantial enhancement of active layer absorption, device short-circuit photocurrent and PCE.^[12] In the dye sensitized solar cells (DSSCs) technology, the use of a scattering material in the device structure is a consolidated technique since more than fifteen years.^[13] Indeed, the introduction of a TiO₂ layer with large nanoparticles^[13a,b,c] or the dispersion of nanozeolites into the standard TiO₂ nanoporous layer has shown significant improvements in terms of performance and lifetime stability^[13d,e]. On the other hand, controlled light scattering in BHJ OPV devices is a relatively recent technique. In particular, research has focused on the use of metal oxide (TiO₂, ZnO, MoO₃,...)^[14] or metallic (Au, Ag,...)^[7] nanostructured materials (often nanoparticles) dispersed in the buffer layer or in the active layer of the OPV stack. However, these materials allowed the enhancement of the OPV devices performance by mainly exploiting their plasmon resonance effects and buffer layer work-function tuning, rather than light scattering.

2. SCATTERING PARTICLES IN THE PEDOT:PSS LAYER OF P3HT:PC₆₁BM-BASED SOLAR CELLS

Here, an application of hydrotalcite nanoparticles (HTs) as scattering centers in OPV devices is presented.

Hydrotalcites are among the most attractive cheap and non-toxic micro- and nano-structured inorganic materials and have been already used in a wide range of applications in the fields of polymeric nanocomposites,^[15] heterogeneous catalysis,^[16] photochemistry^[17] and dye sensitized photovoltaics.^[18]

In detail, HTs have the general formula $[M(II)_{1-x}M(III)_x(OH)_2]^{x+}[A^{n_x/n}]_mH_2O$, where $M(III)$ cations are typically Al, Cr, Fe, or Ga and $M(II)$ are typically Mg, Zn, Ni,

Co, or Cu, while A^{n-} is a charge balancing anion (organic, inorganic or metallorganic) with n as ionic valence and x is the $M(III)$ molar fraction. They can be easily synthesized in a variety of dimensions, with crystallite diameters ranging from some micrometers^[19] to nanometers.^[20] For their chemical nature, HTs reveal a high affinity with the sulfonate groups of PSS (poly(4-styrenesulfonate)),^[21] enabling their potential use in composite materials with PEDOT:PSS.

One of the most common type of HTs are the Zn(II)-Al(III) based HTs (ZnAl-HTs), that can be easily synthesized in the form of crystalline nanoplatelets with a diameter of about 150-200 nm and a thickness of ~ 20 nm.^[20c,d] This high aspect-ratio could allow a preferential in-plane self-orientation of HTs in the composite ZnAl-HTs/PEDOT:PSS material, thus leading to homogeneous and smooth films with a maximized scattering cross-section per particle.

On the basis of the hydrophilicity, electrical inertness and semi-transparency properties of ZnAl-HTs, it is here reported their application in the PEDOT:PSS layer of OPV solar cells. P3HT:PC₆₁BM based BHJ solar cells incorporating pristine PEDOT:PSS or ZnAl-HTs/PEDOT:PSS films have been fabricated with the standard OPV structure (**Figure 39**), revealing an interesting and effective bi-functionality of the ZnAl-HTs/PEDOT:PSS composite film, both as hole transporting and light scattering layer.

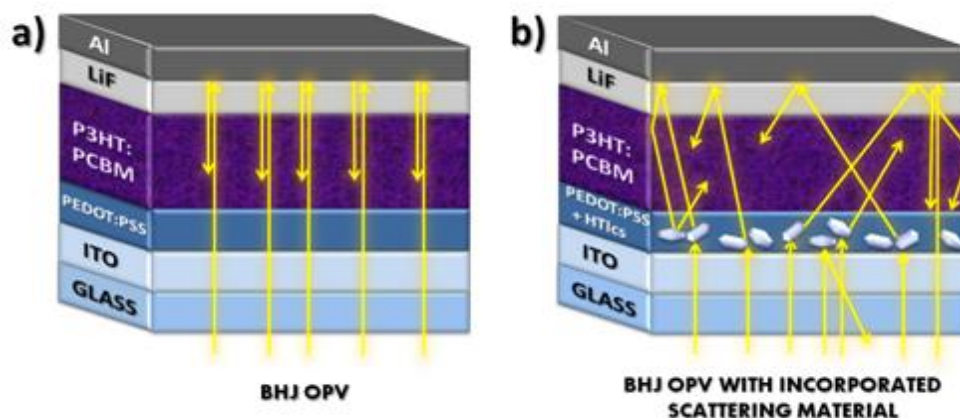


Figure 39 a) Schematic representation of a standard BHJ OPV and b) a BHJ OPV with the composite HTs/PEDOT:PSS film acting as scattering layer.

Two different synthetic routes have been used to prepare ZnAl-HTs: the first one is based on a variation of the known urea method, using a mixture of water and ethylene glycol as solvent,^[18b] while the second one is based on the double microemulsion process.^[20c,d] Both methods led to crystalline ZnAl-HTs (called respectively ZnAl-HT_{wg} and ZnAl-HT _{μ E}) with similar dimensions but different aggregation tendencies.

Since HTs are metal hydroxides which can be dissolved in acid environments, a pH-neutral PEDOT:PSS formulation is used in this work. The morphological, optical and electrical properties of the composite ZnAl-HT_{wg}/PEDOT:PSS and ZnAl-

HT_{μE}/PEDOT:PSS films have been studied for different HTs concentrations and correlated with the corresponding OPV performances.

2.1. Experimental

2.1.1. Materials and methods

All reagents, regioregular P3HT (Rieke Metals), PC₆₁BM (American Dye Source), PEDOT:PSS (Orgacon™ N-1005, Sigma-Aldrich), Zn(NO₃)₂·6H₂O, Al(NO₃)₃·9H₂O, cetyltrimethylammonium bromide (CTAB), urea and various solvents were purchased from commercial sources and used without further purification unless otherwise specified. Synthetic details and the procedure for the preparation of colloidal aqueous dispersions of ZnAl-HTs nanoparticles are reported in literature.^[18b, 20c,d]

2.1.2. HTs/PEDOT:PSS thin-films preparation and characterization

pH-neutral PEDOT:PSS was used after previous filtration with a 0.45 μm filter. The ZnAl-HTs dispersions in water were sonicated for 10 minutes before use. The concentration of ZnAl-HT_{μE} and ZnAl-HT_{wg} starting solutions were 6.6 mg/mL (for lower concentrations mixed solutions) or 15 mg/mL (for higher concentrations). To avoid dilution effects, small volumes (at maximum, a volume of 67 μL in 1 mL, used for the 5 wt% ZnAl-HTs/PEDOT:PSS solution) of these ZnAl-HTs dispersions were added to the PEDOT:PSS aqueous solution to prepare mixed ZnAl-HTs/PEDOT:PSS blends with the following nanoparticles loads: 0.25%, 0.50%, 1%, 5% (weight % vs. PEDOT:PSS solid content). Each solution was sonicated at room temperature for 10 minutes, then ZnAl-HTs/PEDOT:PSS films were prepared by spin coating (on pre-cleaned and plasma-treated glass substrates) at 4000 rpm for 1 minute and subsequent annealing at 120 °C for 10 minutes. The thicknesses of the various films were measured with a profilometer (KLA Tencor, P-6) and all resulted ~ 50 nm thick.

HTs and HTs/PEDOT:PSS films were imaged with a scanning electron microscope SEM, ZEISS LEO 1530 FEG, after metallization with gold. AFM images were taken with a Solver Pro (NT-934 MDT) scanning probe microscope in tapping mode.

For X-ray diffraction (XRD) analysis, the films were prepared by drop casting blends with HTs loads of 5 wt% for both ZnAl-HT_{μE} and ZnAl-HT_{wg}, in order to achieve detectable variations. XRD patterns were recorded with a Philips X'PERT PRO MPD diffractometer operating at 40 kV and 40 mA, step size 0.0170 2θ degree and 20 s step scan, using the CuKα radiation and an X'Celerator detector.

The total transmittance (T%) of the doped and undoped PEDOT:PSS films was measured with a Perkin-Elmer Lambda-9 UV-vis spectrophotometer equipped with an integrating sphere.

The descriptive scattering parameters of the doped and undoped PEDOT:PSS films were determined experimentally from laser in-line transmission (LT) measurements.^[22] Haze parameter H_t ^[23] have been derived by measuring the linear and total transmission of a monochromatic light passing through the sample. The 488 nm emission of an Ar+ Innova 90 Coherent laser passes perpendicularly through the sample (the power is set at 40 mW in order to have a high signal to noise ratio but avoiding any possible distortion due to local heating of the sample) and the transmitted light is collected through a lens by a Ophir laser power meter. The transmitted light collected after passing through a pinhole positioned 50 cm after the sample, with a narrow (diameter $\phi = 1$ mm) or wide ($\phi = 20$ mm) aperture, are called T_{lin} (in-line transmitted light) and T_{tot} (total transmitted light) respectively.

The conductivity of doped and undoped PEDOT:PSS films was measured through the four-point probe technique applied to devices with glass/ITO electrodes arranged in the geometry reported in **Figure 44**.^[24]

2.1.3. Device fabrication and characterization

Patterned ITO-coated glasses ($R_s \sim 10 \Omega/\text{sq}$, ITO roughness RMS < 1 nm) were cleaned in sequential sonicating baths for 10 min, twice in acetone and once in isopropanol, then cleaned in an ozone-plasma chamber for 10 min. Next, the PEDOT:PSS or HTs/PEDOT:PSS layer was spun-cast from the corresponding aqueous suspensions on the ITO surface at 4000 rpm, for 1 minute, and subsequently annealed at 120°C for 10 minutes (as for the films on glass). Samples were then transferred inside the glove box (< 0.1 ppm of O_2 and H_2O). A P3HT:PC₆₁BM 1:1 (wt/wt) solution was previously prepared in glove box with a total concentration of 60 mg/mL in dry chlorobenzene: orthodichlorobenzene (1:1 v/v) and left under stirring and heating at 70 °C overnight. The P3HT:PC₆₁BM solution was then spun-cast on top of the ITO/PEDOT:PSS or ITO/ZnAl-HTs/PEDOT:PSS surface at 1000 rpm for 10 seconds. The wet active layers were slowly dried and then annealed at 110 °C for 10 minutes. To complete the device fabrication, LiF/Al cathodes (0.6 nm and 100 nm respectively) were next deposited sequentially without breaking vacuum ($\sim 3 \times 10^{-6}$ Torr) using a thermal evaporator directly connected to the glove box. The current-voltage (I-V) characteristics of complete OPV devices were recorded by a Keithley 236 source-measure unit under simulated AM1.5G illumination of 100 mW/cm² (Abet Technologies Sun 2000 Solar Simulator). The light intensity was determined by a standard silicon photodiode filtered with a KG5 color glass filter to bring spectral mismatch to unity. During testing, each device was illuminated through a calibrated mask (exactly 6 mm²), to avoid any excess of photocurrent generated from the parasitic device regions outside the overlapped electrode area. All solar cells were tested inside the glove box in oxygen and moisture free environment. EQE spectra were measured with a home built system on encapsulated devices: monochromatic light was obtained with a Xenon arc lamp from Lot-Oriel (300

Watt power) coupled with a Spectra-Pro monochromator. The photocurrent produced by the device passed through a calibrated resistance (50 Ω) and the voltage signal was collected with a Lock-In Digital Amplifier SR830. Signal was pulsed by means of an optical chopper (\sim 500 Hz frequency). A calibrated UV-enhanced Silicon photodiode was used as reference.

2.2. Results and discussion

2.2.1. HTs/PEDOT:PSS thin-film properties

Before comparing the OPV properties of doped and undoped PEDOT:PSS based solar cells, we investigated the structural properties of HTs once dispersed in the polymeric matrix, together with the resulting HTs/PEDOT:PSS composite thin-film morphological, electrical and optical properties. Some key parameters, required for these films to be used as scattering layers in OPV devices, were analyzed: *i*) the chemical and structural stability of the HTs in the PEDOT:PSS matrix; *ii*) the homogeneous distribution of the HTs in the film, combined with a preferential in-plane self-orientation; *iii*) the HTs/PEDOT:PSS composite film surface regularity and flatness, to favor the subsequent deposition of the photoactive layer; *iv*) the maintenance of the optical (high visible light transmission) and electrical (high conductivity) properties of the HTs/PEDOT:PSS thin-film. To this end, a variety of techniques, such as x-ray diffraction, scanning electron microscopy, atomic force microscopy, visible light total transmission and electrical conductivity, have been used for deep investigations.

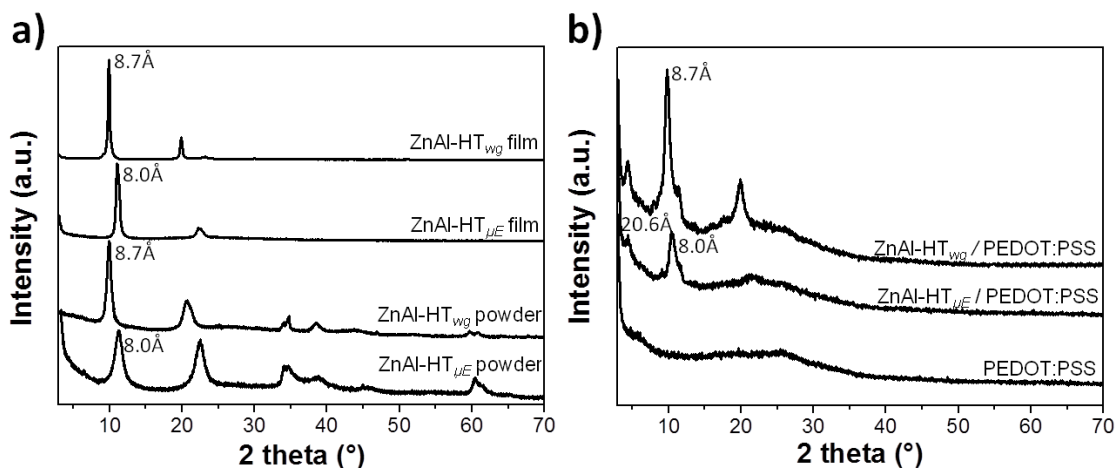


Figure 40 XRD patterns on glass substrates of: **a)** ZnAl-HT_{μE} and ZnAl-HT_{wg} powders compared to the ZnAl-HT_{μE} and ZnAl-HT_{wg} films; **b)** ZnAl-HTs/PEDOT:PSS hybrid films prepared with a HTs load of 5 wt% vs. PEDOT:PSS, compared to the reference PEDOT:PSS film.

Figure 40a shows the XRD patterns of pristine ZnAl-HT_{μE} and ZnAl-HT_{wg} powders compared to the ZnAl-HT_{μE} and ZnAl-HT_{wg} films, while in **Figure 40b** are reported those of the ZnAl-HTs/PEDOT:PSS hybrid films prepared with a HTs load of 5 wt% (required for detectable variations) compared to the undoped PEDOT:PSS film. It can be seen that in the composite films the main reflections at

8.0 Å and 8.7 Å (**Figure 40b**) are the same as in the HTs pristine films (**Figure 40a**) and compatible with the presence of bromide and nitrate anions in the interlayer region.^[20c,15d] The presence of these reflections indicates that the lamellar structure of HTs is preserved in the polymer matrix, excluding any delamination process due to the HTs/PEDOT:PSS interactions. Moreover, the very weak reflection detected at 4.4°, corresponding to a d spacing of 20.6 Å, indicates a partial intercalation of some PSS species in the interlayer region of HTs,^[21] confirming the good affinity between sulfonate groups of the PSS and HTs. In addition, unlike the powder spectra (**Figure 40a**), where the HTs are randomly arranged, the absence of any in-plane reflections ($h,k \neq 0$) at high angles evidences a favourable in-plane orientation of the HTs nanoplatelets in the composite film.^[25]

SEM was used to characterize the topography of the blend films.

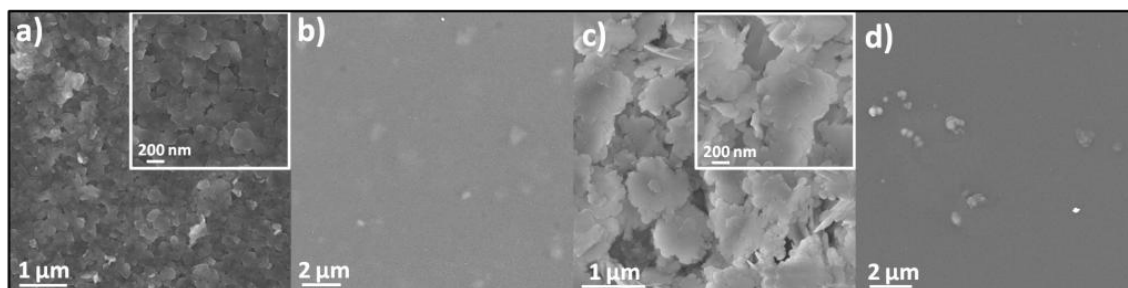


Figure 41 SEM images of: **a)** pristine ZnAl-HT_{μE}; **b)** 0.50 wt% ZnAl-HT_{μE}/PEDOT:PSS; **c)** pristine ZnAl-HT_{wg} and **d)** 0.50 wt% ZnAl-HT_{wg}/PEDOT:PSS based films deposited on glass substrates.

In agreement with the previous considerations, the SEM image of the ZnAl-HT_{μE}/PEDOT:PSS film with 0.50 wt% of HTs (see **Figure 41b**) shows that the HTs nanoparticles are homogeneously dispersed in the PEDOT:PSS matrix. In addition, the preferential in plane orientation of the platelets is confirmed, since the majority of the HTs are embedded in the bulk PEDOT:PSS layer and only a few superficial protrusions are present. However, the SEM image of the blend ZnAl-HT_{wg}/PEDOT:PSS with 0.50 wt% HTs load (see **Figure 41d**) shows some nanoparticle aggregates, indicating the slightly higher aggregation tendency of ZnAl-HT_{wg}, compared to ZnAl-HT_{μE}, in agreement with the images of pristine ZnAl-HT_{wg} (**Figure 41c**) and ZnAl-HT_{μE} (**Figure 41a**) films.

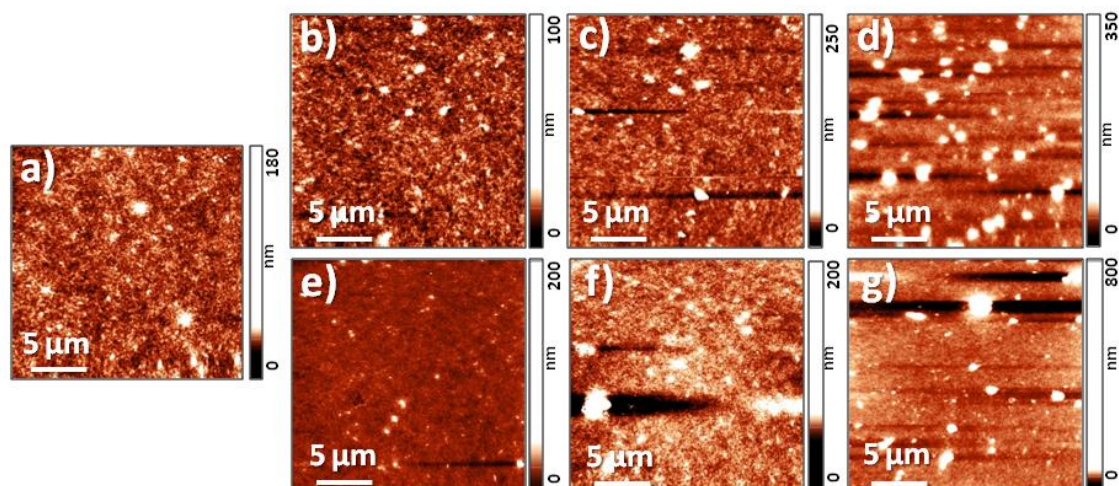


Figure 42 AFM images ($20 \times 20 \mu\text{m}$) of the films on glass substrates: **a)** pristine PEDOT:PSS (RMS = 5.0 nm); **b)** ZnAl-HT $_{\mu E}$ /PEDOT:PSS, 0.50 wt% of HTs vs. PEDOT:PSS (RMS = 5.1 nm); **c)** ZnAl-HT $_{\mu E}$ /PEDOT:PSS, 1 wt% of HTs vs. PEDOT:PSS (RMS = 5.6 nm); **d)** ZnAl-HT $_{\mu E}$ /PEDOT:PSS, 5 wt% of HTs vs. PEDOT:PSS (RMS = 17 nm); **e)** ZnAl-HT $_{wg}$ /PEDOT:PSS, 0.50 wt% of HTs vs. PEDOT:PSS (RMS = 5.1 nm); **f)** ZnAl-HT $_{wg}$ /PEDOT:PSS, 1 wt% of HTs vs. PEDOT:PSS (RMS = 10 nm); **g)** ZnAl-HT $_{wg}$ /PEDOT:PSS, 5 wt% of HTs vs. PEDOT:PSS (RMS = 30 nm).

The morphological properties of the doped and undoped PEDOT:PSS based films have been also investigated by AFM (**Figure 42**). The topographical analysis of ZnAl-HT $_{\mu E}$ /PEDOT:PSS films reveals that ZnAl-HT $_{\mu E}$ loads of 0.50 wt% and 1 wt% (**Figure 42b** and **c**) have a weak influence on the film roughness (RMS of ~ 5.0 and 5.6 nm, respectively), which is very similar to that of the undoped PEDOT:PSS film (**Figure 42a**, RMS ~ 5.0 nm). However, by further increasing the ZnAl-HT $_{\mu E}$ content up to 5 wt%, the RMS sharply increases to 16.8 nm, due to the formation of micrometric aggregates (**Figure 42d**). A similar trend, with a higher dependence on the HTs loads, is found for ZnAl-HT $_{wg}$ based composites, for which the RMS increases from ~ 5.1 nm to ~ 10 nm and ~ 30 nm for particles loads of 0.50 wt% (**Figure 42e**), 1 wt% (**Figure 42f**) and 5 wt% (**Figure 42g**) respectively, in accordance with the higher aggregation tendency of ZnAl-HT $_{wg}$ with respect to ZnAl-HT $_{\mu E}$.

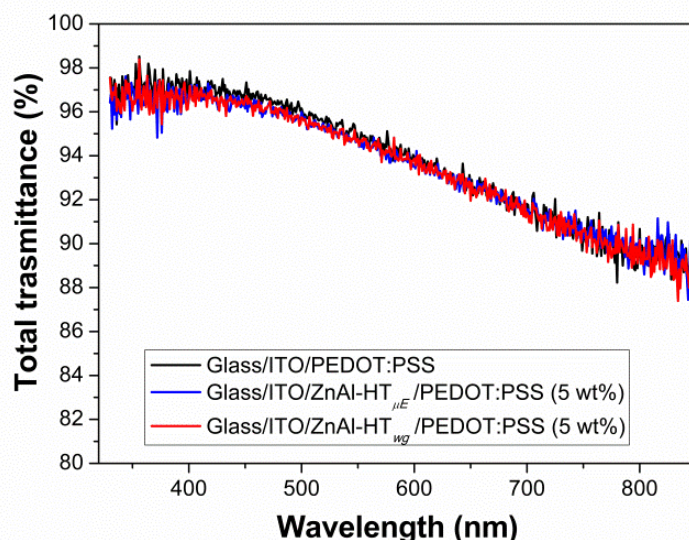


Figure 43 Total transmittance of the substrates: glass/ITO/PEDOT:PSS (black curve), glass/ITO/ZnAl-HT _{μE} /PEDOT:PSS with 5 wt% of HTs vs. PEDOT:PSS (blue curve); glass/ITO/ZnAl-HT_{wg}/PEDOT:PSS with 5 wt% of HTs vs. PEDOT:PSS (red curve).

Finally, the total transmittance of the PEDOT:PSS film and of the most highly doped (5 wt%) HTs/PEDOT:PSS films (see **Figure 43**), measured with a spectrophotometer equipped with an integrating sphere to take into account the contributions of both unscattered and scattered light, results unvaried in the whole visible range (350 – 850 nm). This excludes the possibility that any variation in the photovoltaic response of the solar cells could be due to a change in transparency of the buffer layer following the inclusion of HTs.

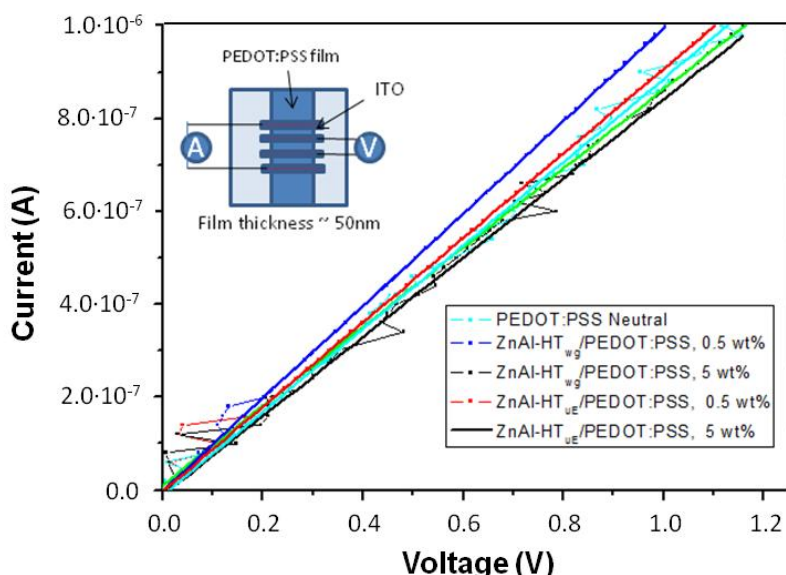


Figure 44 I-V curves measured in the four-points probes resistivity experiments on devices prepared with doped or undoped PEDOT:PSS films having electrodes and contact geometry represented in the upper-left side of the image. The slopes of the interpolation lines gives for each set of points the following approximated resistivity (R) values for the films: $R(\text{PEDOT:PSS}) = 82 \Omega \cdot \text{cm}$; $R(\text{ZnAl-HT}_{wg}/\text{PEDOT:PSS}, 0,5 \text{ wt}\%) = 78 \Omega \cdot \text{cm}$; $R(\text{ZnAl-HT}_{wg}/\text{PEDOT:PSS}, 5\%) = 71 \Omega \cdot \text{cm}$; $R(\text{ZnAl-HT}_{\mu E}/\text{PEDOT:PSS}, 0,5 \text{ wt}\%) = 82 \Omega \cdot \text{cm}$; $R(\text{ZnAl-HT}_{\mu E}/\text{PEDOT:PSS}, 5 \text{ wt}\%) = 81 \Omega \cdot \text{cm}$.

Analogously, the conductivity experiments on the HTs/PEDOT:PSS films reveals that any influence on the PEDOT:PSS conductivity due to the presence of HTs in the film (up to 5 wt% of ZnAl-HT_{μE} or ZnAl-HT_{wg}) can be neglected (**Figure 44**).

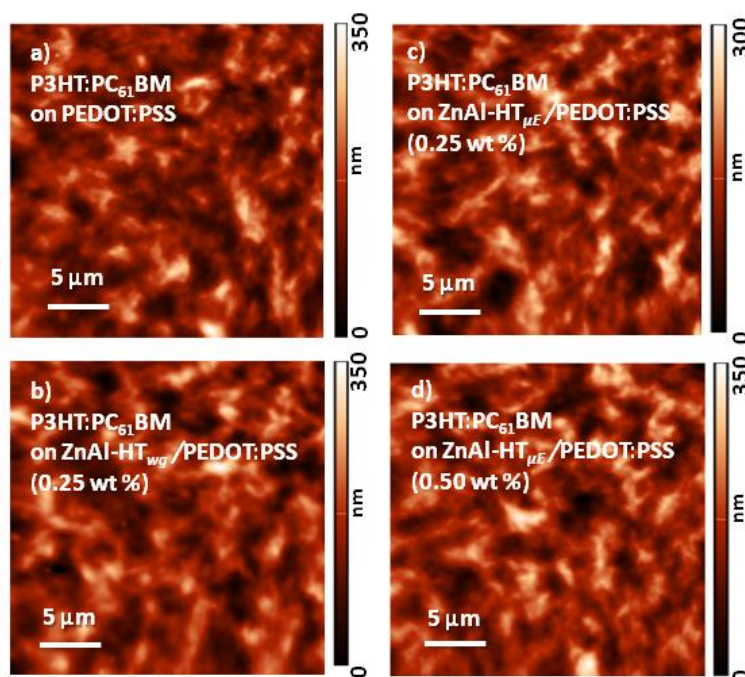


Figure 45 AFM images of the P3HT:PC₆₁BM films deposited on glass/ITO/PEDOT:PSS (**a**, RMS = 46 nm), glass/ITO/ZnAl- HT_{wg}:PEDOT:PSS with 0.25 wt% of HTs vs. PEDOT:PSS (**b**, RMS = 46 nm), glass/ITO/ZnAl- HT_{μE}:PEDOT:PSS with 0.25 wt% of HTs vs. PEDOT:PSS (**c**, RMS = 49); glass/ITO/ZnAl- HT_{μE}:PEDOT:PSS with 0.50 wt% of HTs vs. PEDOT:PSS (**d**, RMS = 40).

The positive results obtained from the morphological, electrical and optical analysis on the HTs/PEDOT:PSS films suggested to test them in BHJ OPVs. In particular, the smooth and regular surfaces observed for the HTs/PEDOT:PSS films with lower HTs concentrations (0.25 and 0.50 wt%) is not expected to induce morphological changes of the overlying P3HT:PC₆₁BM layer, (as evidenced by AFM, **Figure 45**). In addition, the HTs in-plane preferential orientation is favorable for maximizing the HTs/PEDOT:PSS film light scattering properties.

2.2.2. Scattering of HTs:PEDOT:PSS films

To investigate the scattering effects of the HTs/PEDOT:PSS films, laser in-line transmission measurements (LT, **Figure 46a**) were performed on doped and undoped PEDOT:PSS films deposited on glass.

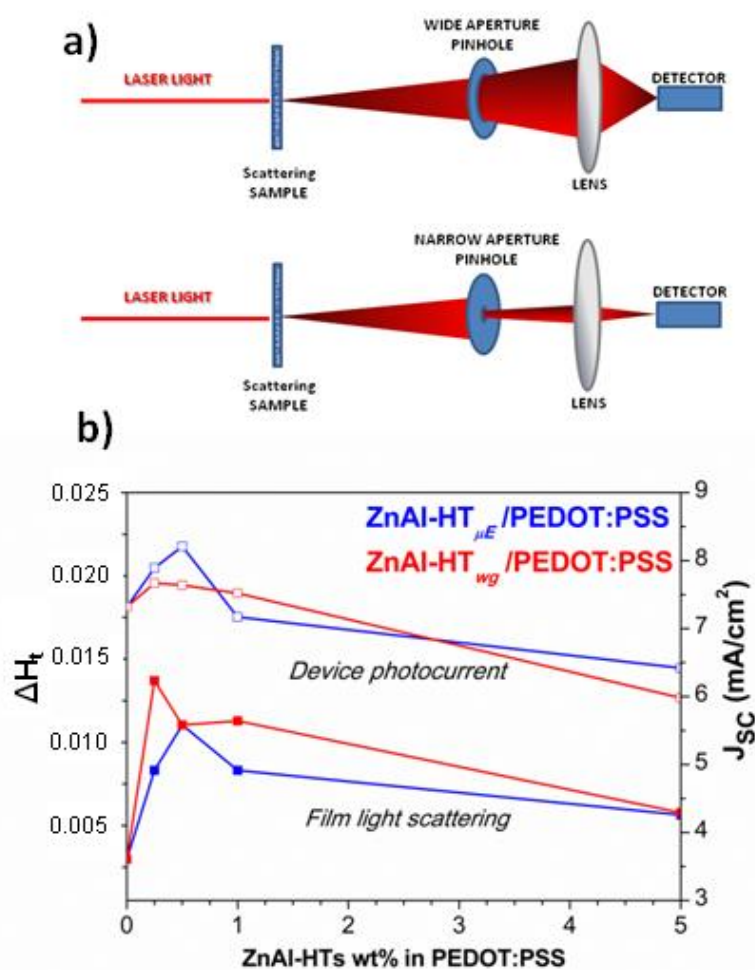


Figure 46 a) Scheme of the laser in-line transmission measurements; **b)** ΔH_t parameters (versus glass) calculated for the ZnAl-HTs/PEDOT:PSS films (left y axis, filled squares) compared to the J_{sc} values of the ITO/(ZnAl-HTs/PEDOT:PSS)/P3HT:PC₆₁BM/LiF/Al corresponding devices (right y axis, empty squares), at different ZnAl-HTs concentrations (0, 0.25, 0.50, 1 and 5 wt% of ZnAl-HTs vs. PEDOT:PSS). Data relative to ZnAl-HT_{μE} are reported in blue and data relative to ZnAl-HT_{wg} in red.

In general, with this method an approximation of the diffused transmittance (T_{dif}) of a semi-transparent sample is given by the difference between the film total transmittance (T_{tot}) and linear transmittance (T_{lin}). An approximated haze parameter (H_t) for transmitted light can then be determined as $H_t = (T_{tot} - T_{lin}) / T_{tot} = T_{dif} / T_{tot}$. In this way, the enhanced light scattering properties of the ZnAl-HTs/PEDOT:PSS films, compared to the bare PEDOT:PSS film, can be evaluated through the difference between their H_t and the H_t of the reference PEDOT:PSS film (this ratio can be called as differential haze, or ΔH_t). Therefore, the H_t parameters of undoped PEDOT:PSS and HTs/PEDOT:PSS composited films on glass have been calculated, and the corresponding ΔH_t are reported in **Figure 46b**. As expected, the ΔH_t values of the glass/ZnAl-HT_{μE}/PEDOT:PSS films at various particle concentrations increases with respect to the glass/PEDOT:PSS reference film, following the same trend of the corresponding devices J_{sc} measured at 1 sun (also reported, for comparison, in **Figure 46b**). In particular, a maximum ΔH_t is obtained

for a particle concentration of 0.50 wt%, while at higher concentrations (1 and 5 wt%) ΔH_t gradually decreases.

Analogously, the ΔH_t of the glass/ZnAl-HT_{wg}/PEDOT:PSS films increases with respect to the bare glass/PEDOT:PSS film, reaching a maximum value for 0.25 wt% particle concentration and gradually decreases for higher ZnAl-HT_{wg} loads, again following the I_{sc} trend of the corresponding OPV devices. It has to be noted that the decrease in the ΔH_t parameter for high particles concentrations, both for ZnAl-HT _{μE} and ZnAl-HT_{wg}, is likely due to the formation of the micrometric aggregates previously observed in the morphological analysis of the highly doped PEDOT:PSS films (SEM and AFM images, **Figures 41** and **42**, respectively).

These measurements validate our hypothesis, confirming that the addition of the ZnAl-HTs to the PEDOT:PSS layer enhances the scattering properties of the film for the transmitted light.

2.2.3. Devices performance

The potential of HTs as effective scattering centers in OPV devices was investigated in BHJ solar cells using P3HT:PC₆₁BM as active layer. The device structure employed is glass/ITO/PEDOT:PSS/P3HT:PC₆₁BM/LiF/Al (**Figure 39**). Details for the device fabrication and characterization are given in the experimental section. Different HTs loads (0.25 wt%, 0.50 wt%, 1 wt%, 5 wt% HTs vs. PEDOT:PSS) have been tested.

Table 9 Summary of the photovoltaic performances of the P3HT:PC₆₁BM based BHJ OPV devices prepared with different buffer layers: pristine PEDOT:PSS, or PEDOT:PSS doped with different loads of ZnAl-HT_{wg} or ZnAl-HT _{μE} . The reported parameters are the values averaged over ~ 15 devices and the maximum values (in brackets).

ZnAl-HTs type	ZnAl-HTs/PEDOT:PSS wt%	J_{sc} (mA/cm ²)	V_{oc} (V)	FF (%)	PCE (%)
-	0	7.21 (7.32)	0.54 (0.54)	63 (66)	2.47 (2.58)
ZnAl-HT _{wg}	0.25	7.55 (7.67)	0.54 (0.54)	64 (66)	2.63 (2.73)
	0.50	7.64	0.54	65	2.68
	1	7.52	0.54	62	2.51
	5	5.98	0.56	57	1.93
ZnAl-HT _{μE}	0.25	7.89	0.55	62	2.68
	0.50	8.04 (8.21)	0.54 (0.54)	64 (67)	2.76 (2.98)
	1	7.17	0.54	65	2.54
	5	6.42	0.54	60	2.09

Table 9 summarizes the photovoltaic response data of the corresponding BHJ OPV devices (maximum and average values calculated over ~ 15 devices).

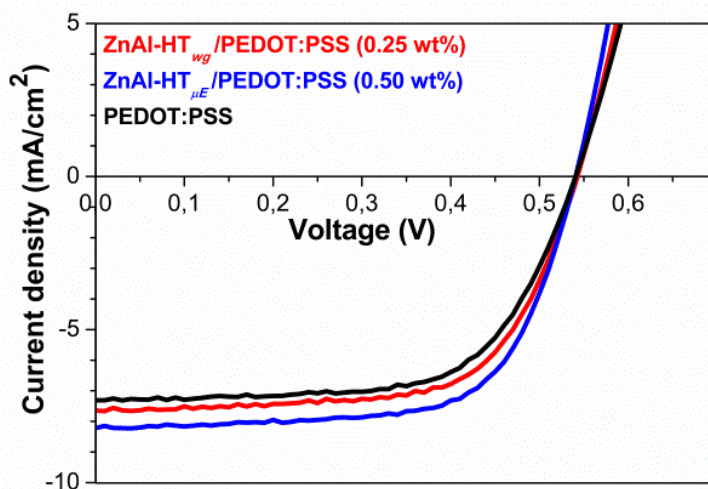


Figure 47 J-V plots of the best performing P3HT:PC₆₁BM based BHJ OPV devices prepared with doped or undoped PEDOT:PSS films.

Representative current density-voltage plots of the best performing solar cells, measured under standard illumination AM1.5G, are shown in **Figure 47**. The optimized reference solar cell, based on pristine pH-neutral PEDOT:PSS (~ 50 nm), affords a J_{SC} of 7.32 mA/cm², a V_{OC} of 0.54 V, a FF of 66% and a PCE of 2.58%. The highest OPV performances were achieved for the devices prepared with 0.50 wt% of ZnAl-HT_{μE} and 0.25 wt% of ZnAl-HT_{wg} dispersed in the PEDOT:PSS layer. In fact, when the ZnAl-HT_{μE}/PEDOT:PSS composite film (with HTs 0.50 wt%) is used in the solar cells, the best device exhibits a J_{SC} of 8.21 mA/cm², a V_{OC} of 0.54 V, a FF of 67% and a PCE of 2.98%, which corresponds to ~16% PCE improvement with respect to the reference cell (~12% on average). A similar but less marked trend was observed for ZnAl-HT_{wg} based devices, for which the best performance is peaked at a particle load of 0.25 wt%, leading to J_{SC} , V_{OC} , FF and PCE of 7.67 mA/cm², 0.54 V, 66% and 2.73%, respectively, which correspond to an improvement of ~ 12% with respect to the reference cell (~6% on average). Noticeably, the main factor determining the efficiency improvements for the devices with HTs/PEDOT:PSS layers is the enhancement of the short-circuit current density, in perfect agreement with the light scattering properties of the doped buffer layer.

By further increasing the HTs content (up to 5 wt%) in the PEDOT:PSS films, the J_{SC} , FF and PCE significantly decrease. This could be ascribed to several factors, such as: *i*) the presence in relatively high percentage of electrically inert HTs, increasing the series resistance within the OPV device; *ii*) a reduced nanoscale self-organization of the overlying photoactive layer (P3HT:PC₆₁BM), induced by the rough and irregular surface of the highly doped buffer layer.

It should be noted that within all films, the highest ΔH_t has been obtained for the ZnAl-HT_{wg}/PEDOT:PSS film with 0.25 wt% nanoparticles concentration. However, the corresponding ZnAl-HT_{wg}/PEDOT:PSS based solar cell doesn't show the highest photocurrent, within all devices. This discrepancy could be explained through the higher aggregation tendency of the former particles comparing to the

latter, as discussed before (**Figure 41**). The possible presence of aggregates, embedded in the composite film bulk or at the ITO/PEDOT:PSS interface, for low particles loads (25 wt% and 0.50 wt%), cannot be excluded through SEM or AFM surface analysis (**Figures 41b** and **41d**, **Figure 42b** and **42e**). Therefore it is reasonable to assume that the limiting factor for the photocurrent generation of the HT_{wg}/PEDOT:PSS based device is the higher content of aggregates in the HT_{wg}/PEDOT:PSS film comparing to the HT_{μE}/PEDOT:PSS one, which could partially limit the charge extracting ability of the former buffer layer comparing to the latter.

A further evidence of the effectiveness of the ZnAl-HTs/PEDOT:PSS films in enhancing the devices photocurrent through light scattering can be given by the study of their spectral response.

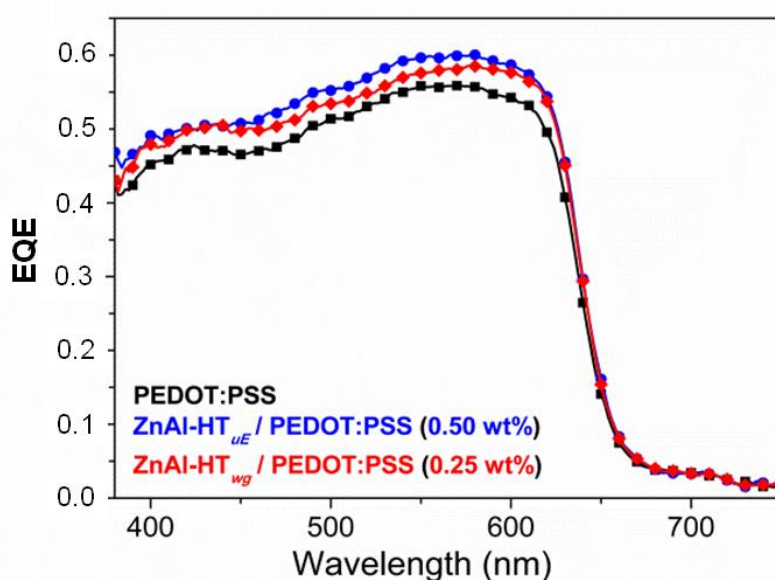


Figure 48. External Quantum Efficiency (EQE) spectra of the best performing P3HT:PC₆₁BM based BHJ OPV devices prepared with doped or undoped PEDOT:PSS films.

Figure 48 shows the External Quantum Efficiency (EQE) spectra of the best performing solar cells with ZnAl-HTs/PEDOT:PSS films, in comparison with the reference cell.

The resulting EQE values are gradually enhanced passing from the reference device (maximum EQE = 0.56), to the cells based on 0.25 wt% of ZnAl-HT_{wg} (maximum EQE = 0.58), to the one with 0.50 wt% of ZnAl-HT_{μE} (maximum EQE = 0.60). Convolution of these EQE spectra with the 1.5AM solar spectrum gave calculated short circuit current densities in good agreement with those obtained from the I-V measurements. Moreover, no significant alteration in the shape of the EQE spectra of the ZnAl-HTs/PEDOT:PSS based devices, with respect to the reference cell, is registered. This further confirms that, for low HTs loads, no significant changes are induced by the underlying PEDOT:PSS doped layer on the P3HT:PC₆₁BM morphology (as evidenced by AFM, **Figure 45**), since they would likely result in absorption and EQE spectral modifications.

These results demonstrate the efficacy of the HTs/PEDOT:PSS layer in enhancing the propagation length and trapping of the incident light into the BHJ OPV device, leading to a significant active layer absorption enhancement and consequent increase of J_{sc} , EQE and PCE.

2.3. Conclusions

In conclusion, two series of PEDOT:PSS films doped with ZnAl-HT_{wg} or ZnAl-HT _{μ E} were employed in P3HT:PC₆₁BM based BHJ OPV devices to investigate their scattering properties. The results demonstrate that ZnAl-HTs could effectively scatter a portion of the incident light into larger angles through the active layer of the OPV solar cell, enhancing its light absorption and improving the device J_{sc} and PCE. Indeed, the HTs/PEDOT:PSS films with the highest haze for transmitted light (ΔH_t) resulted in devices with improved performances, with PCEs going from 2.58%, for the device with pristine PEDOT:PSS, to 2.73% and to 2.98% for the devices with ZnAl-HT_{wg}/PEDOT:PSS and ZnAl-HT _{μ E}/PEDOT:PSS films, respectively.

The extraordinary versatility of HTs, given by their relatively simple synthetic procedures and by the possibility to combine a wide variety of metals and counterions in their chemical structure, paves the way to the engineering of novel HTs-based composites for applications in the OPVs technology. Indeed, we expect that device performances can be further improved by a rational and fine tuning of the optical, electrical and chemical properties of the HTs, taking advantage of the results and considerations reported in this study.

This approach might allow a potential and effective implementation of HTs/PEDOT:PSS composite films in the recombination layer of tandem solar cells. Indeed, the active layers of both the bottom and top cells could benefit of the scattering effect induced by the doped intermediate layer.^[26]

3. BIBLIOGRAPHY

- [1] (a) G. Li, V. Shrotriya, Y. Yao, Y. Yang, *J. Appl. Phys.*, 2005, 98, 043704; (b) K.M. Coakley, M. D. McGehee, *Chem. Mater.*, 2004, 16, 4533; (c) A. Abbotto et al., *J. Polym. Sci. A Polym. Chem.*, 2012, 50, 2829.
- [2] T. Tromholt, In: F. C. Krebs (Ed.), *Stability and Degradation of Organic and Polymer Solar Cells*, First Edition, (John Wiley & Sons Ltd, UK, 2012) 243.
- [3] (a) J. Liu, M. A. G. Namboothiry, D. L. Carroll, *Appl. Phys. Lett.*, 2007, 90, 133515; (b) B. O'Connor, D. Nothorn, K. P. Pipe, M. Shtein, *Opt. Express*, 2010, 18, A432.
- [4] M. O'Neill, S. M. Kelly, *Adv. Mater.*, 2011, 23, 566.
- [5] (a) M. G. Debije, P. P. C. Verbunt, *Adv. Energy Mater.*, 2012, 2, 12; (b) S. Quici et al., *Chem. Mater.*, 2009, 21, 2941; (c) L. Armelao et al., *ChemPhysChem*, 2010, 11, 2499.
- [6] H. K. Raut, V. A. Ganesh, A. S. Nair, S. Ramakrishna, *Energy Environ. Sci.*, 2011, 4, 3779.
- [7] (a) I. Kim, D. S. Jeong, T. S. Lee, W. S. Lee, K.-S. Lee, *J. Appl. Phys.*, 2012, 111, 103121; (b) D. D. S. Fung et al., *J. Mater. Chem.*, 2011, 21, 16349; (c) M.-G. Kang, T. Xu, H. J. Park, X. Luo, L. J. Guo, *Adv. Mater.*, 2010, 22, 4378; (d) A.Y. Mahmoud, J. M. Zhang, D. L. Ma, R. Izquierdo, V. V. Truong, *Org. Electron.*, 2012, 13, 3102; (e) D. H. Wang et al., *Angew. Chem., Int. Ed.*, 2011, 50, 5519.
- [8] K. Forberich, G. Dennler, M. C. Scharber, K. Hingerl, T. Fromherz, C. J. Brabec, *Thin Solid Films*, 2008, 516, 7167.
- [9] W. C. Luk, K. M. Yeung, K. C. Tam, K. L. Ng, K. C. Kwok, C. Y. Kwong, A. M. C. Ng, A. B. Djuri, *Org. Electron.*, 2011, 12, 557.
- [10] T. Søndergaard, J. Gadegaard, P. K. Kristensen, T. K. Jensen, T. G. Pedersen, K. Pedersen, *Opt. Express*, 2010, 18, 26245.
- [11] S.-J. Choi, S.-Y. Huh, *Macromol. Rapid Commun.*, 2009, 31, 539.
- [12] (a) B. Jacobs, G. De Mey, *Solid-State Electron.*, 1978, 21, 1191; (b) S. Hore, P. Nitz, C. Vetter, C. Prahl, M. Niggemann, R. Kern, *Chem. Commun.*, 2005, 15, 2011.
- [13] (a) J. Ferber, J. Luther, *Sol. Energy Mater. Sol. Cells*, 1998, 54, 265; (b) S. Hore, C. Vetter, R. Kern, H. Smit, A. Hinsch, *Sol. Energy Mater. Sol. Cells*, 2006, 90, 1176; (b) M. Planells et al., *Energy Environ. Sci.*, 2011, 4, 1820; (c) A. Reynal, E. Palomares, *Eur. J. Inorg. Chem.*, 2011, 4509; (d) S. Guarnera, A. Bonucci, S. Perissinotto, R. Giannantonio, G. Lanzani, A. Petrozza, *RSC Adv.*, 2013, 3, 2163; (e) SAES GETTERS SPA, International Patent PCT/EP2010/067667, 17.11.2010.
- [14] (a) L. Chen, P. Wang, F. Li, S. Yu, Y. Chen, *Sol. Energy Mater. Sol. Cells*, 2012, 102, 66; (b) C.C. Oey et al., *Thin Solid Films*, 2005, 492, 253; (c) B. Riedel, J. Hauss, M. Aichholz, A. Gall, U. Lemmer, M. Gerken, *Org. Electron.*, 2010, 11, 1172; (d) Y.-J. Lin, Y.-C. Su, *J. Appl. Phys.*, 2012, 111, 073712.
- [15] (a) U. Costantino, F. Montanari, M. Nocchetti, F. Canepa, A. Frache, *J. Mater. Chem.*, 2007, 17, 1079; (b) F. R. Costa, M. Saphiannikova, U. Wagenknecht, G. Heinrich, *Adv. Polym. Sci.*, 2008, 210, 101; (c) G. G. Aloisi et al., *Mater. Chem. Phys.*, 2010, 123, 372; (d) U. Costantino et al., *ACS Appl. Mater. Interfaces*, 2009, 1, 668;

(e) D. G. Evans, X. Duan, *Chem. Commun.*, 2006, 5, 485; (f) L. Liu, J. C. Grunlan, *Adv. Funct. Mater.*, 2007, 17, 2343.

[16] (a) A. Vaccari, *Appl. Clay Sci.*, 1999, 14, 161; (b) M. Turco et al., *J. Catal.*, 2004, 228, 43; (c) T. Montanari et al., *Catal. Today*, 2010, 152, 104; (d) G. Busca, U. Costantino, T. Montanari, G. Ramis, C. Resini, M. Sisani, *Int. J. Hydrogen Energy*, 2010, 35, 5356.

[17] (a) L. Latterini, M. Nocchetti, U. Costantino, G. G. Aloisi, F. Elisei, *Inorg. Chim. Acta*, 2007, 360, 728; (b) L. Latterini, M. Nocchetti, G. G. Aloisi, U. Costantino, F. De Schryver, F. Elisei, *Langmuir*, 2007, 23, 12337; (c) W. Shi, M. Wei, J. Lu, D. G. Evans, X. J. Duan, *J. Phys. Chem. C*, 2009, 113, 12888; (d) T. Posati et al., *Cryst. Growth Des.*, 2010, 10, 2847; (e) T. Posati, F. Costantino, L. Latterini, M. Nocchetti, M. Paolantoni, L. Tarpani, *Inorg. Chem.*, 2012, 51, 13229.

[18] (a) X. Wang et al., *J. Mater. Chem. A*, DOI: 10.1039/c0xx00000x; (b) M. Bastianini et al., *Inorg. Chem.*, 2012, 51, 2560; (c) L. Teruel, Y. Bouizi, P. Atienzar, V. Fornes, H. Garcia, *Energy Environ. Sci.*, 2010, 3, 154; (d) J. H. Lee, J. Chang, J.-H. Cha, D.-Y. Jung, S. S. Kim, J. M. Kim, *Chem. Eur. J.*, 2010, 16, 8296.

[19] U. Costantino, F. Marmottini, M. Nocchetti, R. Vivani, *Eur. J. Inorg. Chem.*, 1998, 1439.

[20] (a) D. O'Hare, G. Hu, *J. Am. Chem. Soc.*, 2005, 127, 17808; (b) D. O'Hare, G. Hu, N. Wang, J. Davis, *J. Mater. Chem.*, 2007, 17, 2257; (c) F. Bellezza, A. Cipiciani, U. Costantino, M. Nocchetti, T. Posati, *Eur. J. Inorg. Chem.*, 2009, 2603; (d) F. Bellezza, M. Nocchetti, T. Posati, S. Giovagnoli, A. Cipiciani, *J. Colloid Interface Sci.*, 2012, 20, 376.

[21] L. Li, R. Ma, Y. Ebina, N. Iyi, T. Sasaki, *Chem. Mater.*, 2005, 17, 4386.

[22] R. Apetz, M. P. B. van Bruggen, *J. Am. Ceram. Soc.*, 2003, 86, 480.

[23] (a) C.-H. Tsai et al., *Org. Electron.*, 2011, 12, 2003; (b) J. Krč, M. Zeman, F. Smole, M. Topič, *J. Appl. Phys.*, 2002, 92, 749.

[24] D. Schroder, *Semiconductor material and device characterization*, 3rd edition (John Wiley & Sons Ltd, New Jersey, 2006).

[25] (a) L. Wang, C. Li, M. Liu, D. G. Evans, X. Duan, *Chem. Commun.*, 2007, 2, 123; (b) Z. Liu et al., *J. Am. Chem. Soc.*, 2006, 128, 4872.

[26] (a) G. Dennler et al., *Adv. Mater.*, 2008, 20, 579; (b) J. Yang et al., *ACS Nano*, 2011, 5, 6210; (c) S. Sista, Z. Hong, L.-M. Chen, Y. Yang, *Energy Environ. Sci.*, 2011, 4, 1606.

CHAPTER V: GENERAL CONCLUSIONS AND PROSPECTIVES

The development of efficient organic solar cells could be one approach to provide mankind with cheap, sustainable and ecofriendly energy. The introduction of the bulk heterojunction concept, of the different device architectures and of many light managing techniques led recently to devices with power conversion efficiencies exceeding 9%, showing the great potential of organic photovoltaics. Nevertheless, to compete with the inorganic solar cell technology, the power conversion efficiencies of organic photovoltaics have to rise further in the range between 10 and 15 %. Since the functioning of organic solar cells is based on a complex interplay of the physical, optical and electronic properties of its components, it is desirable to identify structural and energetic key characteristics of the materials that can lead to efficiency gains. Furthermore, there are virtually no limits for the synthesis of new organic photoactive materials. Therefore, it is crucial for the device fabrication process, as well as under a chemical point of view, to identify the most promising classes of materials, device architectures and other functional structures.

In the first part of this work, particular attention was given to the optimization of the BHJ OPV devices performances through an accurate tuning of the chemical structure of the polymeric donor materials. The main strategy applied was the use of structures with alternate electron withdrawing and electron donating units in the polymer backbone, to obtain highly conjugated co-polymers with a low band gap. A study on two different families of alternate donor-acceptor co-polymers was presented.

First, a series of not previously studied polymers based on the electron rich dithienosilole unit and cyano-substituted di- and tetra-thiophene electron withdrawing units have been designed, synthesized and characterized. The presence of the cyano substituents in the polymer backbone was proven to effectively lower its bandgap and HOMO and LUMO energies, enhancing its optical, photophysical and photovoltaic properties comparing to the unsubstituted polymer. In fact, for the cyano-substituted polymers, an enhanced charge-transfer from the polymer donor to the fullerene acceptor was demonstrated by polymer:fullerene time resolved luminescence quenching studies. Moreover, the presence of long alkyl side chains on tetra-thiophene moiety was proven to significantly increase the polymer solubility, electrical properties (light absorption and hole mobility), nano-structuring and opto-electrical properties of the relative blend films. As a result, the PCEs of the corresponding BHJ OPV devices was enhanced from 1% to around 5%.

The second family of studied donor-acceptor co-polymers was based on dialkoxy-benzodithiophene π electron-rich and benzothiadiazole π electron-poor alternated units. The comparison between a previously studied polymer, in which the same units are separated by a direct bond, and a new polymeric structure in which the moieties are separated by a vinyl-spacer, allowed the determination of the role of the spacer separating the co-polymer moieties on the overall BHJ OPV

performances. In particular, the use of the vinylene spacer allowed an increased π delocalization along the polymer backbone, with respect to the most common direct aryl-aryl connected co-polymer. The electrochemical investigation highlighted the ambipolar character of the new polymer, with both p- and n-doping processes being observable. The coupling of the two strong π electron-rich and π electron-poor moieties effectively led to the obtainment of a low band gap polymer, with HOMO and LUMO energies in agreement with the reference polymer with the same donor-acceptor moieties and a direct aryl-aryl linker. On the other hand, the presence of the vinylene spacer led to a lower optical bandgap and improved thermal stability, compared to the reference polymer with single bond spacer, probably due to the increased backbone planarization leading to stronger intermolecular interactions. The characterization of BHJ OPV devices containing the studied vinylene-spaced donor-acceptor polymer and PC_{xx}BM has given high photovoltages but low photocurrents, comparing to the reference directly bonded donor-acceptor polymer. The still non-optimal thin-film nano-morphologies and hole mobility properties, likely due to the relatively low molecular weight, could account for the obtained modest PCE, lower than 1%, which is nonetheless similar for the two compared polymers.

In a second part of the work, the focus was moved to the optimization of the performances of BHJ OPV devices by a deeper study of the role of buffer layers. Standard active layers made of P3HT:PCBM blends were employed in devices prepared with different semiconducting metal-oxides (TiO_x and ZnO) employed as cathode buffer materials and the same anode buffer layer (PEDOT:PSS). The optical, morphological and electrical properties of these materials have been investigated and their functioning as buffer layers in BHJ OPV devices with inverted structure was analyzed and compared with the reference P3HT:PC₆₁BM-based devices prepared in the standard architecture configuration (by employing LiF/Al cathode and ITO/PEDOT:PSS anode). The best efficiency was found for the standard architecture, while slightly lower efficiencies were found for the inverted one. The device with ZnO as cathode buffer layer presented a slightly lower J_{sc} , probably due to optical losses, while for TiO_x-based device a lower V_{oc} was measured. The analysis of the charge density distribution in the devices under working conditions under different light biases revealed a difference in the density of states distribution of the TiO_x-based device, compared to the ZnO-based and to the standard ones. Transient photovoltage measurements in open-circuit conditions at different light biases showed that charge recombination kinetics are comparable for the three different devices. The recombination kinetics were found to be dependent on the charge density through the same exponential function, characteristic of a bimolecular recombination process occurring within the organic layer. Therefore, the decreased V_{oc} of the TiO_x-based device, leading to its inferior performances, was explained by its different density of states distribution induced by the TiO_x metal oxide layer on the active layer blend through morphological and/or electrical changes, rather than to increased charge recombination kinetics within the active layer. The results and discussions provided open new insights for

further investigations on inverted devices. For instance, new metal oxides leading to narrower density of states distributions (inferior film roughness, decreased charge trapping states) could be employed in inverted OPV devices, paving the way toward higher V_{oc} and higher efficiencies.

In the last section, an overview on the light managing techniques that could improve solar cells light absorption was given. A deeper study on the technique of light trapping inside the device obtained by inserting a scattering material in the device architecture were applied to standard P3HT:PC₆₁BM-based devices. The scattering nanoparticles (Zn-Al layered double hydroxide, or hydrotalcite, nanoparticles) were easily dispersed in the PEDOT:PSS layer, avoiding in this way any alteration of the standard BHJ OPV device stack. The resulting PEDOT:PSS/nanoparticles composite film was proven to effectively scatter a portion of the transmitted light, thus leading to improved light absorption and J_{sc} of the related device, with PCEs going from 2.58%, for the reference device to ~ 3% for the device with the scattering composite film. The extraordinary versatility of the hydrotalcite nanoparticles employed, given by their relatively simple synthetic procedures and by the possibility to combine a wide variety of metals and counter-ions in their chemical structure, opens the way to the engineering of novel hydrotalcite-based composites for applications in the OPV technology. Indeed, device performances could be further improved by a rational and fine tuning of the optical, electrical and chemical properties of the employed nanoparticles.

In conclusion, this thesis gives an overview on the different possible strategies that could be adopted for the improvement of the performances of BHJ OPV devices. The accurate analysis of the chemical, energetic and physical criteria governing the solar cells behaviour allowed to individuate some critical aspects and apply possible solutions by a fine tuning of the material chemical structure, device processing techniques and device architecture engineering. Even though not in all cases, the applied strategy successfully led to device efficiency improvements as well as to the fundamental understanding of some efficiency limiting factors, which could serve as a useful scientific basis for future developments.

APPENDIX: LIST OF SYMBOLS AND ABBREVIATIONS

A	Electron acceptor
A%	Fractional Absorption
a-PANIN	poly(aniline) nanotubes doped with n-dodecylbenzenesulfonic acid and hydrochloric acid
ABL	Anode buffer layer
Abs	Absorbance
AFM	Atomic force microscopy
AM0	Air Mass 0
AM1.5	Air Mass 1.5
BDT	4,8-dialkoxy-benzo[1,2- <i>b</i> :4,5- <i>b'</i>]dithiophene
BHJ	Bulk hetero junction
BTD	2,1,3-benzothiadiazole
C	Capacitance
CBL	Cathode buffer layer
CE	Charge extraction technique
CN	Cyano group
CN-PPV	Cyano- Poly(<i>p</i> -phenylene vinylene)
CT	Charge transfer
CTAB	Cetyltrimethylammonium bromide
CV	Cyclic Voltammetry
<i>d</i>	Inter-lamellar spacing
D	Electron donor
D-A	Donor-acceptor
DFT/TDDFT	Density Functional Theory, Time Dependent Density Functional Theory
DIO	Di-iodooctane
DOS	Density of states
DPV	Differential pulse voltammetry
DSC	Differential scanning calorimetry
DSSCs	Dye sensitized solar cells
DT	Di-thiophene
<i>E</i>	Light bias (potential)
E_0	Potential at maximum capacitance
E_{A}	Electronic affinity of A
E_B	Exciton binding energy
EDOT	3,4-ethylenedioxihiophene
E_g	Band Gap
E_{gap}^o	Optical energy gap
E_{HOMO}, E_{LUMO}	Energy of HOMO, energy of LUMO levels
E_{ox}	Oxidation potential
EQE	External Quantum Efficiency
FF	Fill Factor

GPC	Gel Permeation Chromatography
h,k	Θ reflections in XRD measure
HOMO	Highest Occupied Molecular Orbital
H _t	Haze parameter for transmitted light
HTs	Hydrotalcite nanoparticles
i-OPV	Inverted configuration organic photovoltaic device
I-V	Current-voltage
I _{dark} (V)	Dark current
I _m	Maximum current (current at MPP)
IP _A	Ionization potential of A
IQE	Internal Quantum Efficiency
I _{sc}	Short circuit photocurrent
ITO	Indium Tin Oxide
J	Current density
J _{dark} (V)	Dark current density
J _{sc}	Short circuit photocurrent density
k _B	Boltzmann constant
k _R	Charge recombination rate
LT	Laser in-line transmission
LUMO	Lowest Unoccupied Molecular Orbital
MDMO-PPV	Poly[2-methoxy-5-(3',7'-dimethyloctyloxy)-1,4-phenylenevinylene]
M _w	Weight average polymer molecular weight
M _n	Number average polymer molecular weight
MPP	Maximum Power Point
n	Device density of charges
N	Maximum limit of charge density per volume unit
N _e	Number of extracted electrons
NMR	Nuclear Magnetic Resonance
N _{ph}	Number of incident photons
OFET	Organic Field Effect Transistor
OLED	Organic light emitting diode
OPV	Organic Photovoltaic
P3HT	Poly(3-hexylthiophene)
P3OT	Poly(3-octylthiophene)
PC ₆₁ BM	Phenyl-C61-butyric acid methyl ester
PC ₇₁ BM	Phenyl-C71-butyric acid methyl ester
PCE	Power Conversion Efficiency
PCM	polarizable continuum model
Pd ₂ (dba) ₃	Tris(dibenzylideneacetone)dipalladium(0)
PDI	Poly-dispersity Index
PEDOT:PSS	poly(3,4-ethylenedioxythiophene): poly(styrene sulfonic acid)
PFT	poly[(9,9-dioctylfluorene)- co-N-(4-(1-methylpropyl)phenyl) diphenylamine]

PHEDOT	Poly[3,4-(1-hydroxymethyl)ethylenedioxythiophene]
P_L	Power density input of sunlight
PL	Photoluminescence
P_m	Power density output of a solar cell
P_{max}	Maximum power
PPV	Poly(<i>p</i> -phenylene vinylene)
PSS	Poly(4-styrenesulfonate)
PV	Photovoltaic
q	Electron elementary charge
Q	Photoluminescence quenching ratio
Q	Total device charge
R_L	Load resistance
RMS	Root mean square roughness
R_s	Series Resistance
R_{sh}	Sheet resistance
R_p	Parallel Resistance
SCLC	Space Charge Limited Current
SEM	Scanning Electron Microscopy
SiDT	Di-thieno-silole
T%	Total transmittance
t_1, t_2	Components of PL decay lifetime
TBAClO ₄	Tetrabutylammonium perchlorate
T_d	Decomposition temperature
T_{dif}	Diffused transmittance
TGA	Thermal gravimetric analysis
T_{lin}	Linear transmitted light
Tol ₃ P	Tri(<i>o</i> -tolyl)phosphine
TPV	Transient photo-voltage technique
TRPL	Time resolved photoluminescence
TT	Tetra-thiophene
T_{tot}	Total transmitted light
V	Voltage
V_m	Maximum voltage (voltage at MPP)
V_{oc}	Open circuit voltage
Vol	Volume available for charge accumulation
w_1, w_2	Pre-exponential factors (weights) in PL decay fitting expression
WF	Workfunction
XRD	X-ray diffraction
ZnAl-HTs	Zn(II)-Al(III) based HTs
ZnAl-HT _{wg}	Zn(II)-Al(III) based HTs prepared with urea method in water and ethylene glycol
ZnAl-HT _{μE}	Zn(II)-Al(III) based HTs prepared with microemulsion process

σ	DOS Curvature
ΔH_t	Differential haze for transmitted light
ε	Absorption molar coefficient
ε_0	Vacuum permittivity
ε_{\max}	Maximum of absorption molar coefficient
ε_r	Relative permittivity
ϕ	Pinhole inner diameter
ξ	Ideality Factor
λ_{\max}	Wavelength of the absorption spectrum maximum
λ_0	Wavelength of the absorption spectrum onset
η	Efficiency of a solar cell under 1 sun illumination
μ	Charge mobility
μ_h	Hole mobility